Synthesis and Characterization of Cobalt-Based Coordination Complexes with Various Organic Linkers

by

Md Faruque Hasan

Submitted in Partial Fulfillment of the Requirements

for the Degree of

Master of Science

in the

Chemistry

Program

YOUNGSTOWN STATE UNIVERSITY

August, 2018

Synthesis and Characterization of Cobalt-Based Coordination Complexes with Various Organic Linkers.

Md Faruque Hasan

I hereby release this thesis to the public. I understand that this will be made available from the OhioLINK ETD Center and the Maag Library Circulation Desk for public access. I also authorize the University or other individuals to make copies of this thesis as needed for scholarly research.

Signature:

_____

Md Faruque Hasan, Student Date

Approvals:

_____

Dr. Sherri Lovelace-Cameron, Thesis Advisor Date

_____

Dr. Timothy R. Wagner, Committee Member Date

_____

Dr. Clovis A. Linkous, Committee Member Date

_____

Dr. Salvatore A. Sanders, Dean of Graduate Studies Date

ABSTRACT

Metal-organic frameworks (MOFs) are being explored and investigated for a wide range of potential industrial applications due to the massive diversity of its structures and so many properties. Metal-organic framework compounds offer extremely large surface area, higher empty space volume, flexible networks, perfect mechanical and thermal stability, MOF can provide size or shape selectivity, and all of these are necessary for many industrial applications. In this research, different types of cobalt MOFs and coordination complexes have been synthesized with solvothermal process by fabricating cobalt (II) ion (normally metal salt) coordinated with organic ligand (normally organic carboxylate acid or basic organic compound or sometimes both and Nitrogen based third party linkers) and required solvent with subsequent heating condition. Various characterization techniques have been employed such as: single crystal X-ray diffraction (SXRD), powder X-ray diffraction (PXRD), scanning electron microscopy (SEM), energy dispersive X-ray spectroscopy (EDS), transmission electron microscopy (TEM), thermogravimetric analysis **(**TGA), nuclear magnetic resonance (NMR), and BET surface area.

Acknowledgment

I would like to express my thanks to the Chemistry Department of Youngstown State University for giving me the scope to pursue the master's degree. I would like to thank my research and academic advisor, Dr. Sherri Lovelace-Cameron, for the knowledge and support she provides me, her devotion, motivation, encouragement, and guidance.

I would like to express my gratitude to my thesis committee advisers, Dr. Timothy R. Wagner and Dr. Clovis A. Linkous for their kind support and insights on the research. I would like to thank Dr. Matthias Zeller for analyzing single crystal X-ray Diffraction (SXRD) data and providing suitable suggestions based on the SXRD observation.

I would like to thank all the faculty members of the Chemistry Department of YSU for providing me tremendous help in both academia and research. I would like to express profound gratitude to Ray Hoff for help with all of instrumentation training and SXRD data collection. I also would like to thank Lisa DeVore for the administrative assistance and Timothy Styranec for the safety awareness and chemical supply on the research.

I would like to thank the YSU Center for Advanced Materials Analysis for giving the opportunity to perform advanced characterization such as SEM, EDS and TEM analysis. I would like to thank Dr. Virgil Solomon for helping me to learn SEM, EDS analysis. I would like to thank Dr. Shaikh Tofazzel Hossain for collecting the TEM data in this project.

I would like to thank the Chemistry Department of the University of Akron, for the solid-state NMR analysis.

I would like to thank my colleagues and friends at the Chemistry Department of YSU. I would like to express my special gratitude to Abm Mostafizur Rahman, Shanzida Alam, Samara, Sohel, Erfan Uddin and Jisan Minhaz, who made me feel like I was at home during my MS study.

I would like to express my deepest thanks to my family and in-laws family, for their love, sacrifice and tremendous support, encouragement, and understanding.

I would like to dedicate this thesis to my loving and supporting wife, Khadiza Parvin, and to my mother, Maziran Nesa. Their love and sacrifice have helped me to fulfill my dreams.

Table of Contents.

List of Figures

List of Tables

List of Abbreviations

Abbreviation	Full form
Å	Ångstrom
θ	Theta, Angle of Incidence
a, b, c	Cell parameters
BDC	Benzenedicarboxylate
BTC	Benzenetricarboxylate
BTCA or H_3BTCA	1,3,5- Benzenetricarboxylic acid
Bpy	Bipyridine
BET	Brunauer Emmett-Teller
cm	Centimeters
cm^{-1}	Reciprocal centimeters, wavenumbers
cm^3	Centimeters cubed, volume
CHDA or H_2CHDA	1,4- Cyclohexanedicarboxylic acid
cps	Counts per second
^0C	Degrees Celsius
di-	Two
d	Distance
DMF	N, N'-dimethylformamide
eV	Electron Volts
E	Energy
EDS	Energy dispersive X-ray spectroscopy

EtOH	Ethanol
g	Grams or gas
hkl	Miller indices
I	Intensity
K	Kelvin
k	Kilo
kV	Kilovolt
μ m	Micrometer
m	Meter
mm	Millimeter
M	Metal atom (Co)
MeOH	Methanol
MOF	Metal-Organic Framework
mol	Mole
mmol	Millimole
NMR	Nuclear magnetic resonance
nm	Nanometer
O-	Oxide
PCP	Porous coordination polymer
ppm	Parts per million
psi	Pounds per square inch
SBU	Secondary building unit

SEI	Secondary electron images
SEM	Scanning electron microscopy
SDBA	4-4'sulfonyl dibenzoic acid
SXRD	Single Crystal X-ray diffraction
T	Temperature
TEM	Transmission Electron Microscopy
HRTEM	High-Resolution Transmission Electron Microscopy
TGA	Thermal Gravimetric Analysis
TMdiPy or 4,4'- TMdiPy	4,4'- Trimethylenedipyridine
PXRD	Powder X-ray diffraction
% wt	Percent weight
x	Thickness
XRD	X-ray diffraction
λ	Wavelength
ZIF	Zeolitic Imidazolate Framework

Chapter 1: Introduction

MOF materials have attracted immense attention for their usage in gas storage, fuel cell, gas purification, luminescence, sensing, electronic device, heterogeneous catalysis, ion exchange, drug delivery, semiconductor, superconductor, composite materials, electrochemistry, thin film, separation applications and so many applications are now being investigated.[1] The goal of the research is to find out the production scope of new cobalt-based metal-organic frameworks as well as cobalt coordinated complexes with required synthesis and characterization techniques for different application. Different ways for characterization will also be analyzed. Our research project aims to identify appropriate synthesis directions for cobalt-based MOFs and coordination complexes which are well fitted for industrial production.

1.1 Background

MOFs are organic-inorganic integrated materials, and these materials can be constructed by bonding between a variety of inorganic metal ions and a numerous number of organic linkers. These integrated materials can be used for many volume specific applications and other important applications. [2] MOF materials can permit various types of chemical changes, such as organic molecule or compound conversion, possess very large pore area with comparatively higher surface areas, have the capability of capturing of small molecules, the introduction of foreign molecules and these materials have higher bulk capacity. These features and characteristics are best suited for the different types of storage and sorption type application of MOFs. Moreover, if third-party linker or compound is added during the synthesis procedure, the MOF's characteristics and

applicability will be amended.[3] Metal-organic framework compounds have many auspicious characteristics which include: excellent surface area with extreme void space, adaptable networks, optimum mechanical and thermal durability, the eminent flexibility of different foreign molecules and enormous variety of chemical arrangements and structures. These properties can make MOFs amenable for plenty of various practical industrial applications. Because of improved processing technology and auspicious characteristics, different types of MOF applications in the industrial sector are very economical and highly efficient.[4]

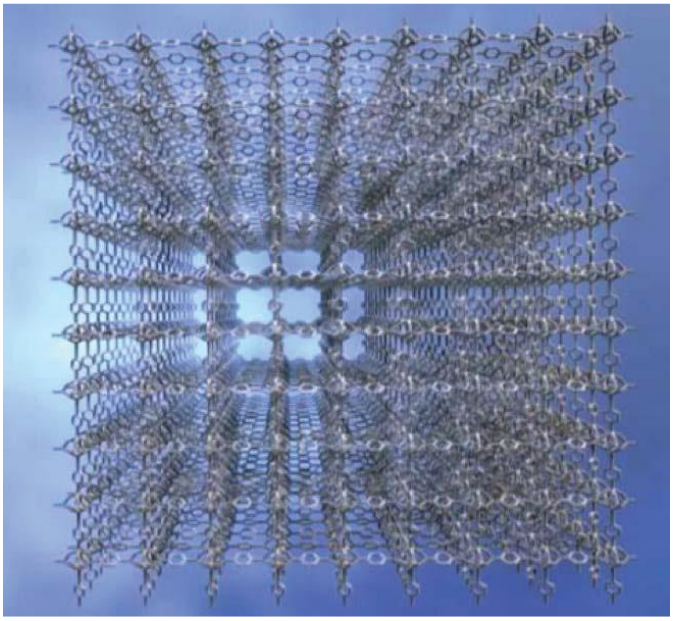

Fig. 1: The MOF-5 structure is showing free entree to nano-pores and the nonappearance of unapproachable bulk-volume. (Reproduced with permission) [4]

The three-dimensional MOF configuration can be shaped by the amendment of various types of ligand or linker and bridging or connection between these ligand and metal ions. Because of their three dimensional structure with the higher spacing area, MOF materials become the most promising materials for catalytic and adsorption application.[5]

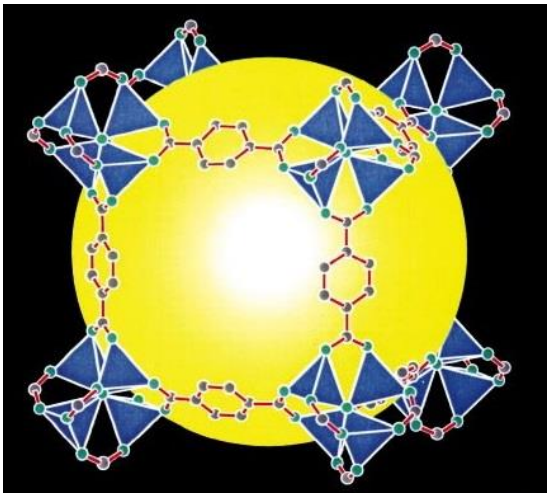

Fig. 2: Structure of MOF-5. (Reproduced with permission) [6]

There are immense possibilities of finding diverse organizational metal-organic framework because of the various construction mechanisms of metal ions and linkers or ligands. MOFs can be extensively used for the extraction of sulfur from different gases to purify the compound or gases. O ther volume related applications of MOFs, such as gas uptake, separation or adsorption application, catalytic behavior of MOF, etc. are now being revealed and analyzed continuously.[7]

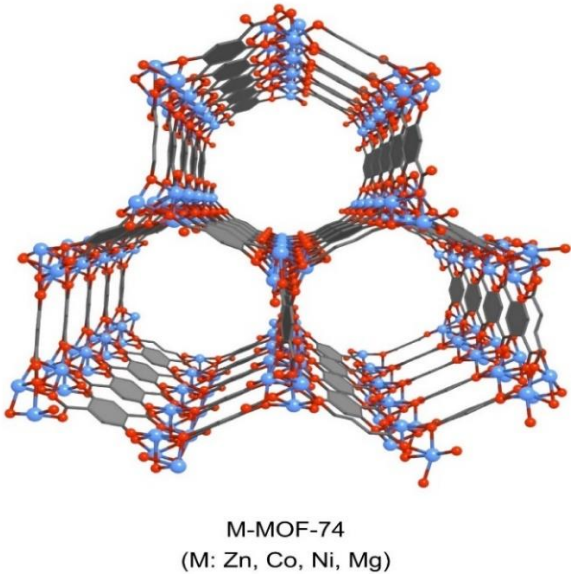

Fig. 3: Typical MOF-74 structure (Reproduced with permission) [8]

Nowadays, addressing CO_2 adsorption has become vastly attractive because of the worldwide environmental concern. MOFs are unique adsorbents for CO_2 separation having volume specific properties such as very large space volumes, manageable compositions, and structures. More importantly, CO_2 storage with MOFs is an efficient and the cheap and convenient instrumental technology. [9]

Yaghi and his research associates showed the hydrogen adsorption properties of different metal-organic frameworks and improved techniques for hydrogen storage capacity of those MOFs; such as MOF-5, IRMOF-6, and IRMOF-8. After all the property investigations and characterization tests and analysis it was stated that MOFs are considered as an efficient and competent hydrogen storing materials. For enhancing the capture capacity of hydrogen with MOFs, some modification techniques were made, and those techniques for enhancing hydrogen storage capacity are the management of pore size, ligand alteration, impregnation with foreign molecules, interpenetration and the introduction of different free metal spaces.[10] After the modification of functional pore size, many MOF compounds become more popular for hydrogen storage, separation or other volume and energy-related industrial applications.[11]

Nowadays due to needing an alternative fuel source, much interest is focused on electric power applications; such as fuel cell application with the storage or adsorption principle of hydrogen in metal-organic frameworks. Also, the associated cost of production of MOFs are very low, and so the feasibility of hydrogen storage is the most exciting and electrifying. [12]

M. Masoomi and his research associates produced two different type of cobalt-based MOFs named TMU-10 (**$[Co_6(oba)_5(OH)_2(H_2O)_2(DMF)_4]_n \cdot 5DMF$**) and TMU-12 (**$[Co_3(oba)_3(O)(Py)_{0.5}]_n \cdot 4DMF \cdot Py$**) with the solvothermal process (oba = 4,4′-oxybisbenzoicacid). These MOFs showed different functional morphologies and characteristics. More catalytic capability was found for TMU-12 than TMU-10 because of the variation in coordinate centers and empty pores. Both of the produced MOFs were used for catalytic application in the oxidative desulfurization (ODS) reaction.[13]

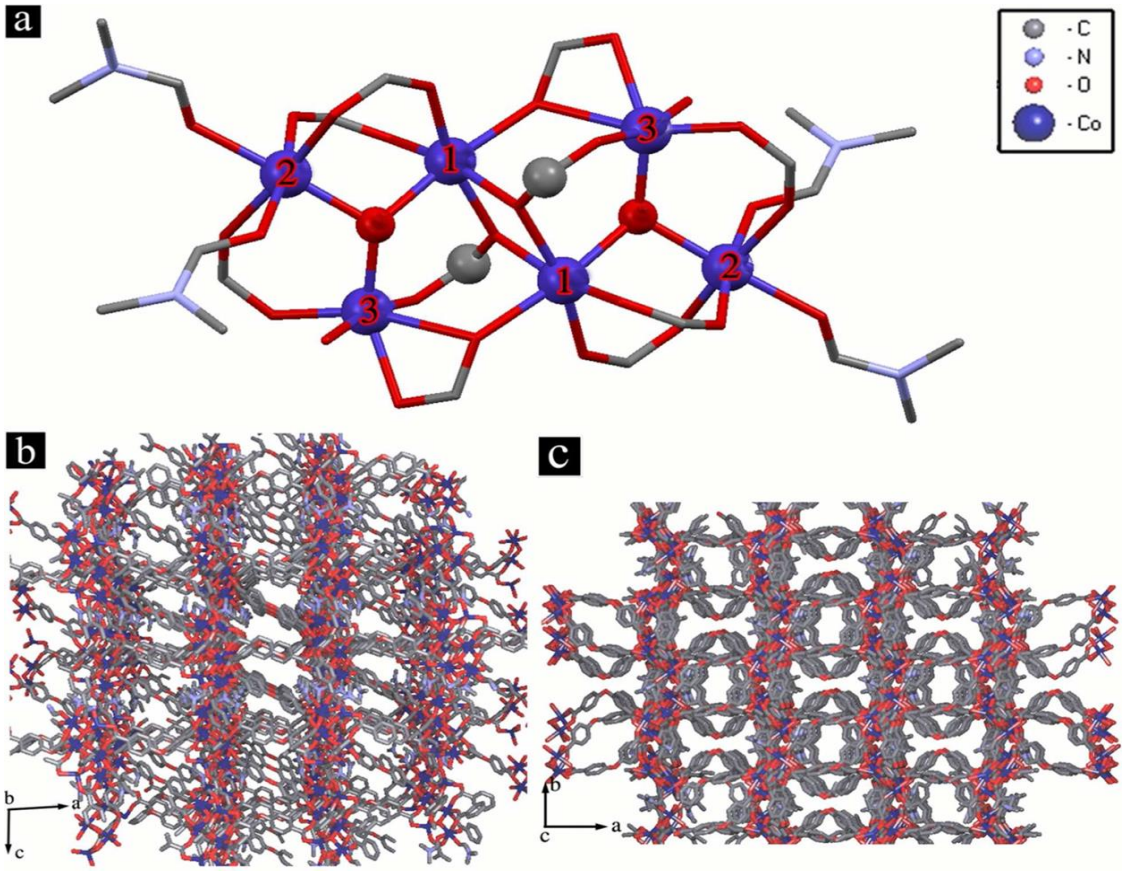

Fig. 4: a) Ball and stick model of the secondary building units (SBUs), $Co_6(CO_2)_{10}(O)_2(O)_4$ in TMU-10. (b and c). model of voids. (Reproduced or reprinted with permission) [13]

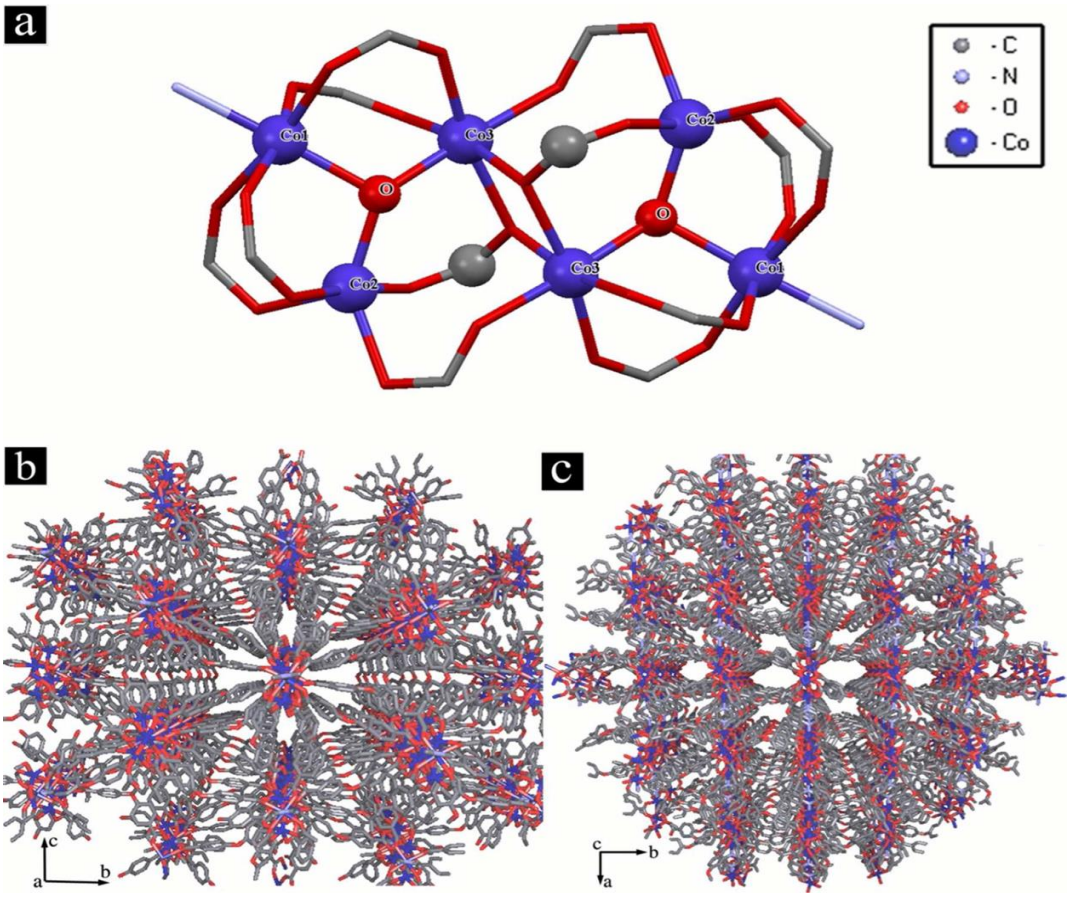

Fig. 5: a) Model of the secondary building units, $Co_6(CO_2)_{12}(O)_2(N)_2$ in TMU-12. (b and c) model of voids in b and c direction. (Reproduced or reprinted with permission) [13]

Bo. You and his research associates investigated and demonstrated N-doped electrocatalysts named as CoP_x (a combination of CoP and Co_2P) for water splitting application involving hydrogen evolution reaction (HER) and oxygen evolution reaction (OER) experiment. With the carbonization method of cobalt-based zeolitic imidazolate framework, the Co-P/NC catalysts were synthesized and then characterized. The produced catalyst showed manageable pore structure, high nitrogen percentage (weight%) and very high surface area. From the HER and OER experiment, Co-P/NC showed excellent catalytic activity with optimum stability at an experimental current

density of 10 mA cm^{-2}. High crystallinity and zeolite-like configuration were found in the X-ray diffraction(XRD) patterns, and X-ray absorption spectroscopy characterized its excellent catalytic capability with optimum durability.[14]

According to the theory produced by Xiuxiu Liu and his research group members, their synthesized cobalt-based layered MOF (Co −LMOF) is an excellent electrode compound for supercapacitor applications. The Co−LMOF electrode showed optimum specific capacitance and cycling durability with the analysis of a cyclic voltammetry (CV) test. Nanoparticles of Co-LMOF maximize the surface area, minimize ion diffusion path and expand active sites. This experimental study established cobalt layered based metal-organic frameworks as unique electrode materials for supercapacitor applications.[15]

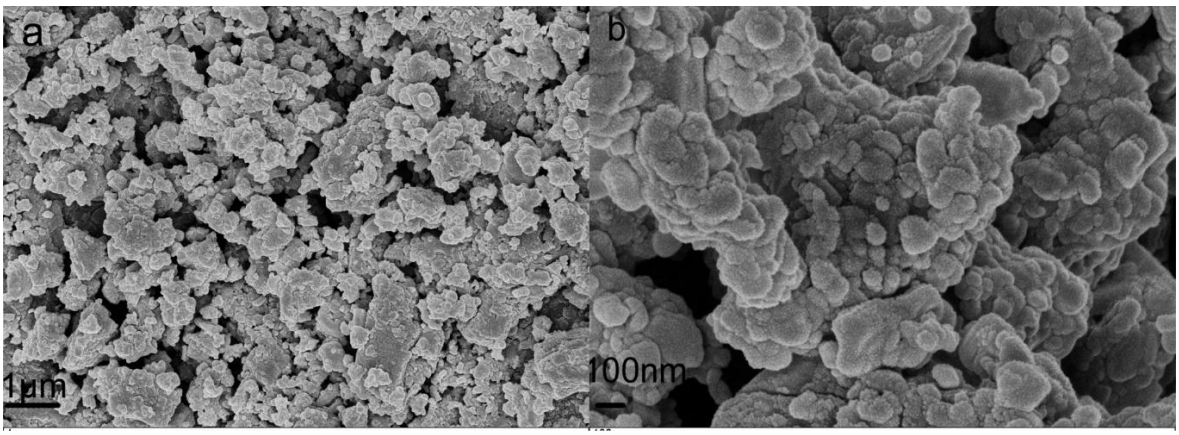

Fig. 6: (a) Low-magnification and (b) high-magnification Field Emission SEM images of Cobalt-based layered MOF (Reprinted or reproduced with permission) [15]

For the analysis and explanation of electrochemistry and catalytic applications, Watcharop Chaikittisilp's team manufactured new carbon-cobalt-oxide integrated compounds by thermal transformation of Metal-Organic Frameworks. In the oxygen

reduction and evolution reactions, these integrated compounds showed exceptional catalytic features and can be used as a catalyst in fuel cells. [16]

In Wei-Jin Li research group's work, with the practice of the solvothermal process, unique metal-organic framework (MOF) based films were produced and were analyzed with different characterization techniques. With the increment of both temperature for pre-activation and reagent amounts, the produced films become more compact and consistent. Optical instruments, dye materials capture, or organic vapor sensing may be a possible prospect for this manufactured MOF films. [17]

Practically, MOFs are now being fabricated by traditional hydrothermal or solvothermal methods. Nowadays, many modern improved manufacturing procedures are being inspected such as electrochemical manufacturing procedure, microwave-cooperated method, spray-drying process, mechanochemical fabrication process, etc. The microwave-cooperated process and the electrochemical process are becoming very promising from the economic and industrial perspective. The interconnection between electromagnetic waves and moving electric charges is the principle of microwave-cooperated method, whereas in the electrochemical method, continuous anodic dissolution of metal ions is the principle of the manufacturing procedure. Over the conventional synthesis procedure, both microwave cooperated and electrochemical processes have certain benefits, such as they are continuous processes, large-scale MOF materials production is possible, energy consumption is lower and most importantly, they are cost effective. [18]

1.2 Importance of Cobalt-based Coordination Complex

The benefits of MOFs are flourished by the properties that initiate from their porosity and constructions. Because of the various types of manufacturing techniques, the extent and features of MOF nanomaterials become vastly controllable. The characteristics and applicability of MOF materials have developed significantly in the last few years. [1]

Cobalt metal is a transitional d-block element and is commonly found having an oxidation state of +2 and +3. Because of its transitional characteristics, cobalt has better coordination capability in a variety of cobalt complexes. Another aspect of the study of cobalt complexes is that there are not so many studies on cobalt MOFs or coordinated cobalt complexes that have been published in the research area.

1.3 Problem Statement

Synthesis and characterization of novel cobalt coordination complexes with investigation of the various type of organic linkers is the objective of this research project. For the synthesis procedure, conventional solvothermal synthesis techniques will be used and various instrumentation techniques will be practiced, analyzing the physical and chemical properties of the produced cobalt complexes or frameworks.

Chapter 2: Experimental

2.1 Experimental Methods

The synthesis of MOFs or coordinated complexes usually involves mixing metal nitrates $Co(NO_3)_2$ and organic acids or bases with polar organic solvent, particularly an amine or amide along with solvents like ethanol. After a combination of these inorganic and organic components with required stirring, the mixture is transferred into a Teflon-lined autoclave; the metal-organic structures are formed under heated conditions.

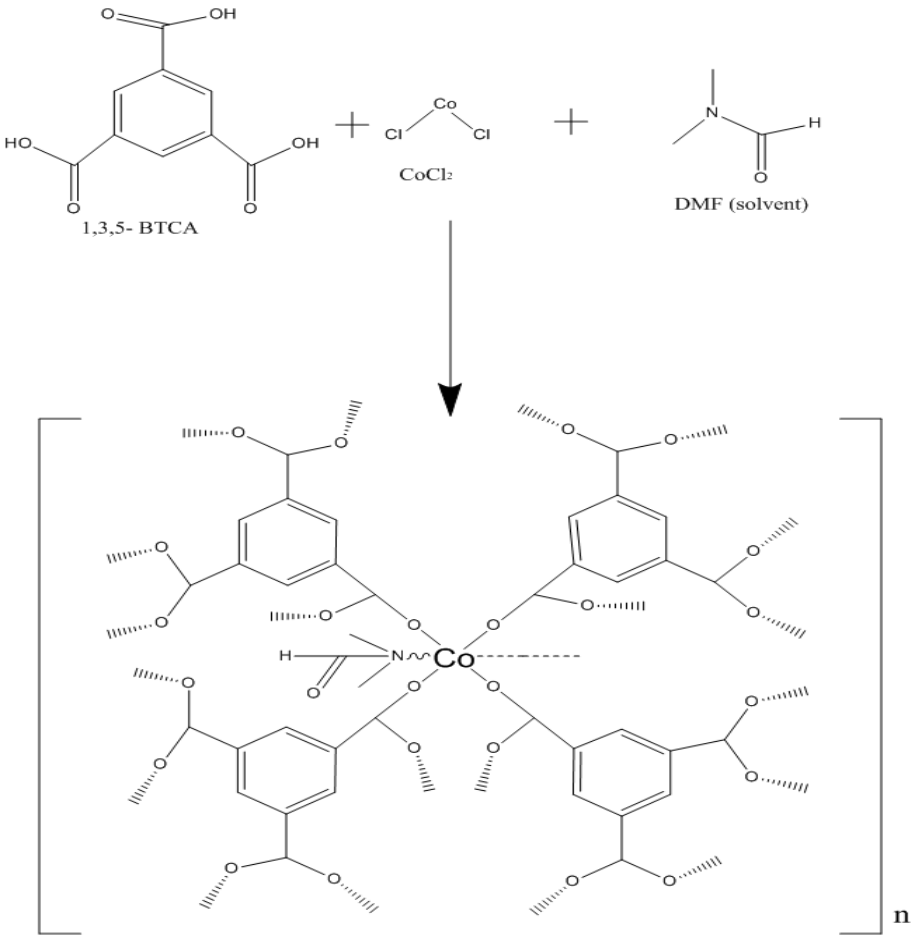

Fig. 7: Typical Co-MOF reaction

A typical reaction for a Co-MOF may be represented by the schematic in figure 7. Our approach toward new Co-MOFs or complexes synthesis is the solvothermal process.

2.2 Experimental Materials

As a metal salt, we first used cobalt (II) nitrate hexahydrate [$Co(NO_3)_2$. $6H_2O$] and later anhydrous cobalt (II) nitrate [$Co(NO_3)_2$] and lastly, we used anhydrous cobalt chloride ($CoCl_2$). We tried to investigate different properties by synthesizing materials with different types of linker such as: 1,4-cyclohexanedicarboxylic acid (1,4-CHDA), 1,3,5-benzenetricarboxylic acid (1,3,5- BTCA), 2-aminoterephthalic acid (2-ATTA), adenine, 5-nitrobenzimidazole, imidazole, 4,4'- trimethylenedipyridine, 4,4- sulfonyldibenzoic acid, 4,4--bipyridine and piperazine. As a solvent, we used either 100% dimethylformamide (DMF), or a mixture of DMF and another solvent like ethanol, methanol, or water. For changing pH, we sometimes used sodium hydroxide (NaOH) or hydrochloric acid (HCl). All materials were bought from either Sigma-Aldrich or Fisher Scientific or other reputable chemical seller.

2.3 Preparation of Autoclave

Teflon autoclave vessels were cleaned with distilled water and soap first, and then with using 5% (V/V) HNO_3, a stir plate, and stir bar, vessels were stirred for 10-30 minutes. After stirring the Teflon liners were sealed in the in-steel autoclave vessel and put into the oven for 10-12 hours at a temperature of 150 ^{0}C. All vessels were taken out from the oven emptied and rinsed with distilled water, and finally dried in an oven for a minimum of 24 hours.

2.4 Reaction Principle

Most reaction procedures followed the following sequence: the metal salt cobalt(II)nitrate or cobalt(II)chloride, followed by the organic linker was added into the Teflon autoclave liner with a stir bar. The required solvent was pipetted into the vessel with accurate measurement. Nitrogen-based linkers were added as a third-party linker to strengthen the cobalt linking ability in some experiments. The solution was stirred using a stir plate for 10-20 minutes until the solids were dissolved. After mixing, the Teflon autoclaves were closed with steel vessels and sealed carefully. The sealed steel specimens were placed in a pre-heated oven. After subsequent reaction heating, samples were cooled down to room temperature and visually inspected to see if crystals formed. If crystals were present, samples were transferred to glass vials or rinsed with a non-deuterated solvent such as chloroform. If the sample was in powder form, solutions were filtered with a vacuum pump and dried in a 60-70 ^{0}C oven for12-14 hours. Before the reaction and after the reaction the pH of the solution was determined. After drying, samples were placed into glass vials for further characterization or activation processes.

2.5 Activation of Samples

In the production procedure of MOFs, solvent or unreacted linker may be captured in the void of the MOF structure. This excess solvent must be eliminated from the MOF structure to get the optimum porosity and large surface areas. There are many activation techniques, such as the conventional activation methods of just heating and vacuum drying, solvent exchange activation, supercritical freeze drying and chemical treatment activation process.[19] In our experiment, we used a conventional activation procedure

where we heated our sample in the furnace in the temperature range of 160-200 ^{0}C under vacuum sometimes or without vacuum treatment. After the activation process, we witnessed the significant change of the material's appearance and properties, such as densification. We applied the activation method to only some samples to analyze the activation effect on MOF structure.

Chapter 3: Characterization Methodology and Instrumentation

3.1 Visual Inspection and Aqueous Solution Test:

At first, samples were visually inspected and analyzed for further solid state or liquid state analysis. After reaction and before drying the pH was tested with the scale corresponds to aqueous solutions and noted in the notebook to analyze the effect of pH in the solution.

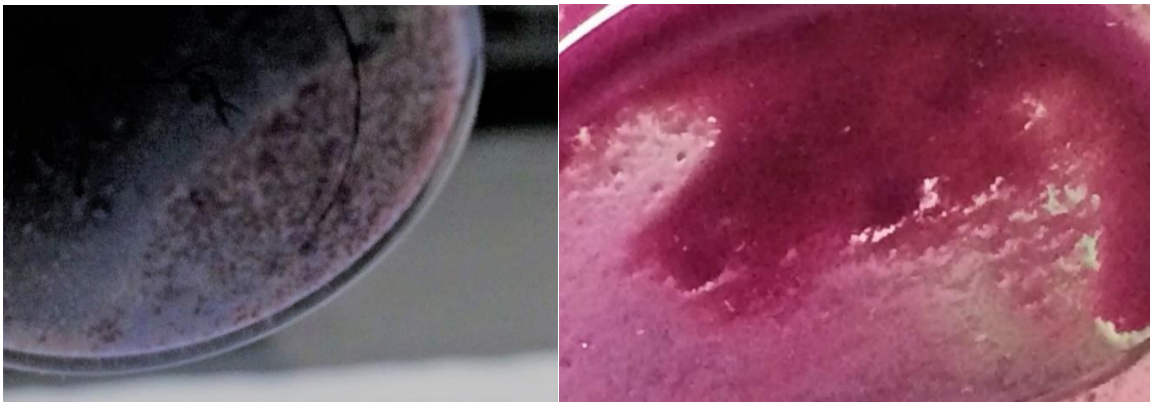

Fig. 8: Visual inspection of samples.

3.2 Optical Microscopy

Our samples were taken into the Zeiss stereo microscope to inspect the magnified morphology of the powder and crystal samples. An Axiocam MRC camera was added to the instrument to take live image and transferred them into the computer.

3.3 Powder X-Ray Diffraction

X-ray powder diffraction (XRD) is an analytical technique that is principally used for determining the phase credentials of a crystalline material and can provide information on unit cell structure. Analyzing principle follow the Bragg's law ($n\lambda = 2d \sin\theta$). The diffracted X-rays are identified by detectors in a range of 2θ angles, and diffracted peaks are normally transformed into d-spacings to classify the phases. In our experiment,

Powder X-ray Diffraction (PXRD) patterns were measured on a Rigaku Miniflex powder X-ray diffraction instrument or X8 Prospector instrument with a Cu-Kα radiation mechanism. In our experiment, we used both instruments. For the Rigaku Miniflex diffractometer, samples were ground and pressed into the circular aluminum disc and placed into the instrument. The sample run time was three hours. The data was converted into a PowDLL converter and analyzed in DIFFRAC.EVA software of SOCABIM circulated by Bruker AXS.[20] For X8 Prospector, the powder was taken on the tip of the specimen holder and inserted in the instrument for 20-45 min depending on image collection time selection criteria. After getting data, raw files were created and analyzed similarly with DIFFRAC.EVA software with the help of the Cambridge database system.

3.4 Single Crystal X-Ray Diffraction

Selected samples were examined for single crystal x-ray diffraction on the D8 Quest instrument or X8 Prospector instrument with a Bruker AXS Smart APEX CCD diffractometer. The calculations of squares reflection principles measured the lattice parameters. For data collection, Apex2 V.2012.4-3, For integration of data SAINT V8.18C were used. For solving the material's structure, SHELX software was used and for refinement of structure SHELXTL software was used.[20] Data and images were analyzed in the crystal maker software. Publication-quality images and crystal information were collected from the IUCr Journals website with our CIF files. [21]

3.5 Thermogravimetric Analysis (TGA)

Thermogravimetric analysis or thermal gravimetric analysis (TGA) is a method of thermal analysis in which the mass or weight change of a sample is measured over time as the temperature changes (normally increases). From TGA analysis, we can measure weight or mass change (either loss or gain) and the rate of weight change as a function of temperature and time. TGA data were taken from a Hi-Ros TGA 2050 Thermogravimetric Analyzer. Platinum pans were used after cleaning with nitric acid. On the platinum pan, an aluminum pan was added to enhance the reusability of the platinum pan. Samples were heated at a rate of 10 ^{0}C min^{-1} from 50 ^{0}C to 600 ^{0}C with a flow of 10-90 mL min^{-1} nitrogen.

3.6 BET Surface Area

Brunauer-Emmett-Teller (BET) concept is a widespread method by which we can measure the surface area of powder and porous materials like metal-organic frameworks. In our research work, we used a Micromeritics Auto-Chem^{TM} II 2920 to calculate the surface area of our powder sample. The sample was inserted in a U-shaped glass tube, and nitrogen gas was purged through the glass tube and at the time the temperature of the sample was reduced to ~77 K. The temperature of the sample was then increased to room temperature by using water (in a beaker). With detection by Thermal Conductivity Detector (TCD), the quantity of entombed nitrogen gas molecules was measured and after getting all the information, computer software could measure the surface area and monolayer volume of sample.

3.7 Raman Spectroscopy

Raman spectroscopy is conventionally practiced for detecting vibrational, rotational, and other low-frequency modes of materials by which we can perform sample identification and quantitation. The Raman method uses a monochromatic light source on a specimen and detects frequency shifts in the scattered light. Raman method is proficient in investigating solid powder samples and liquid samples swiftly. In this method frequency shift of a small segment of the scattered radiation is isolated from the incident radiation. The basic principle of this technique is the inelastic scattering of incident radiation. [22] If the scattered light frequency is the same as the excitation source that is termed as Rayleigh or elastic scattering. A small portion of the scattered light is shifted or altered in energy from the laser frequency because of the connections between the incident waves and the vibrational or rotational energy levels of the molecules in the specimen. Changes in light intensity due to absorption versus Raman shift (frequency) is plotted in a Raman spectrum of the specimen. Raman spectroscopy method is normally used for both qualitative and quantitative purpose. [23]

We used the Horiba iHR320 to obtain the Raman spectrum of various samples. This spectrometer exploits a laser (green laser beam of 532 nm wavelength) to excite the molecular vibrations. For calibration purposes, silicon single crystal wafer was used.

3.8 Scanning Electron Microscopy (SEM) Analysis

For structural morphology inspection, SEM analysis was done. We used high-performance SEM and micro milling FIB (Focused Ion Beam) which utilizes the most popular LaB_6 electron beam. The JEOL JIB-4500 Multibeam dispenses instantaneous

imaging, analysis, compositional analysis and micro milling functions.[24] Typical JEOL JIB-4500 -SEM-FIB features as: LaB6 emitter; acceleration voltage is 0.3V to 30,000 V or 30 KeV; Scanning Electron Microscope (SEM) resolution: ~2.5 nm at 30 keV; Omni-probe: OMP-AUTOPROBE 200.1 [25]

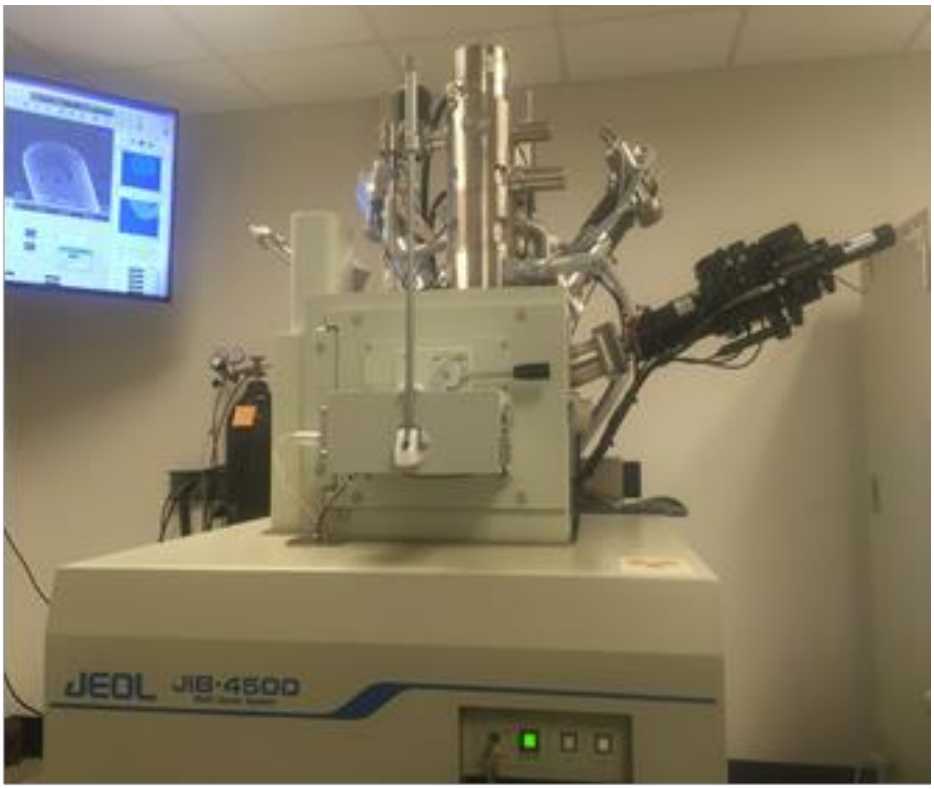

Fig. 9: SEM (JEOL JIB-4500) facilities at YSU

Our samples were examined on the JEOL JIB-4500 instrument. Powder samples were attached on specimen holder with the help of carbon tape. After entering the sample, the acceleration voltage was increased gradually up to 15 KeV, and then the filament was preheated. The filament current was also increased gradually. After that, with changing magnification, contrast, and brightness, appropriate microstructures were found from the specimens.

3.9 Energy Dispersive X-ray Spectroscopy (EDS) Analysis

EDS analysis was determined using a JEOL JIB-4500 instrument. For the EDS analysis, a stationary X-ray detector obtained emission from a SEM sample. After the scanning and imaging, appropriate scan areas were selected, and the X-ray emission spectrum (counts vs. E) was generated. With the help of ZAF (Z-the atomic number factor, A- the X-ray absorption factor, F- the fluorescent factor) correction method, the elemental composition was found and analyzed.

3.10 Transmission Electron Microscopy (TEM) Analysis

For TEM analysis we used a JEOL JEM2100 Scanning/Transmission Electron Microscope, which is a multipurpose 200 kV analytical electron microscope. [26]

Fig. 10: TEM (JEOL JEM-2100) facilities at YSU

Features of the JEOL JEM 2100 TEM are: accelerating voltage: up to 200,000 Volts (200 KeV); magnification range: X200 to X1,500,000; point-to-point resolution: 0.20 nm and lattice resolution: 0.14 nm; digital camera enable of capturing both high resolution images and electron diffraction patterns.[25]

After switching on the TEM, all air, gun and gas pressure were checked, the acceleration voltage was increased, and the beam current was stabilized. We inserted the sample into the TEM Specimen chamber with either the single tilt holder or double tilt holder. The gun alignment was adjusted for the best focus to get a better image in all modes such as HRTEM, STEM, and SADP. We also analyzed EDS spectra with the help of EDAX software.

3.11 NMR Spectroscopy

Nuclear Magnetic Resonance (NMR) spectroscopy surrounds a sample with a magnetic field and convert the nuclei of atoms with nonintegrated spin into an equilibrium condition among ground and excited spin state. Absorption of radio wave radiation can produce transition between ground and excited sates. The frequency shift (in ppm) versus a standard for radio wave absorption by an atom in a particular compound is characteristics of its position in the molecule. Both hydrogen and carbon atoms are active for the NMR affect. [27] We used the Bruker ULTRASHIELD^{TM} 400 instrument and deuterated DMSO solvent for proton and carbon NMR spectroscopy analysis. Samples were taken to the Chemistry department of the University of Akron, Ohio for solid-state NMR analysis.

Chapter 4: Results and Discussion

4.1 Product Summary:

Table 1: Summary of reactions and products

Sample information	Reaction Conditions	Notes
[A]	0.4:0.4 mmol= $Co(NO_3)_2$: 1,3,5- Benzene tricarboxylic acid; 10ml DMF (solvent) Heating Condition: 120 ^{0}C 96 hours; Room cooling Temp- 24 hours	Powder sample
[B]	0.72:0.36 mmol=Anhydrous $Co(NO_3)_2$: 1,4-Cyclohexane dicarboxylic acid; 6ml Anhydrous DMF (solvent) Heating Condition: 150 ^{0}C- 24 hours; 120 ^{0}C- 24 hours; 100^{0}C- 24 hours; 60-^{0}C- 24 hours; Room Temp- 24 hours	Powder sample
[C] [Co_6 ($H_3BTCA)_8$ $(DMF)_{18}(CO_2)_3]_n$. $2H_2O$] (from Single crystal X-ray diffraction data)	0.36:0.36 mmol=Anhydrous $CoCl_2$: 1,3,5-Benzene tricarboxylic acid; 6ml DMF Heating Condition: 150 ^{0}C- 24 hours; 120 ^{0}C- 24 hours; 100^{0}C- 24 hours; 60-^{0}C- 24 hours; Room Temp- 24 hours	Powder and crystal samples
[D] [CoO_3 (H_3BTCA) $(DMF)_3]_n$ (from Single crystal X-ray diffraction data)	0.36:0.72 mmol= Anhydrous $CoCl_2$: 1,3,5-Benzene tricarboxylic acid; 6ml Anhydrous DMF Heating Condition: 150 ^{0}C- 24 hours; 120	Powder and crystal samples

	^{0}C- 24 hours; 100^{0}C- 24 hours; 60-^{0}C- 24 hours; Room Temp- 24 hours	
[E] [Co_3 (H_3BTCA) (DMF)$_6$(CO_2)$_3$]$_n$ (from Single crystal X-ray diffraction data)	0.36:0.36 mmol=Anhydrous $CoCl_2$: 1,3,5-Benzene tricarboxylic acid; 6ml DMF Heating Condition: 150 ^{0}C- 24 hours; 120 ^{0}C- 24 hours; 60-^{0}C- 48 hours; Room Temp- 24 hours	Powder and crystal samples
[F] [Co (H_3BTCA)$_4$ (Imidazole)]$_n$	0.5:0.5:0.5 mmol= Anhydrous $CoCl_2$: 1,3,5-Benzene tricarboxylic acid: Imidazole; 6ml DMF: MeOH=1:1 (solvent) Heating Condition: 150 ^{0}C- 24 hours; 120 ^{0}C- 24 hours; 90 ^{0}C- 24 hours; 60-^{0}C- 24 hours; Room Temp- 24 hours	Powder and crystal samples
[G] [Co (H_3BTCA)$_3$ (DMF)]$_n$ (from single crystal X-ray diffraction data)	0.5:0.5:1.0 mmol= Anhydrous $CoCl_2$: 1,3,5-Benzene tricarboxylic acid: Imidazole; 10ml DMF: EtOH=1:1 (solvent) Heating Condition: 150 ^{0}C- 24 hours; 120 ^{0}C- 24 hours; 90 ^{0}C- 24 hours; 60-^{0}C- 24 hours; Room Temp- 24 hours	Powder and crystal samples
[H] [Co (H_3BTCA)$_3$ (DMF)$_2$]$_n$ (from single crystal X-ray diffraction data)	1:2:2 mmol= Anhydrous $CoCl_2$: 1,3,5-Benzene tricarboxylic acid (1,3,5-BTCA):4,4'- Trimethylene-dipyridine; 12mL DMF	Powder and crystal samples

	Heating Condition: 150 ^{0}C- 24 hours; 120 ^{0}C- 24 hours; 90 ^{0}C- 24 hours; 60-^{0}C- 24 hours; Room Temp- 24 hours	
[I] [Co (H_3BTCA)$_3$ (DMF)$_3$]$_n$ (from single crystal X-ray diffraction data)	0.5:0.5:0.5 mmol= Anhydrous CoCl2: 1,3,5- Benzene tricarboxylic acid: Imidazole; 6ml DMF Heating Condition: 150 ^{0}C- 24 hours; 80 ^{0}C- 24 hours; Room Temp- 24 hours	Powder and crystal samples
[J] [Co (H_3BTCA)$_4$ (DMF)$_3$]$_n$ (from single crystal X-ray diffraction data)	1:3 mmol=Anhydrous $CoCl_2$: 1,3,5-Benzene tricarboxylic acid; 10mL DMF Heating Condition: 150 ^{0}C- 24 hours; 80-^{0}C- 24 hours; Room Temp- 24 hours	Powder and crystal samples

4.2 Detailed Synthesis Route and Characterization with Discussion

[A] Zero-dimensional Cobalt-based Compound

0.116 g $Co(NO_3)_2$*$6H_2O$ (0.4 millimoles) and 0.0688g 1,3,5- benzenetricarboxylic acid (0.4 millimoles) were mixed with six mL DMF in the Teflon autoclave. After mixing, the solution was sealed in a steel vessel and heated at 120 ^{0}C for 96 hours. Then the products were cooled to room temperature. A pink colored powder sample was produced, and a suitable characterization performed.

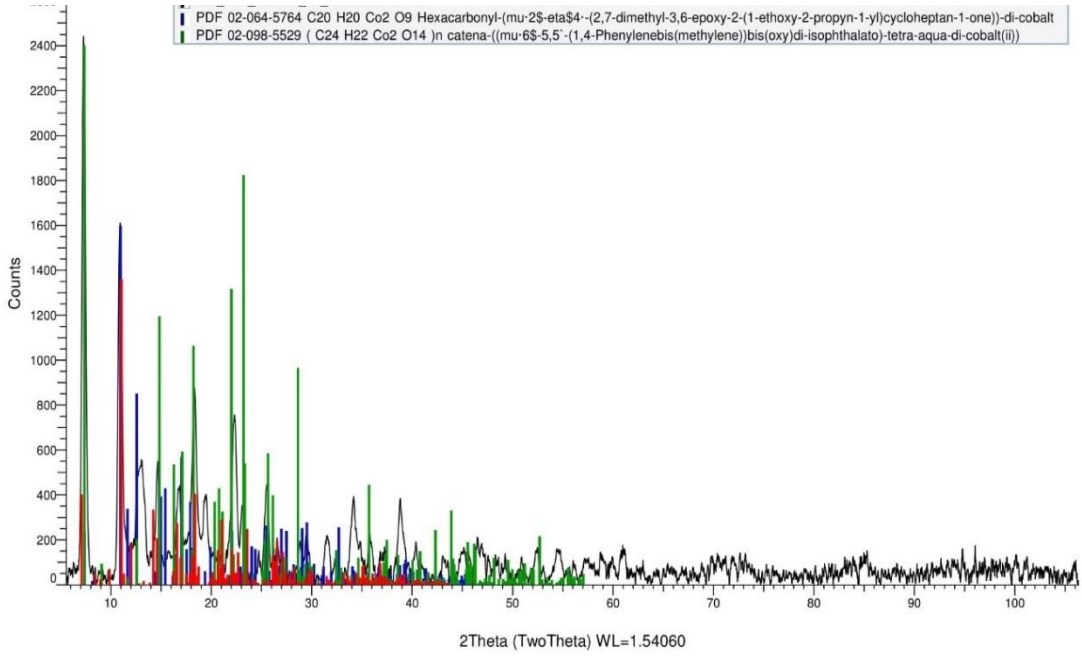

Fig. 11: PXRD pattern of sample [A] with matching data from Cambridge Database

From the figure 11, sample [A] was not properly matched with the database, and the crystallinity of the powder sample was very poor. We did not get enough data and information from this synthesis route so that we changed the base metal as anhydrous cobalt nitrate salt from the next batch.

[B] Zero-dimensional Cobalt-based Compound

In this synthesis route, 0.1376 g anhydrous $Co(NO_3)_2$ (0.72 millimoles) and 0.0619g 1,4-cyclohexanedicarboxylic acid (0.36 millimole) were mixed with six mL DMF in the Teflon autoclave. After mixing, the solution was sealed in a steel vessel and heated at 150 ^{0}C for 24 hours. The products were slowly cooled. A purple colored powder sample was produced, and a suitable characterization performed.

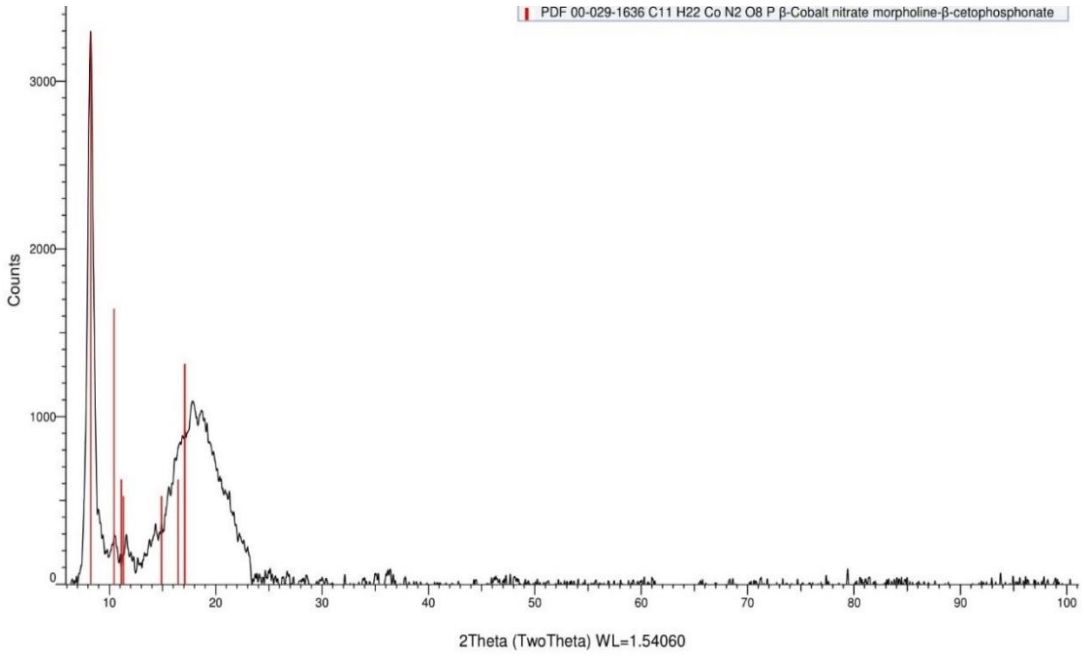

Fig. 12: PXRD pattern and database compound matching of [B]

From the figure 12, sample [B] didn't properly match with the database information, and only two peaks were found; the crystallinity of the powder sample was very poor. We did not get enough information from this synthesis route so that we changed the base metal compound to $CoCl_2$ for the next batch.

[C] One-dimensional Cobalt Complex: $[Co_6(H_3BTCA)_8(DMF)_{18}(CO_2)_3]_n.\ 2H_2O$]

0.0467 g anhydrous $CoCl_2$ (0.36 millimole) and 0.0756g 1,3,5- benzenetricarboxylic acid (0.36 millimole) were mixed with 6 mL solvent in the Teflon autoclave. After mixing, the solution was sealed in a steel vessel and heated at 150 ^{0}C for 24 hours. The products were slowly cooled at 120 ^{0}C for 24 hours, then 90 ^{0}C for 24 hours, after that 60 ^{0}C for 24 hours and lastly, room cooling for 24 hours. A pink colored crystal and powder samples were produced, and suitable characterization performed.

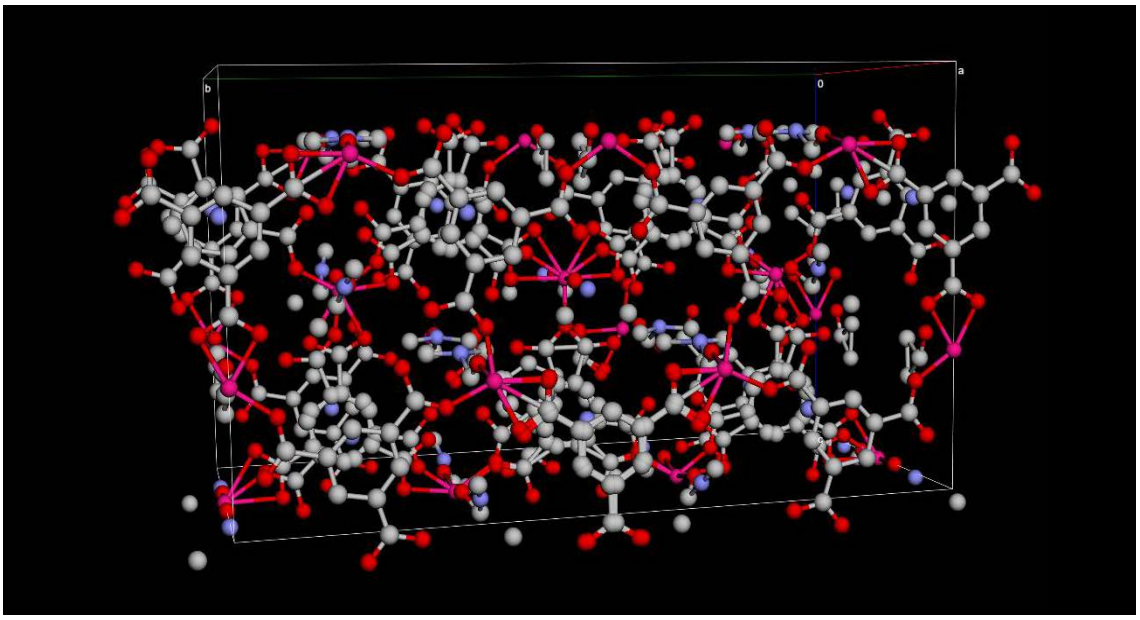

Fig. 13: Unit cell structure of **[Co_6 ($H_3BTCA)_8$ $(DMF)_{18}(CO_2)_3]_n$. $2H_2O$]** from single crystal XRD data (hydrogen atoms omitted for more clarity, red sphere-oxygen, ash or gray sphere- carbon, light red or rose: cobalt, blue -nitrogen atoms representation.)

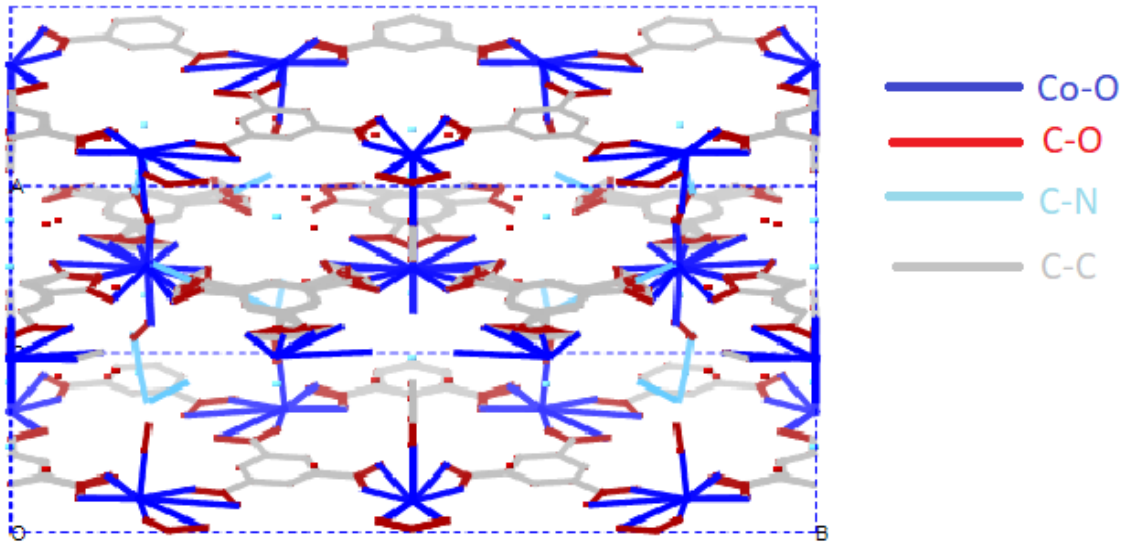

Fig. 14: Stick model (SXRD data) of [C]: **[Co_6 ($H_3BTCA)_8$ $(DMF)_{18}(CO_2)_3]_n$. $2H_2O$]**

Table 2: Crystal information of **[Co_6 (H_3BTCA)$_8$ (DMF)$_{18}$(CO_2)$_3$]$_n$. 2H_2O]**

Structure Type:	Crystal	**Asymmetric Unit:**	99 sites
Chemical Formula:	$C_{129}H_0Co_6N_{18}O_{74}$	**Unit Cell:**	442 sites per unit cell
Display Formula:	C217 Co21 N36 O117.75	**Site Density:**	0.0642 sites/Å^{3}0.0427 atoms/Å^3
Spacegroup:	*A m m* 2	**Visible Atoms:**	586
	(Polar)	**Cell Volume:**	6880.482 Å^3
Crystal System:	Orthorhombic	**Density:**	1.0825 g/cm^3
a:	14.3125 Å (15)	***M*r:**	3339.05
b:	28.8470 Å (3)	**Radiation type:**	Mo *Kα*
c:	16.6649 Å (14)	**H-atom treatment:**	H-atom parameters not defined

From the SXRD data, it appears to be a network with trimesate and cobalt with some DMF solvent. But the crystal structure is beset by pseudosymmetry and twinning. In this case, twinning may be caused by the loss of symmetry upon cooling. We tried other batches changing reaction conditions and composition for getting better and helpful crystal information.

[D] One-dimensional Cobalt Complex [CoO_3 (H_3BTCA) (DMF)$_3$]$_n$

0.0467g anhydrous $CoCl_2$ (0.36 millimole) and 0.1512g 1,3,5- benzenetricarboxylic acid (0.72 millimole) were mixed with 6 mL DMF in the Teflon autoclave. After mixing, the solution was heated at 150 ^{0}C for 24 hours. The products were slowly cooled at 120 ^{0}C for 24 hours, then 90 ^{0}C for 24 hours, after that 60 ^{0}C for 24 hours and lastly, room cooling for 24 hours. A pink colored crystal and powder samples were produced, and characterization techniques such as SXRD, PXRD, TGA analysis performed.

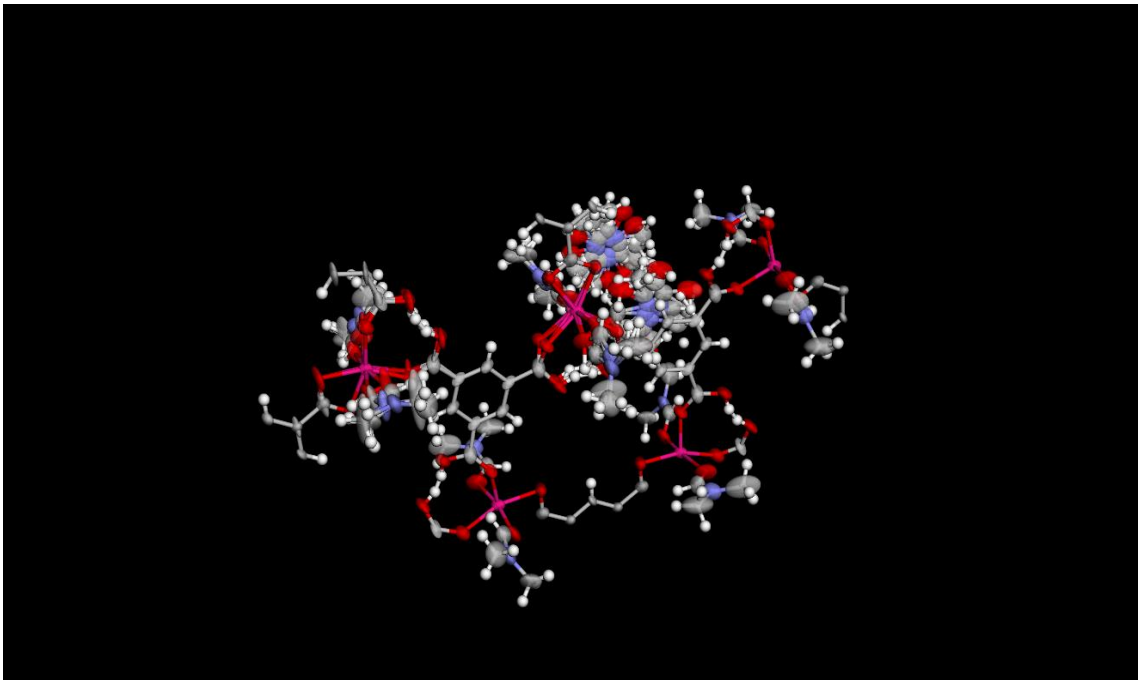

Fig. 15: Hirshfeld surface view from single XRD data (similar as reported paper[28]) of **[Co (H$_3$BTCA) (DMF)$_3$]$_n$**

Table 3: Crystal information of **[Co (H$_3$BTCA) (DMF)$_3$]$_n$** (similar to reported paper[28])

Structure Type:	Crystal	**Asymmetric Unit:**	77 sites
Chemical Formula:	$C_{15}H_{18}CoN_2O_8 \cdot C_3H_7NO$	**Unit Cell:**	2700 sites per unit cell
Display Formula:	C335.968 H453.924 Co18 N53.989 O161.989	**Site Density:**	0.2681 sites/Å^{3}0.1001 atoms/Å^3
Space group:	$R\bar{3}c$	**Visible Atoms:**	2716
Crystal System:	Trigonal	**Cell Volume:**	10072.330 Å^3 (8)
a:	16.6254 Å (5)	**Density:**	1.4431 g/cm^3
c:	42.0780 Å (2)	**Mr:**	486.34

From the SXRD data, we got pretty much a similar structure to the reported structure in the database.[28] We didn't get high-quality data and structure. The cobalt (Co) ion, the two coordinated DMF molecules, and one of the carboxylic acid groups is disordered around a twofold axis close to the cobalt ion. The carboxylic acid groups were controlled to be planar, as they were subjected to an inflexible bond restraint, and their atoms were likely to be isotropic. Two solvent-occupied sites were refined as disordered DMF molecules. The DMF molecules' construction was constrained to be similar as those of the cobalt coordinated DMF molecules, to be planar and more likely to be isotropic. The occupancy ratio for the molecule disordered around the three-fold axis refined to 0.165(10) to 0.168(10) (approximately 1:1).

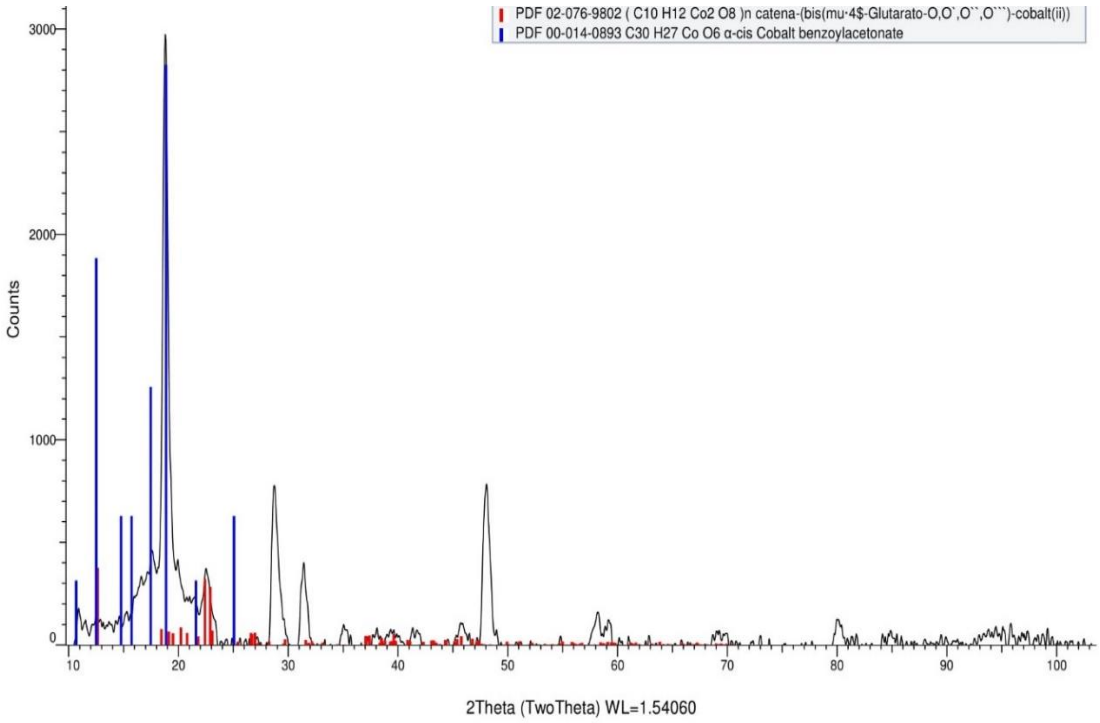

Fig. 16: PXRD pattern of **[Co (H$_3$BTCA) (DMF)$_3$]$_n$**

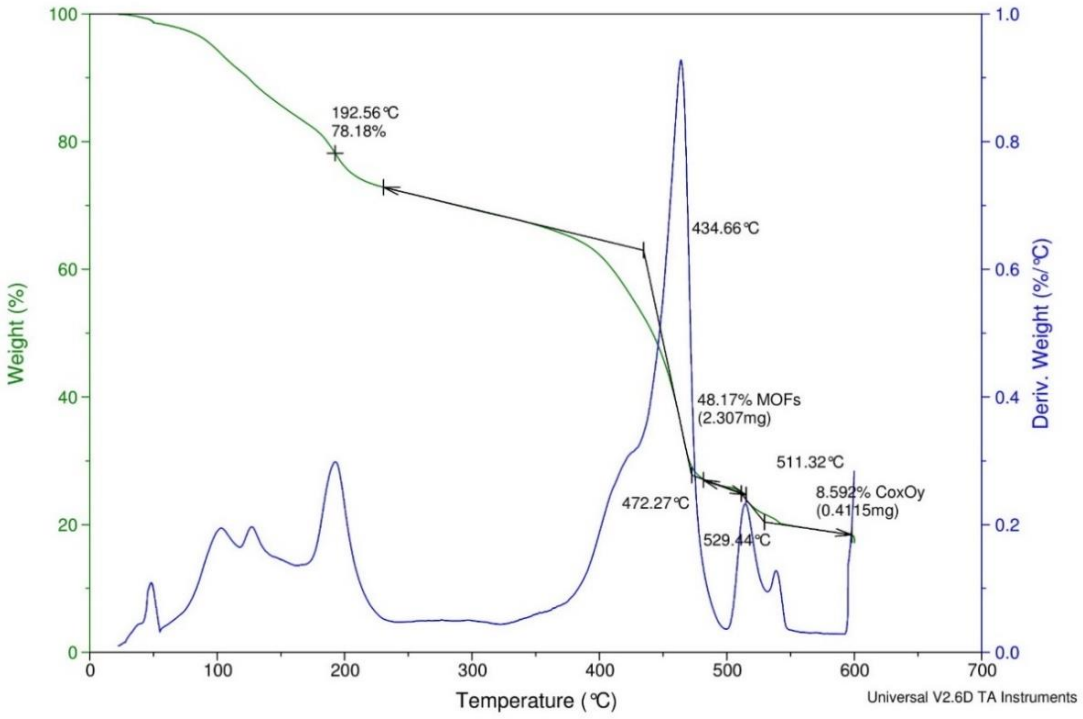

Fig. 17: TGA analysis of **[Co (H3BTCA) (DMF)3]n**

From the figure 16, the produced powder sample's PXRD data principal peak almost matched with the reported data set, and crystallinity of sample is very low. From the TGA analysis, solvent and moisture decomposition last until 200 ^{0}C.

[E] One-dimensional Cobalt Complex [Co3 (H3BTCA) (DMF)6(CO2)3]n

0.0467 g anhydrous $CoCl_2$(0.36 millimole) and 0.0756g 1,3,5- benzenetricarboxylic acid (0.36 millimole) were mixed with 5mL DMF. After mixing, the solution was heated at 150 ^{0}C for 24 hours. The products were slowly cooled at 120 ^{0}C for 24 hours, then 90 ^{0}C for 24 hours, after that 60 ^{0}C for 24 hours and lastly, room cooling for 24 hours. A light purple colored crystal and powder samples were produced, and a suitable characterization performed.

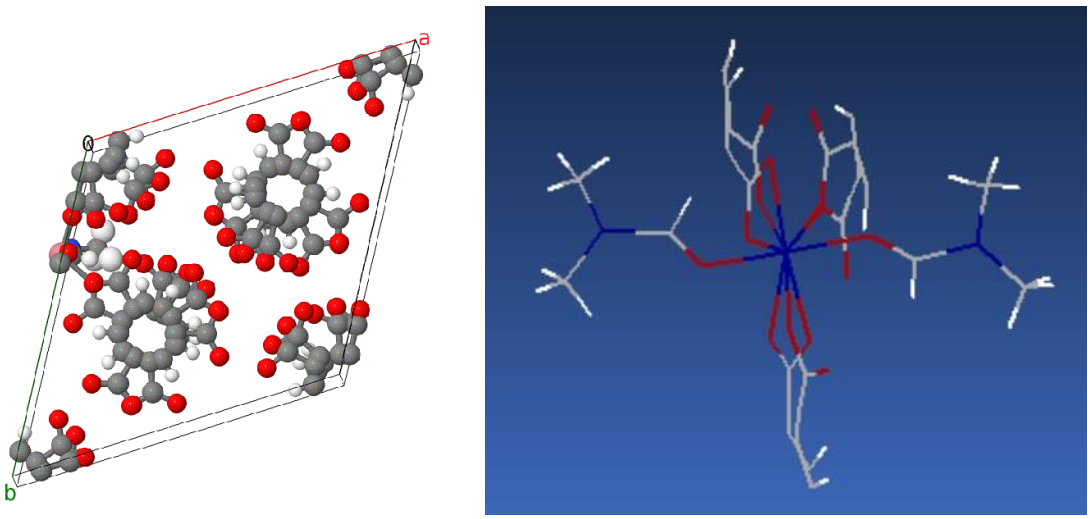

Fig. 18: SXRD data of **$[Co_3(H_3BTCA)(DMF)_6(CO_2)_3]_n$ a.** The unit cell of (hydrogen atoms -white small, red sphere-oxygen, ash or gray sphere- carbon, rose or light pink-cobalt, blue- nitrogen atoms representation **b.** pipe model from SXRD data. (Hexagonal unit cell -Table 9: Appendix A)

We were unable to refine the disorder for the solvate molecules in between the lattice.

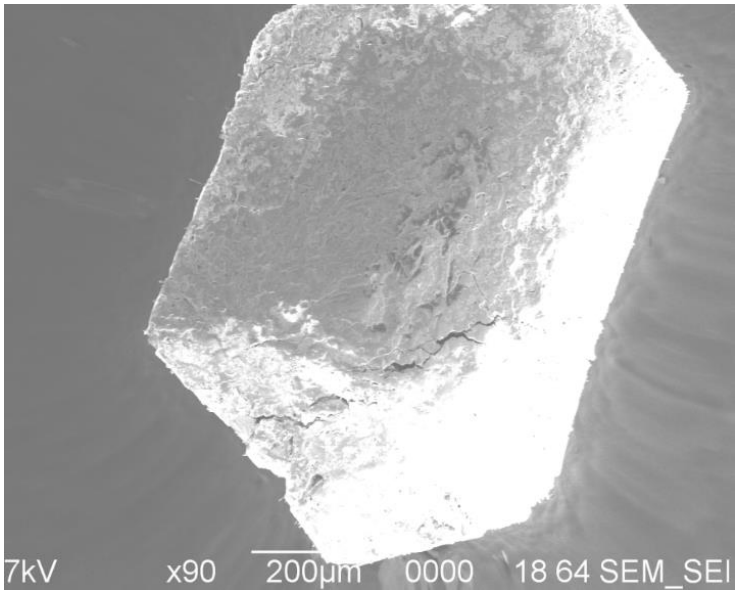

Fig. 19: Lower magnification SEM image of **$[Co_3(H_3BTCA)(DMF)_6(CO_2)_3]_n$** (source: YSU Center for Advanced Materials Analysis)

From SEM analysis, there are distinct pores or cracks in the structure and a surface roughness difference also visible.

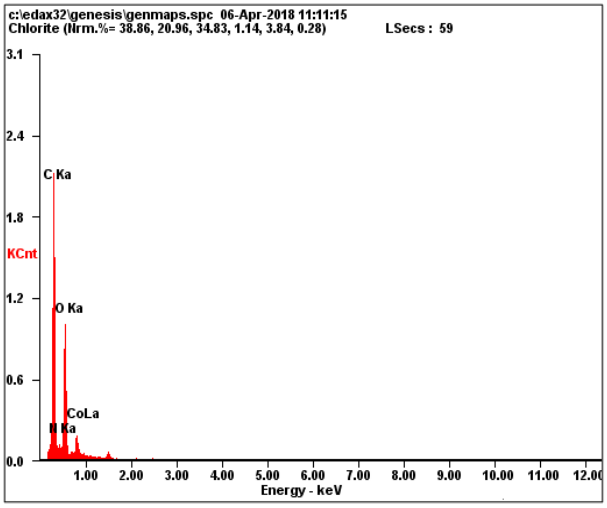

Element	Wt%	At%
CK	50.70	63.38
NK	07.51	08.05
OK	26.23	24.61
CoL	15.56	03.96
Matrix	Correction	ZAF

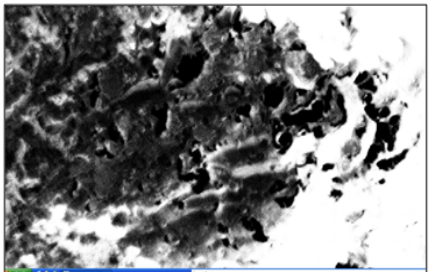

Fig. 20: EDS compositional analysis with ZAF correction method (source: YSU Center for Advanced Materials Analysis)

From the EDS analysis, our produced structure comprises of cobalt, carbon, oxygen, nitrogen, and hydrogen (not shown). The high carbon content suggests that carbon constraints in the benzene ring and the ring may be attached to either oxygen, cobalt or nitrogen.

[F] Three-dimensional Metal-Organic Framework [Co (H_3BTCA)$_4$ (Imidazole)]$_n$

In this synthesis route, 0.0649g anhydrous $CoCl_2$ (0.5 millimoles) and 0.105g 1,3,5-benzenetricarboxylic acid (0.5 millimoles) along with imidazole 0.034g (0.5 millimoles) were mixed with the solvent (6 mL 1:1=DMF: methanol) in the Teflon autoclave. After mixing, the solution was heated at 150 ^{0}C for 24 hours. The products were slowly cooled at 120 ^{0}C for 24 hours, then 90 ^{0}C for 24 hours, after that 60 ^{0}C for 24 hours and lastly, room cooling for 24 hours. Mixed pink and purple colored crystal and powder samples

were produced, and characterization techniques such as SXRD, PXRD, TGA analysis were performed.

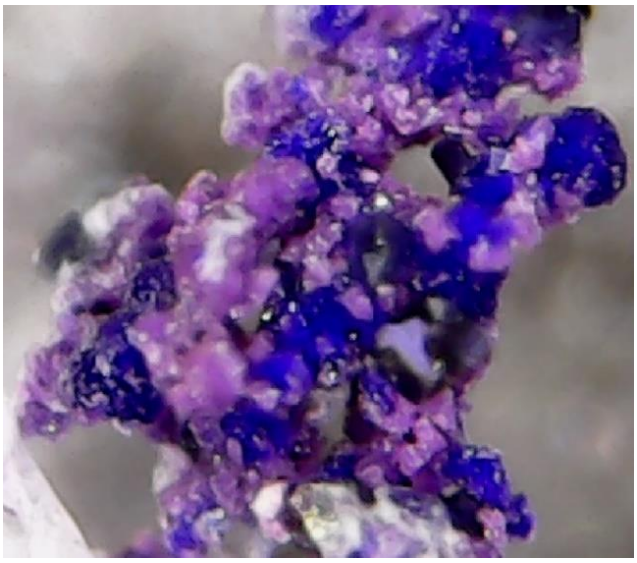

Fig. 21: Optical Microscopy of **[Co (H$_3$BTCA)$_4$ (Imidazole)]$_n$** showing purple and pink color crystals.

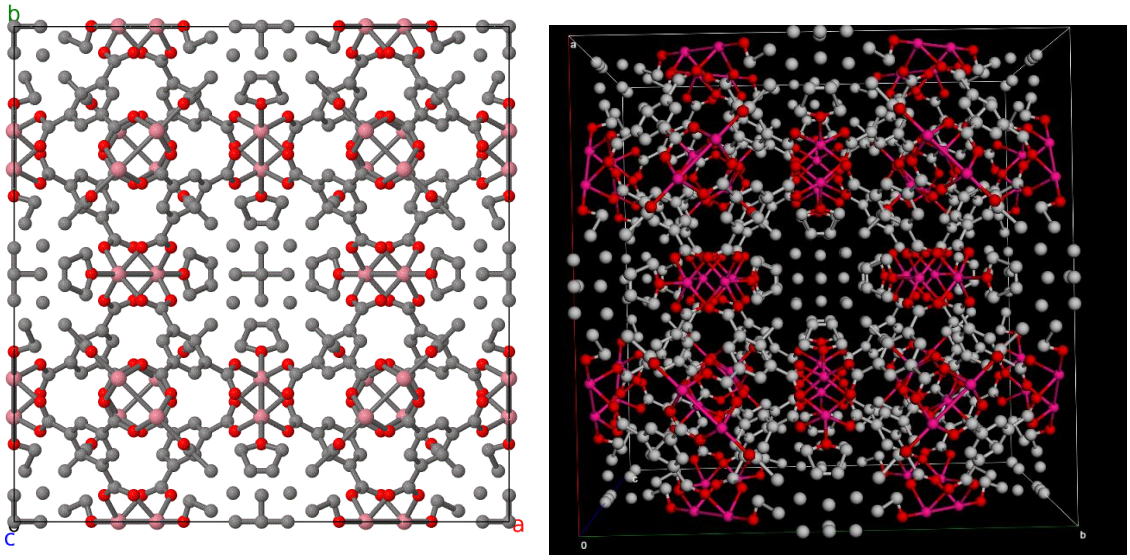

Fig. 22: Single crystal XRD analysis of **[Co (H$_3$BTCA)$_4$ (Imidazole)]$_n$ a.)** Unit cell information in which unit cell is Cubic structure and lattice parameter is 26.6325 Å. **b.)** Hirshfeld surface view (hydrogen atoms omitted for more clarity, red sphere-oxygen, ash or gray sphere- carbon, rose sphere - cobalt)

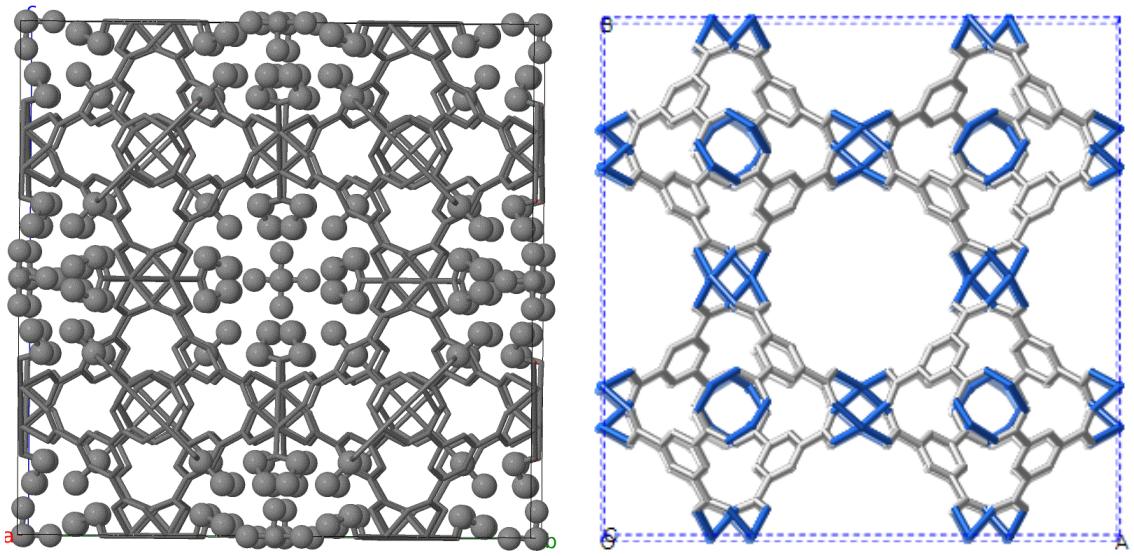

Fig. 23: a. Ball and stick view of [F] with considering solvent. b. Stick view without solvent and third-party linkers (combination of cobalt and trimesate)

Table 4: Crystal information of **[Co (H$_3$BTCA)$_4$ (Imidazole)]$_n$**

Chemical formula	$C_{40}H_{40}CoN_2O_{12}$
M_r	799.67
Crystal system, space group	Cubic, *Fm*3*m*
Temperature (K)	280
a (Å)	26.6325 (12)
V (Å^3)	18890 (3)
Z	16
Radiation type	Mo *K*α
μ (mm^{-1})	0.42
No. of measured, independent and observed [$I > 2\sigma(I)$] reflections	7248, 1376, 1080
R_{int}	0.025
$(\sin \theta/\lambda)_{max}$ (Å^{-1})	0.714
$R[F^2 > 2\sigma(F^2)]$, $wR(F^2)$, S	0.084, 0.272, 2.07
No. of reflections	1376
$(\Delta/\sigma)_{max}$	0.390
$\Delta\rho_{max}$, $\Delta\rho_{min}$ (e Å^{-3})	1.16, −0.72

From the SXRD data, a basic structure was obtained, but it is confusing about the apical position of the cobalt atoms. This might be a partially occupied imidazole, as imidazole was used as a third-party linker. If we could carefully isolate some of the crystals, dissolve them in a suitable deuterated solvent, and try to find how much of each possible ligand and solvent is trapped inside the crystals, then we could find the actual apical position of cobalt. We tried to find out with the EDS and CHNO analysis, but the data could was not conclusive about the apical position of cobalt. Apart from this, our SXRD data support that sample is a three-dimensional channel MOF.

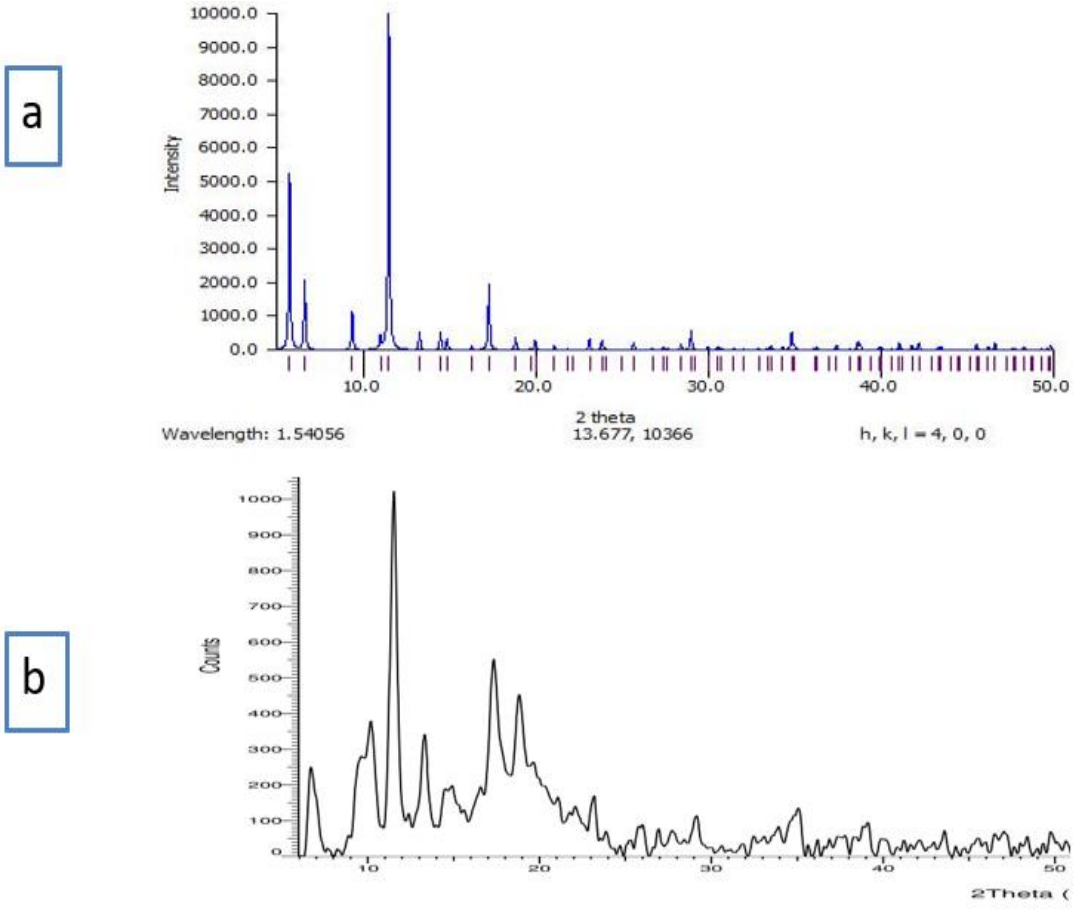

Fig. 24: a. The simulated PXRD pattern of **[Co (H$_3$BTCA)$_4$ (Imidazole)]$_n$** (produced from SXRD data) b. Experimental (lab sample) PXRD pattern of [F]

There are some matched peaks in the simulated and experimental PXRD data. The crystallinity is not so good in the experimental data as simulated data. Before and after activation PXRD data show slight differences in intensity and peak width. (see Appendix B, figures 67 and 68)

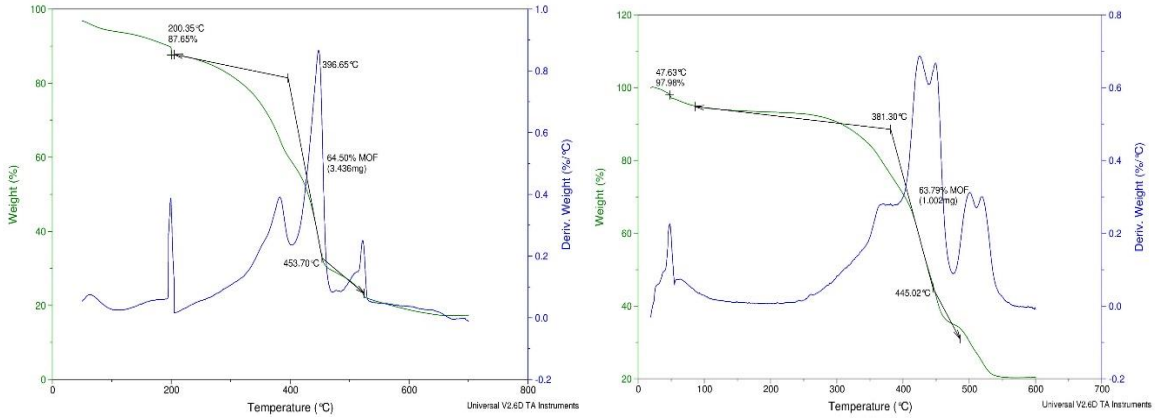

Fig. 25: TGA data of **[Co (H$_3$BTCA)$_4$ (Imidazole)]$_n$** a. Before activation b. after activation.

There was not much difference in the TGA between the before and after activation samples. As expected loss of solvent is absent in the after activation.

Experiment 1: Experiment 1 Pre-treatment and First BET

Analysis Type: Physisorption Surface Area
Calibration: (292_0022) BET calibration-September 13, 2011
Measured Flow Rate: 50.13 cm³ STP/min
Signal Offset: 6.54357
Signal Inverted: No

Peak Summary

Experiment Number	Active Concen-tration	Relative Pressure	Cumulative Quantity (µmol/g)	1 / [Q(Po/P-1)] (g/µmol)
1	0.0000	0.0000	-2.79188	0.0000000
1	0.0000	0.0000	-3.50930	0.0000000
1	0.0000	0.0000	-4.04272	0.0000000

BET Analysis Summary

Atmospheric Pressure: 731 mmHg
Saturated Pressure: 775.00 mmHg
Cross-Sectional Area: 0.162 nm²
Monolayer Volume: 2.899 cm³/g
BET Surface Area: 12.6189 m²/g

BET Single Point Tabular Report

Experiment 1: Experiment 1 Pre-treatment and First BET

Analysis Type: Physisorption Surface Area
Calibration: (292_0022) BET calibration-September 13, 2011
Measured Flow Rate: 50.13 cm³ STP/min
Signal Offset: 6.51291
Signal Inverted: No

Peak Summary

Experiment Number	Active Concen-tration	Relative Pressure	Cumulative Quantity (µmol/g)	1 / [Q(Po/P-1)] (g/µmol)
1	0.0000	0.0000	-1.98363	0.0000000
1	0.0000	0.0000	-3.03435	0.0000000
1	0.0000	0.0000	-3.77186	0.0000000

BET Analysis Summary

Atmospheric Pressure: 731 mmHg
Saturated Pressure: 775.00 mmHg
Cross-Sectional Area: 0.162 nm²
Monolayer Volume: 2.705 cm³/g
BET Surface Area: 11.7734 m²/g

Fig. 26: BET analysis of [F] a. Before activation and b. after activation

From the figure 26, the results show a very small value for BET surface area. Because of the structural topology and exceptional void space, three-dimensional metal organic framework should have attained the higher surface area. This instrument may be useful for chemisorption processes but for our BET analysis; physisorption techniques need to be performed.

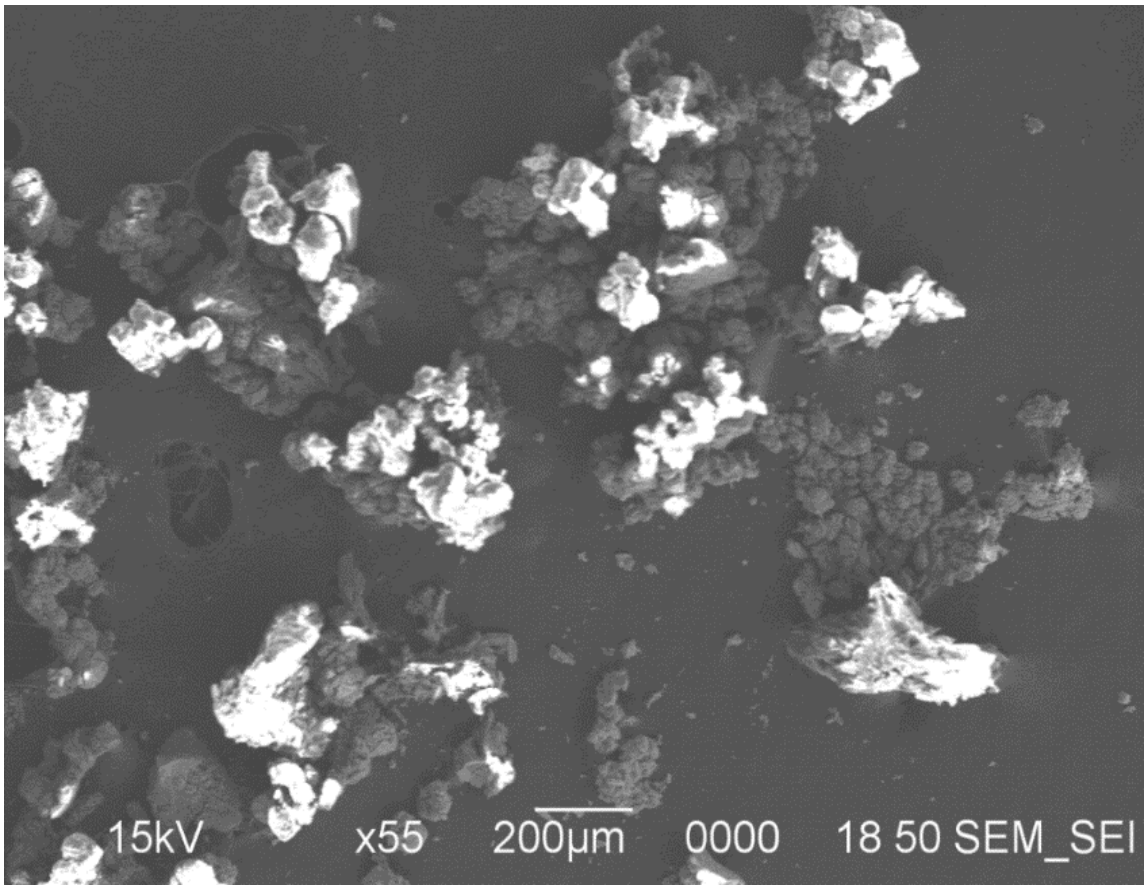

Fig. 27: Lower magnification (x55) SEM image of **[Co (H$_3$BTCA)$_4$ (Imidazole)]$_n$**

Figure 27 shows the powder cluster agglomeration. Inter-particle void space is also visible in the cluster.

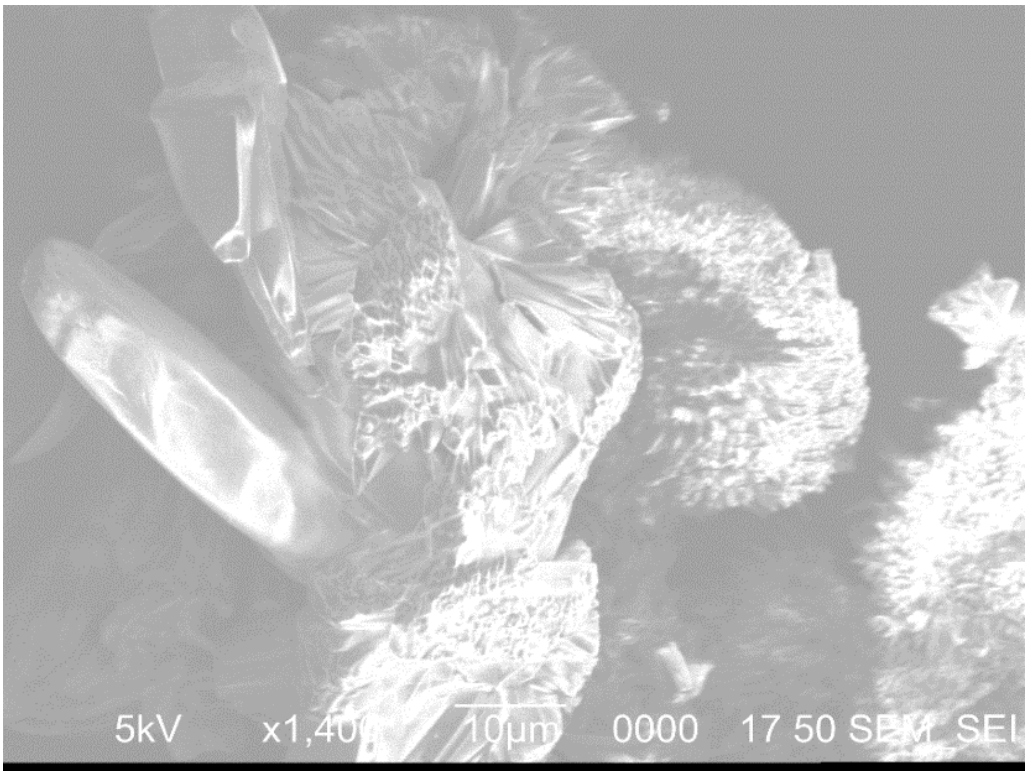

Fig. 28: SEM microstructure of **[Co (H$_3$BTCA)$_4$ (Imidazole)]$_n$**

Fig. 28 shows the morphology of structure [F]. It looks like dendritic structures and layer patterns are visible in the structure, which indicates that our sample has significant porosity in the structure.

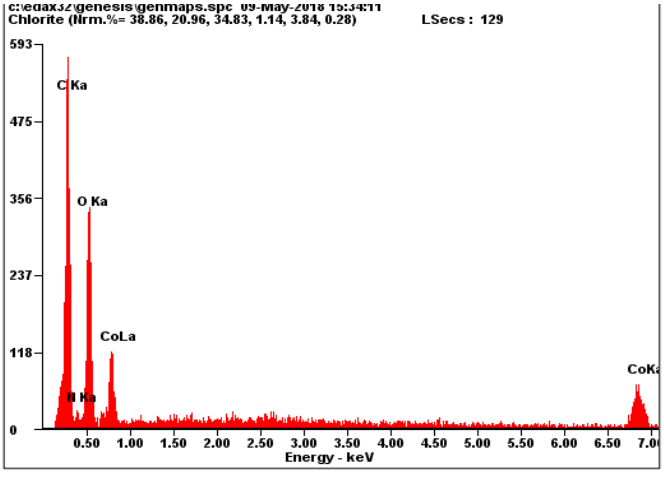

Element	*Wt%*	*At%*
CK	48.30	62.22
NK	04.12	04.56
OK	29.42	28.46
CoK	18.15	04.77
Matrix	Correction	ZAF

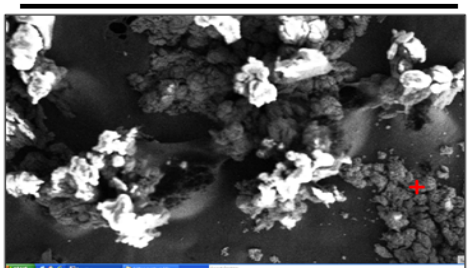

Fig. 29: EDS compositional analysis with ZAF correction method of [F]

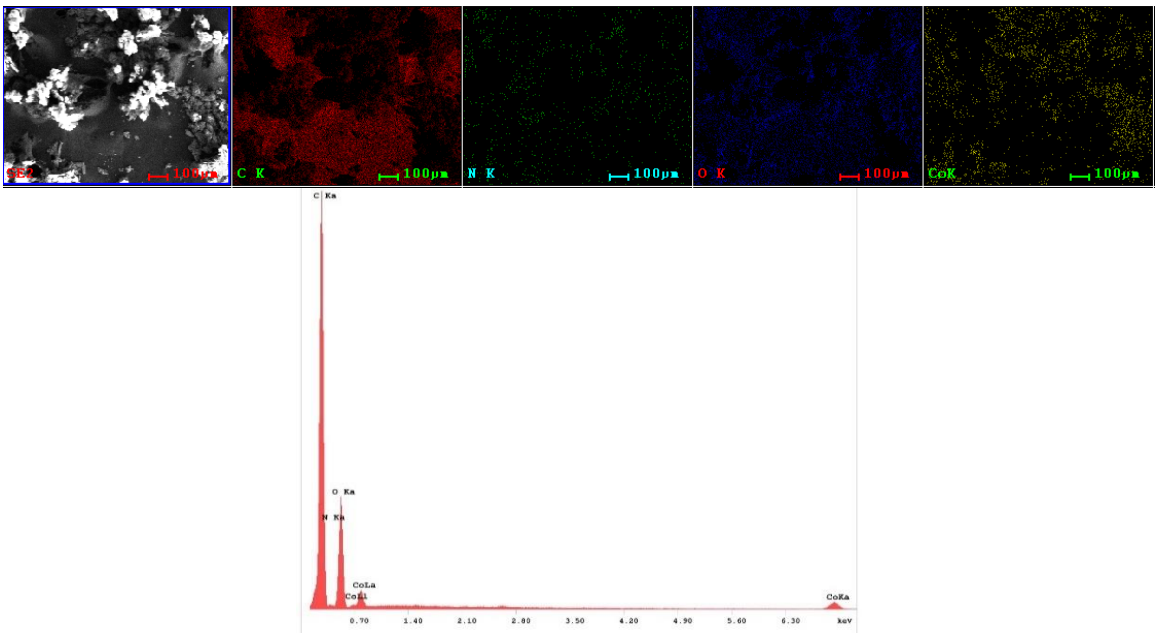

Fig. 30: Elemental Mapping with corresponding elemental analysis from EDS analysis.

From the EDS analysis, our sample comprises cobalt, carbon, oxygen, and nitrogen.

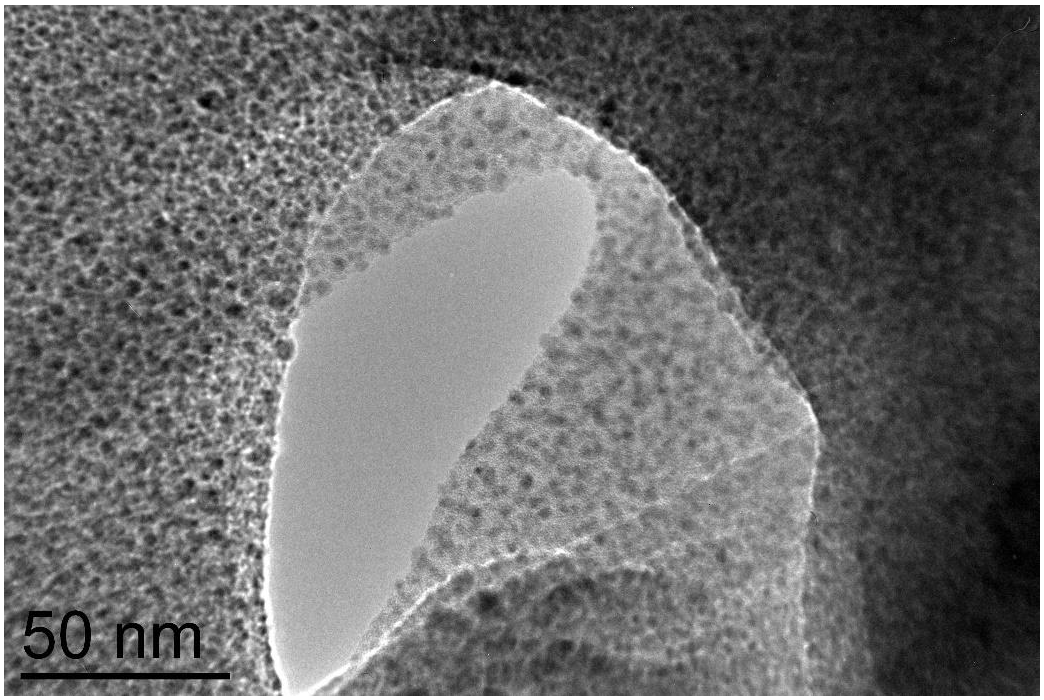

Fig. 31: Transmission Electron Microscopy (TEM) image in nanoscale of **[Co $(H_3BTCA)_4$ (Imidazole)]$_n$** (source: YSU Center for Advanced Materials Analysis)

From the TEM image, the atomic orientation configuration was found, and a small fraction of voids may present in the structure.

[G] Three-dimensional Metal-organic Framework [Co (H$_3$BTCA)$_3$ (DMF)]$_n$

Under solvothermal synthesis condition 0.5 millimoles anhydrous $CoCl_2$ (0.0649g) and 0.5 millimoles 1,3,5- benzenetricarboxylic acid (0.105g) along with 1 millimoles imidazole (0.068g) were mixed with 10 mL 1:1=DMF: ethanol in the Teflon autoclave. After mixing, the solution was heated at 150 ^{0}C for 24 hours. The products were slowly cooled at 120 ^{0}C for 24 hours, then 90 ^{0}C for 24 hours, after that 60 ^{0}C for 24 hours and lastly, standing at ambient temperature for 24 hours. A pink colored crystal and powder samples were produced, and characterization techniques such as SXRD, PXRD, TGA analysis performed.

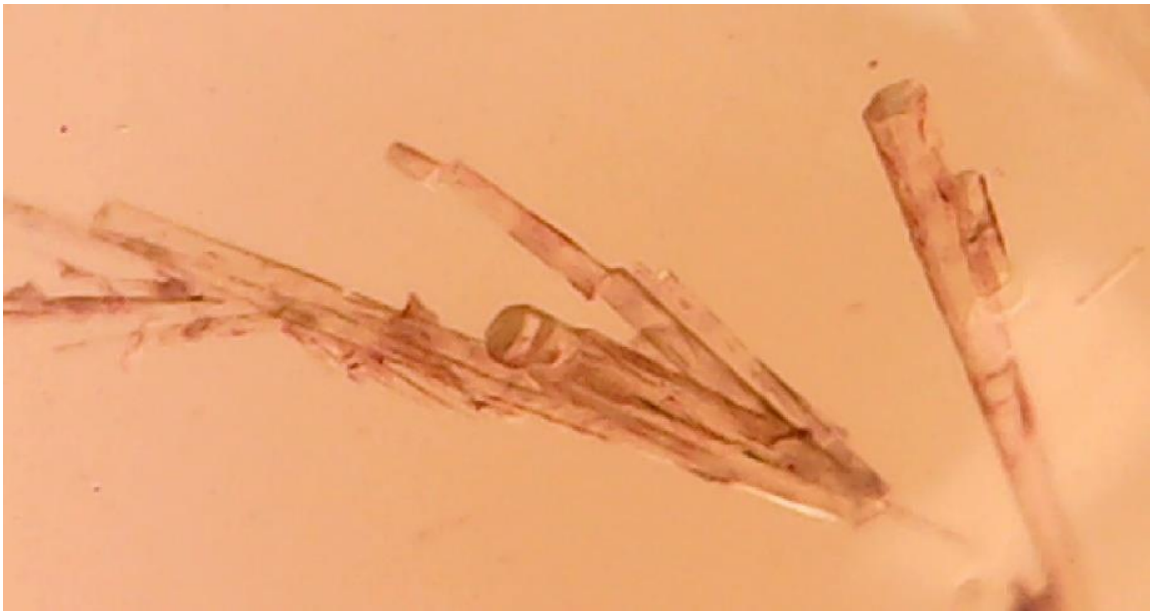

Fig. 32: Optical Microscopy of **[Co (H$_3$BTCA)$_3$ (DMF)]$_n$** which indicate the rod or tube-like structure. (powder and crystal samples found)

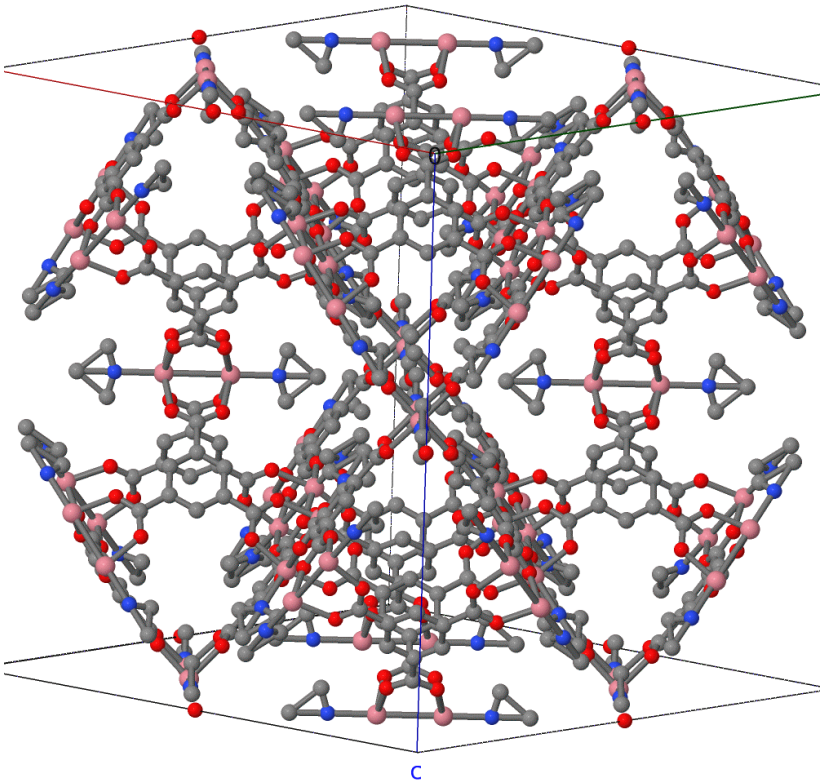

Fig. 33: Single crystal XRD analysis of **[Co (H3BTCA)3 (DMF)]n** Ball and stick model (hydrogen atoms omitted for more clarity, red sphere-oxygen, ash or gray sphere- carbon, rose or light pink-cobalt, blue -nitrogen atoms representation.)

Table 5: Crystal information of **[Co (H3BTCA)3 (DMF)]n**

Chemical formula	$C_{30}H_{30}CoN_2O_{10}$
M_r	637.49
Crystal system, space group	Cubic, *Fm3m*
Temperature (K)	273
a (Å)	26.6565 (7)
V (Å^3)	18941.3 (15)
Z	24
Radiation type	Cu *K*α
μ (mm^{-1})	4.75
R_{int}	0.071
$(\sin \theta/\lambda)_{max}$ (Å^{-1})	0.599
$R[F^2 > 2\sigma(F^2)]$, $wR(F^2)$, *S*	0.122, 0.335, 1.52
$\Delta\rho_{max}$, $\Delta\rho_{min}$ (e Å^{-3})	1.34, −1.00

From the SXRD data, it is very difficult to provide information about what is attached to the sixth position at the cobalt. By charge measuring, it should be neutral, unless there are cations in the voids (DMF solvent). It seems to be something like dimethyl ammonium or DMF solvent. A similar unit cell is found in the database.[29] That reported structure has chlorine atom but there are no chlorine atoms in our structure. We need to perform a chemical analysis that would help with determining what is attached to the Co atom (sixth position). From the EDS analysis (Fig. 74: Appendix D), the compound contains carbon, nitrogen, oxygen, and cobalt and the sixth position of cobalt might be DMF solvent, which is associated in the MOF structure.

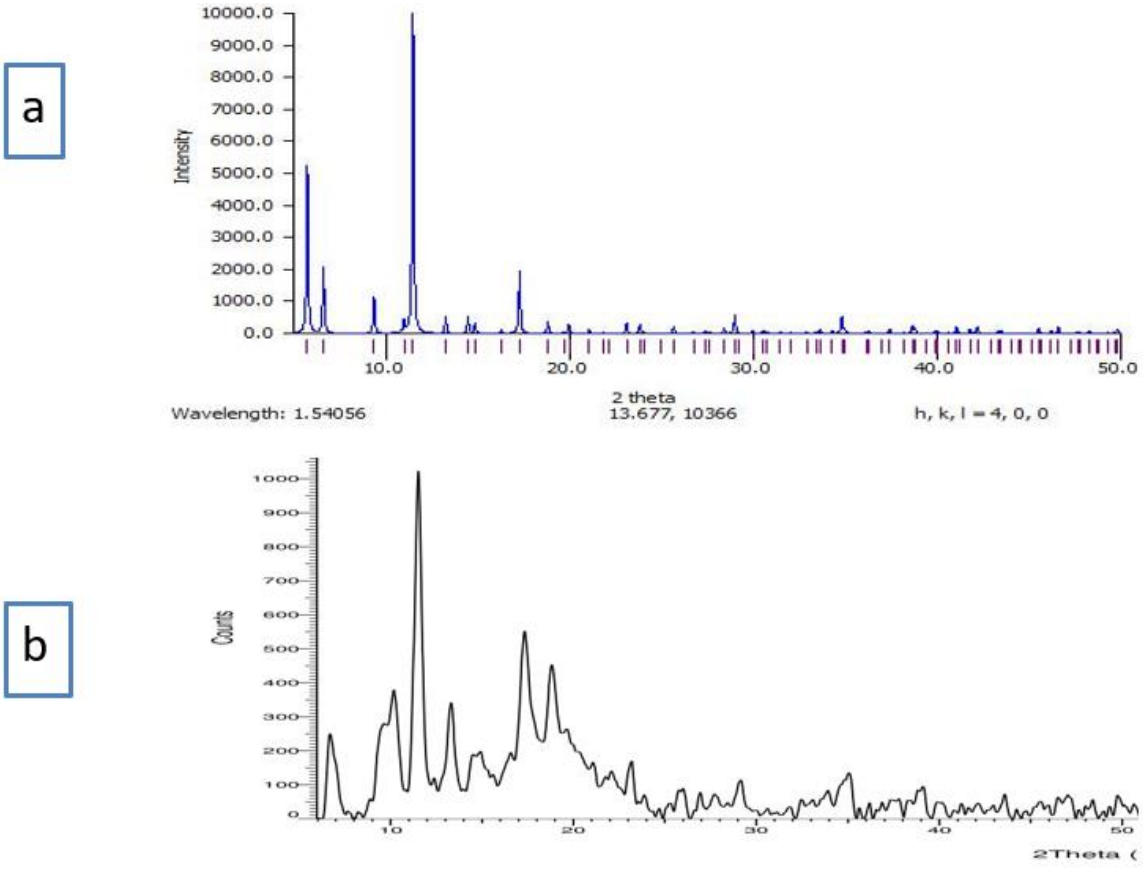

Fig 34: a. Simulated PXRD pattern **[Co (H$_3$BTCA)$_3$ (DMF)]$_n$** (produced from SXRD data) b. Experimental (lab sample) PXRD data.

From the experimental PXRD data, a match was not found which means these materials are completely new.

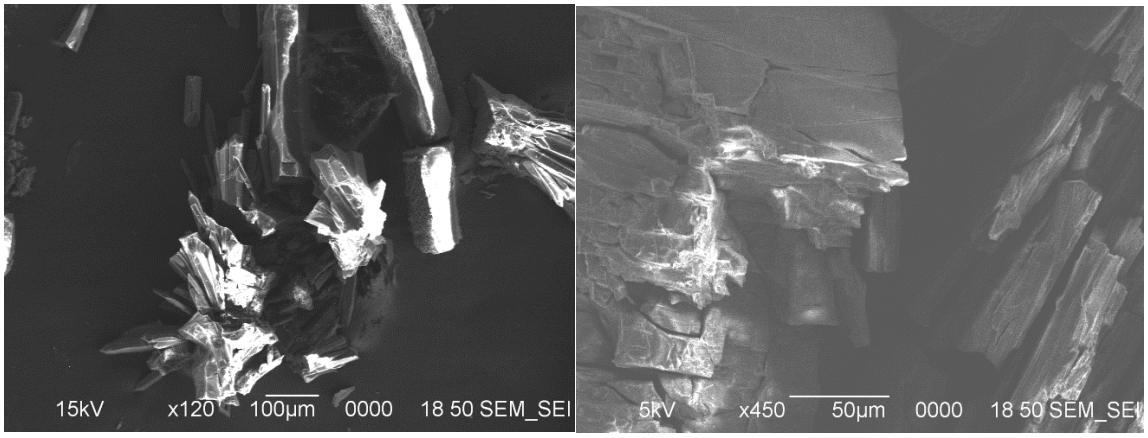

Fig. 35: Secondary Electron Images (SEI) data from SEM analysis of **[Co (H$_3$BTCA)$_3$ (DMF)]$_n$**

From the SEM analysis, the MOF structure looks like a three-dimensional layered structure.

[H] One-dimensional Cobalt Complex [Co (H$_3$BTCA)$_3$ (DMF)$_2$]$_n$

Under solvothermal synthesis condition, 0.1296g anhydrous $CoCl_2$ (1 millimoles) and 0.42g 1,3,5- benzenetricarboxylic acid (2 millimoles) along with 4,4-trimethylenedipyridine 0.396g (2 millimoles) was mixed with six mL 1:1=DMF: methanol in the Teflon autoclave. After mixing, the solution was heated at 150 ^{0}C reaction temperature for 24 hours. Then products were slowly cooled at 120 ^{0}C for 24 hours, then 90 ^{0}C for 24 hours, after that 60 ^{0}C for 24 hours and lastly, standing at room temperature for 24 hours. A purple colored crystal and powder samples were produced, and a suitable characterization analysis was performed.

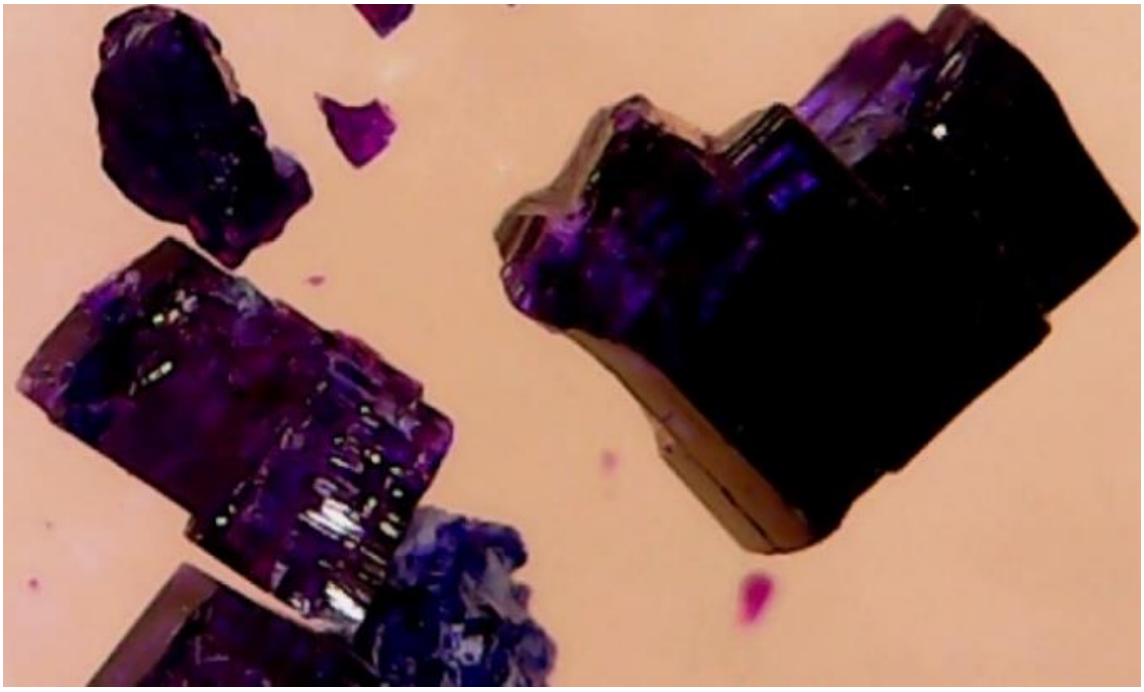

Fig. 36: Optical Microscopy image of **$[Co(H_3BTCA)_3(DMF)_2]_n$**

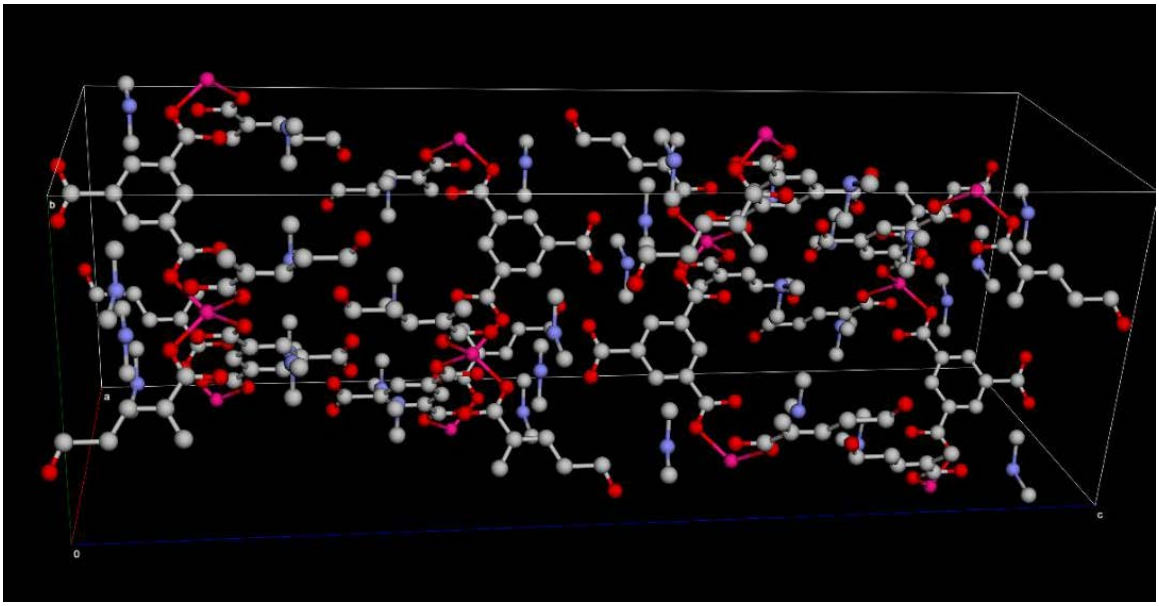

Fig. 37: Single crystal XRD analysis of **$[Co(H_3BTCA)_3(DMF)_2]_n$** (Hirshfeld surface view: red sphere-oxygen, ash or gray sphere- carbon, rose- cobalt, blue-nitrogen, hydrogen atoms omitted for more clarity)

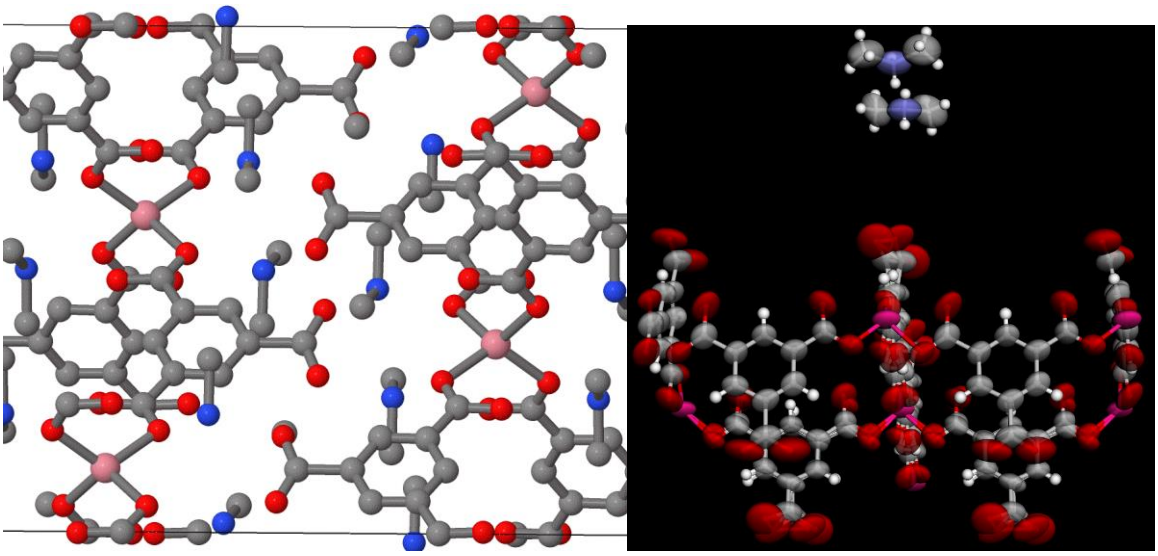

Fig. 38: a. Ball and stick view of **[Co (H$_3$BTCA)$_3$ (DMF)$_2$]$_n$** from SXRD data b. Hirshfeld molecular view

Table 6: Crystal information of **[Co (H$_3$BTCA)$_3$ (DMF)$_2$]$_n$**

Chemical formula	$C_{18}H_6CoN_4O_{12}\cdot 4(C_2H_8)$
M_r	657.53
Crystal system, space group	Orthorhombic, *Fddd*
Temperature (K)	280
a, *b*, *c* (Å)	13.7301 (19), 14.794 (2), 43.111 (5)
V (Å^3)	8757 (2)
Z	8
Radiation type	Mo *K*α
μ (mm^{-1})	0.44
Crystal size (mm)	0.21 × 0.17 × 0.10
T_{min}, T_{max}	0.526, 0.746
No. of measured, independent and observed [$I > 2\sigma(I)$] reflections	15080, 2551, 1777
R_{int}	0.096
$(\sin\theta/\lambda)_{max}$ (Å^{-1})	0.661
$R[F^2 > 2\sigma(F^2)]$, $wR(F^2)$, *S*	0.090, 0.261, 1.07
No. of reflections	2551
No. of parameters	191
No. of restraints	178
$\Delta\rho_{max}$, $\Delta\rho_{min}$ (e Å^{-3})	1.18, −0.63

From the SXRD data, the tricarboxylate ligand and a dimethyl ammonium cation are 1:1 disordered around a two-fold axis. The carboxylate group and the benzene ring and directly adjacent C-atoms were each controlled to be a planar structure. The structure contains eight independent solvent accessible voids, and there were no substantial electron density peaks in the solvent accessible voids. From the information, we can't tell the disordered pyridines attached the Co ions which are also partially occupied. But from the structure analysis of SXRD data, this structure looks like one-dimension Cobalt coordinated complex.

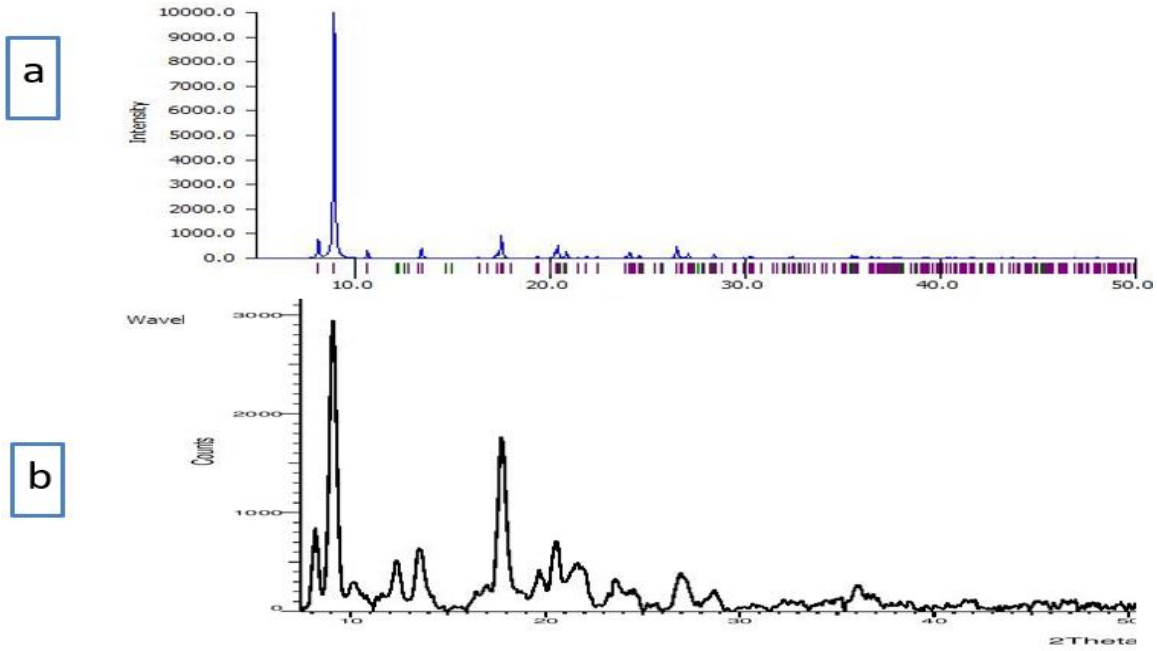

Fig. 39: **a**. The simulated PXRD pattern (produced from SXRD data) **b.** experimental PXRD pattern of **$[Co(H_3BTCA)_3(DMF)_2]_n$**

From the PXRD analysis, there are few similarities between the simulated and experimental PXRD pattern, but the degree of crystallinity was very poor. An experimental sample pattern also matched with the database, but no data completely matched with our compound.

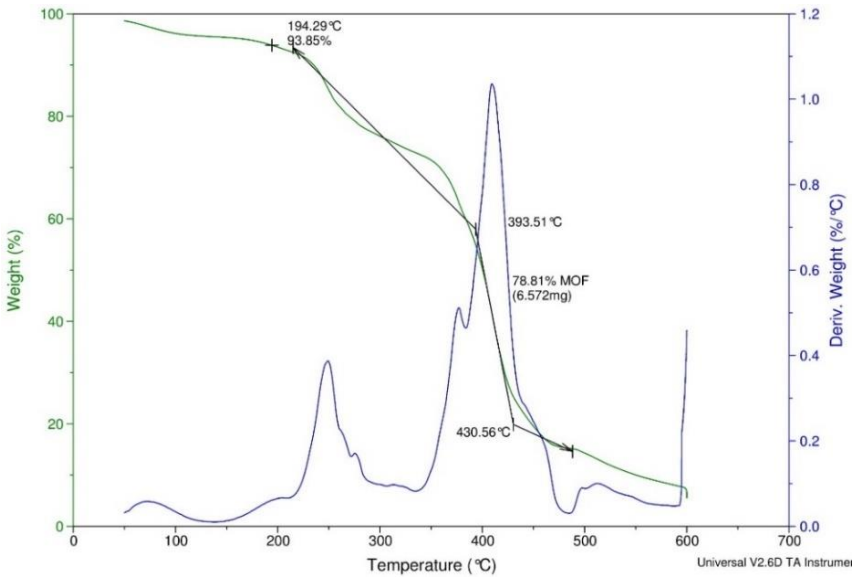

Fig. 40: TGA analysis of **[Co (H$_3$BTCA)$_3$ (DMF)$_2$]$_n$**

TGA analysis shows the thermal stability and decomposition profile of our sample. Decomposition starts at around 300 ^{0}C. The gradual decrease of weight reveals the possibility of getting higher porosity or larger surface area of a newly synthesized cobalt complex.

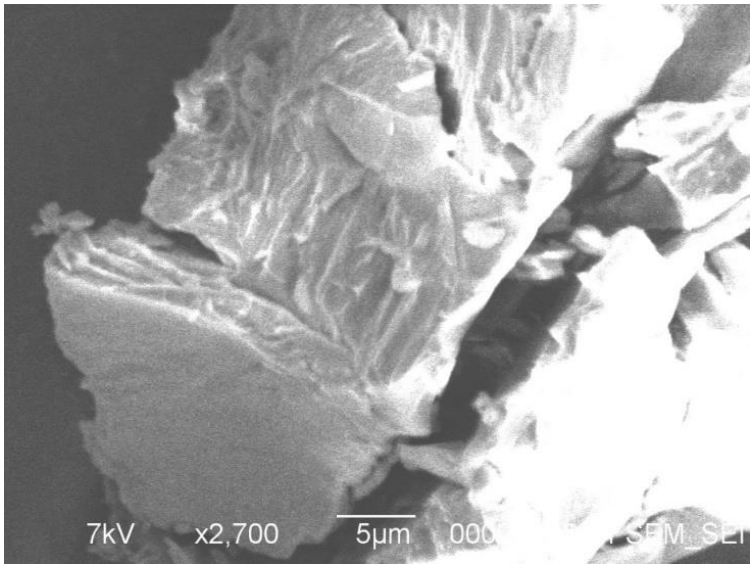

Fig. 41: Secondary Electron Images (SEI) data from SEM analysis of **[Co (H$_3$BTCA)$_3$ (DMF)$_2$]$_n$**

From the SEM image, grain orientation is visible, and a layered structure is found.

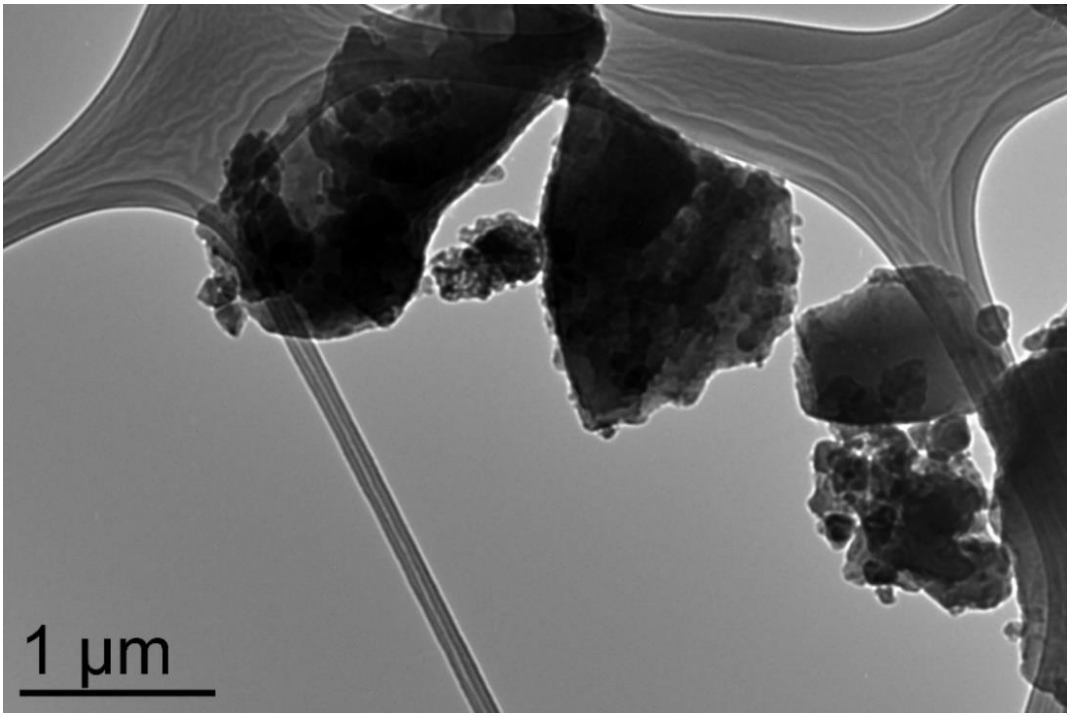

Fig. 42: TEM image of **[Co (H$_3$BTCA)$_3$ (DMF)$_2$]$_n$ [H]** in microscale.

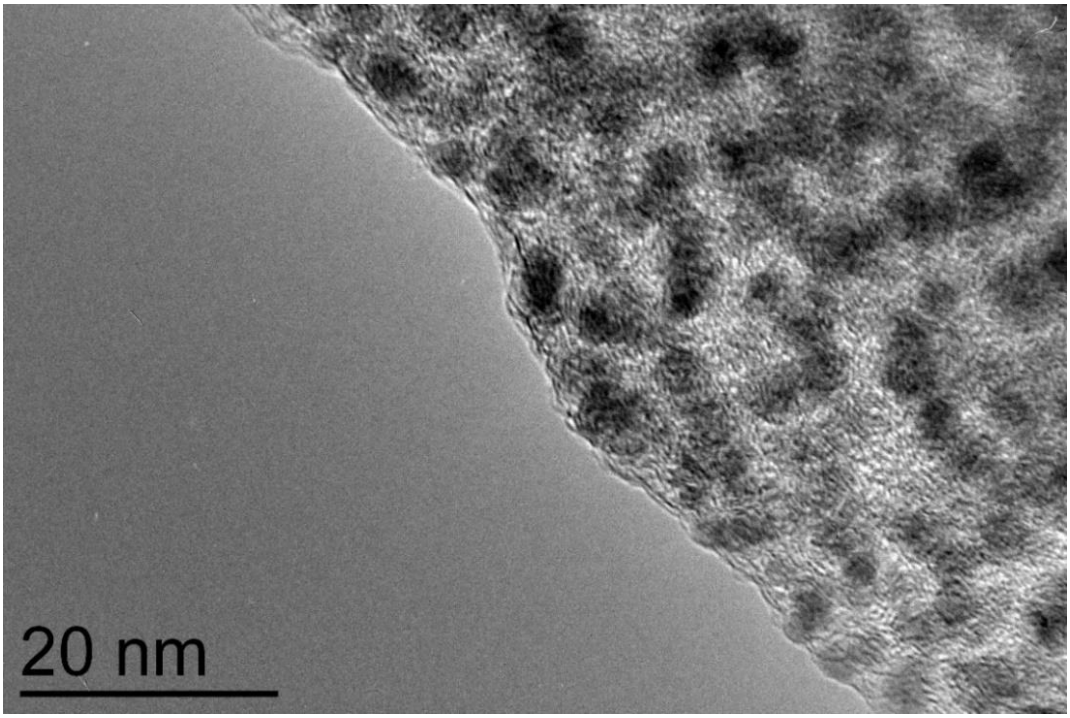

Fig. 43: High-Resolution Transmission Electron Microscopy (HRTEM) image of **[H]**

From figure 42, we found the agglomeration of particles and spherical particles growing in the image. Figure 43 shows the atomic resolution of the compound, where the stacking of atoms is seen, even though atomic size could not be established from the HRTEM image.

[I] Two-dimensional Metal-organic Framework [Co $(H_3BTCA)_3$ $(DMF)_3]_n$

Under solvothermal synthesis condition, 0.5 millimoles anhydrous $CoCl_2$ (0.0649g) and 0.5 millimoles 1,3,5- benzenetricarboxylic acid (0.105g) along with 0.5 millimoles imidazole (0.034g) were mixed with 6 mL DMF in the Teflon autoclave. After mixing, the solution was heated at 150 ^{0}C for 24 hours. The products were cooled at 80 ^{0}C for 24 hours, and lastly, standing at ambient temperature for 24 hours. A pink-colored crystal and powder samples were produced, and characterization analysis was performed.

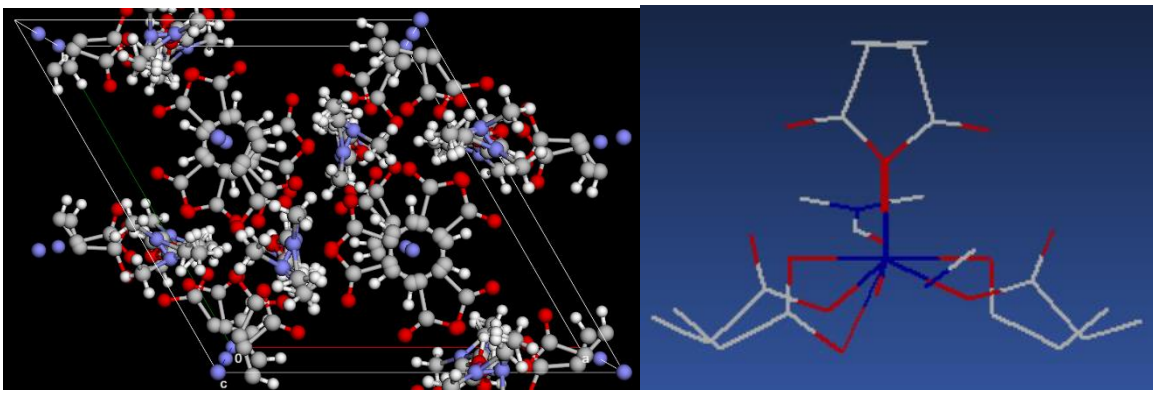

Fig. 44: Single crystal XRD analysis of **[Co $(H_3BTCA)_3$ $(DMF)_3]_n$ a.)** Unit cell information **b.)** Pipe model.

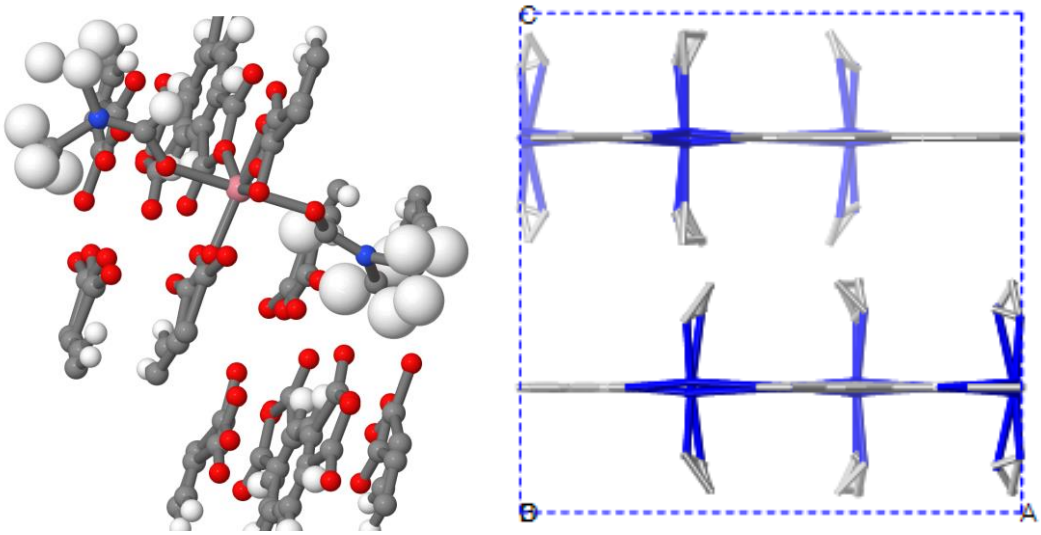

Fig. 45: a. Atomic arrangement of **[I]** in ball and stick view b. planner view (Pipe model)

Table 7: Crystal information of **[Co (H$_3$BTCA)$_3$ (DMF)$_3$]$_n$**

Chemical formula	$C_{33}H_0Co_3N_6O_{24}$
M_r	1041.18
Crystal system, space group	Hexagonal, $P6_3/m$
Temperature (K)	280
a, c (Å)	16.6093 (7), 14.2889 (8)
V (Å^3)	3413.8 (3)
Z	2
Radiation type	Mo $K\alpha$
μ (mm^{-1})	0.78
No. of measured, independent and observed [$I > 2\sigma(I)$] reflections	31557, 2478, 2070
R_{int}	0.116
$(\sin \theta/\lambda)_{max}$ (Å^{-1})	0.630
No. of reflections	2478
No. of parameters	288
No. of restraints	819
H-atom treatment	H-atom parameters constrained
D_x	1.013 Mg m^{-3}
$(\Delta/\sigma)_{max}$	0.941
$\Delta\rho_{max}$, $\Delta\rho_{min}$ (e Å^{-3})	2.31, −5.08

Symmetry codes: (i) −y+1, x−y+1, z; (ii) −x+y, −x+1, −z+1/2; (iii) −x+y−1, −x, −z+1/2; (iv) −y, x−y, z; (v) −y, x−y+1, z; (vi) −x+y, −x, −z+1/2.

The material is not perfectly crystalline with large non-Bragg intensity between diffraction spots. It is a trimer of cobalt-coordinated with the oxygen of four molecules of 1,3,5- benzenetricarboxylic acid and three molecules of DMF. The complex structure provides chains in all directions which creates a two-dimensional layered coordinated complex.

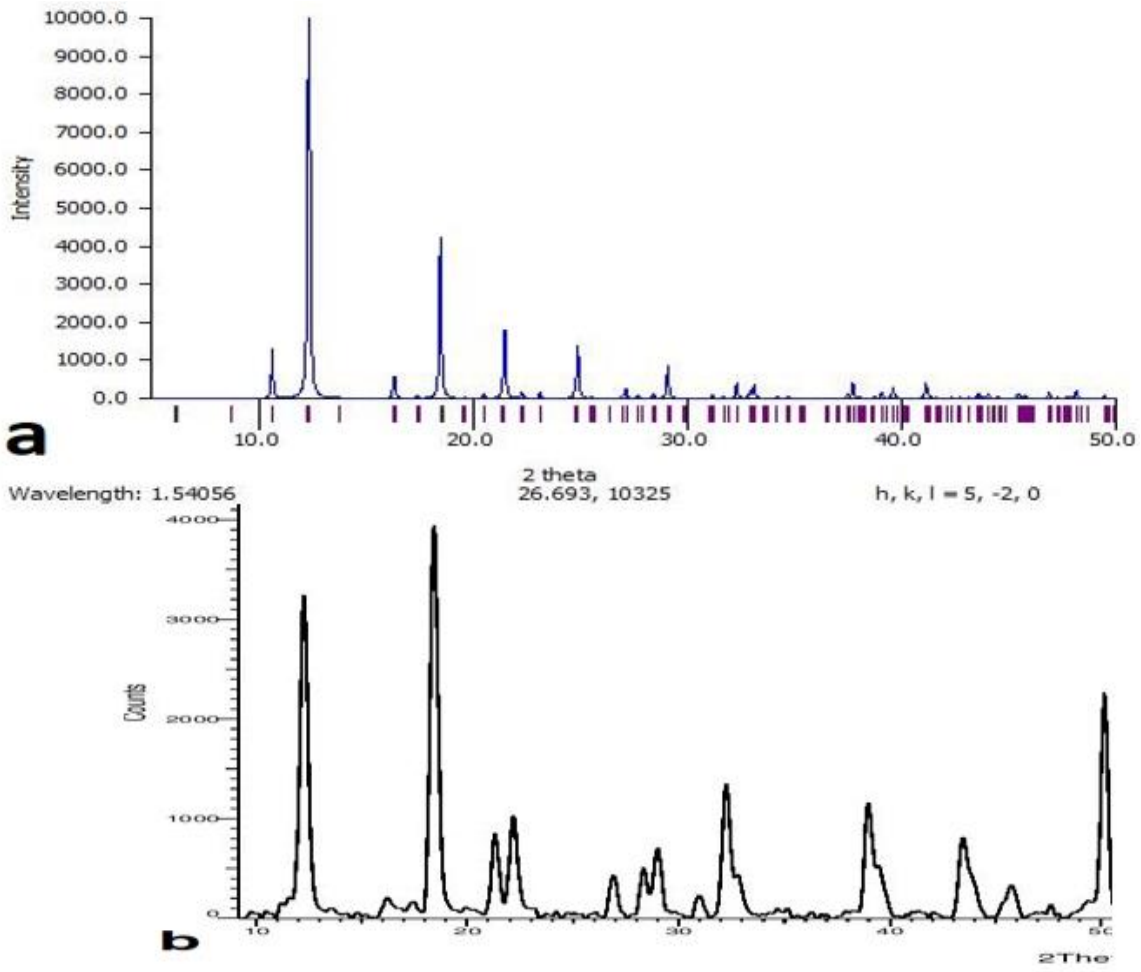

Fig. 46: **a**. The simulated PXRD pattern (produced from SXRD data) **b.** experimental PXRD pattern of **$[Co(H_3BTCA)_3(DMF)_3]_n$**

From figure 46, the majority of the experimented PXRD peaks matched with the simulated PXRD peaks and the degree of crystallinity was better for this compound.

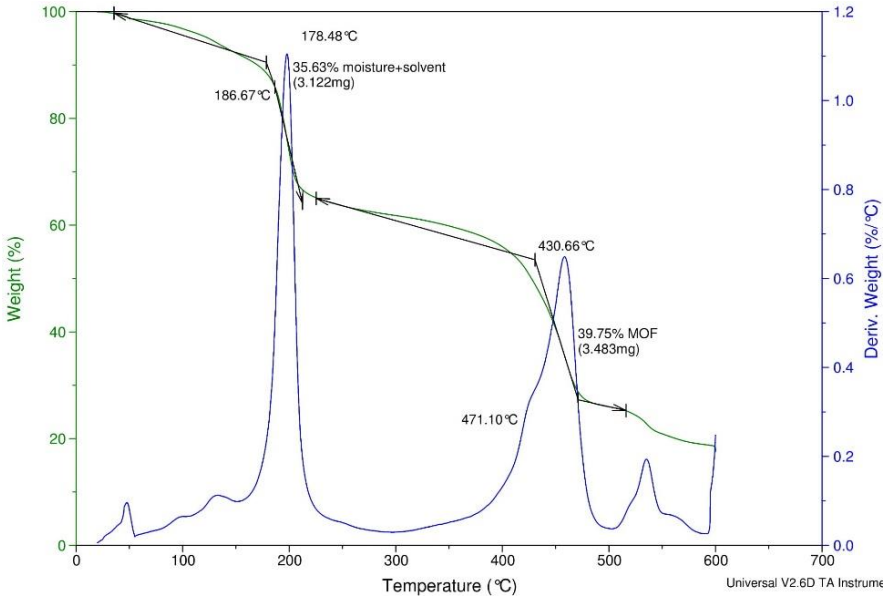

Fig. 47: TGA analysis of **[Co (H$_3$BTCA)$_3$ (DMF)$_3$]$_n$**

Figure 47 shows the thermal decomposition of our sample. Because of the lower reaction time, a higher percentage of the compound is solvent. The moisture and solvent component is reflected in the ~35% decomposition up to 200 ^{0}C. This sample's organizational thermal stability is good, which shown in the TGA analysis.

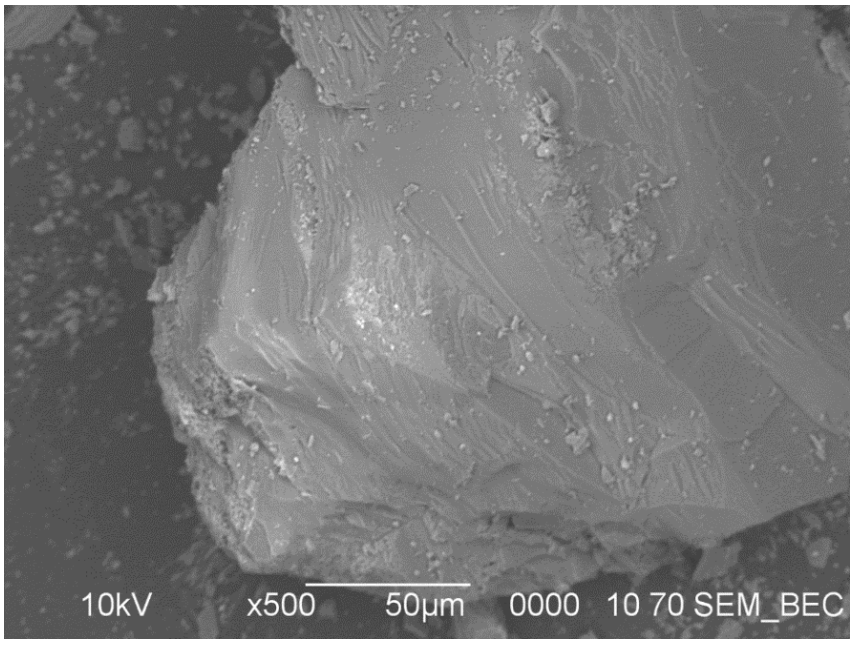

Fig. 48: Backscattered Electron Image (BEC) of **[Co (H$_3$BTCA)$_3$ (DMF)$_3$]$_n$**

Figure 48 shows the structural configuration of the compound.

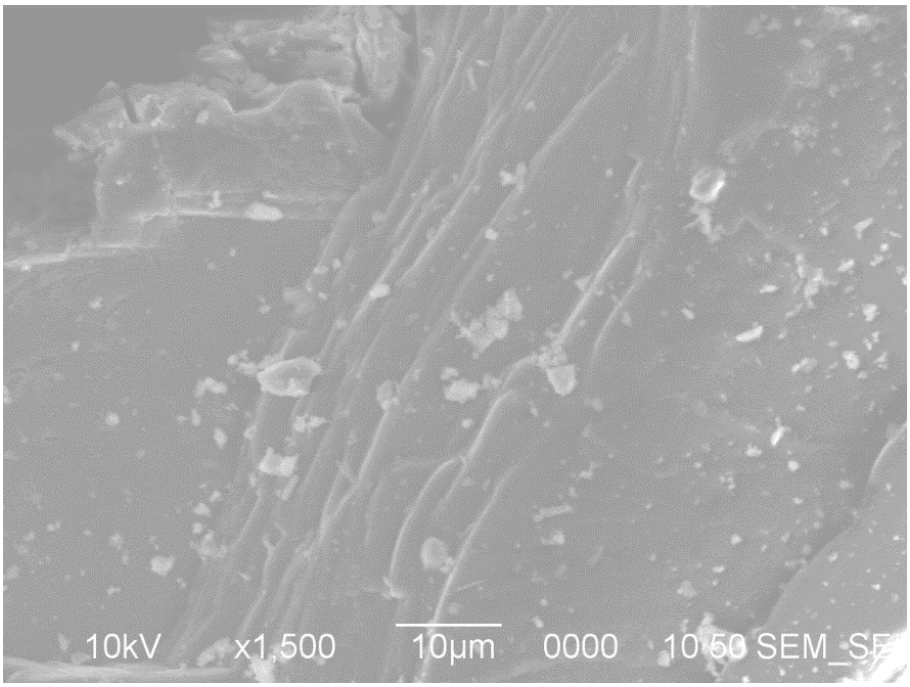

Fig. 49: Secondary Electron Image of **$[Co(H_3BTCA)_3(DMF)_3]_n$** at x1500 magnification

Figure 49 reveals the layered structure of the synthesized product.

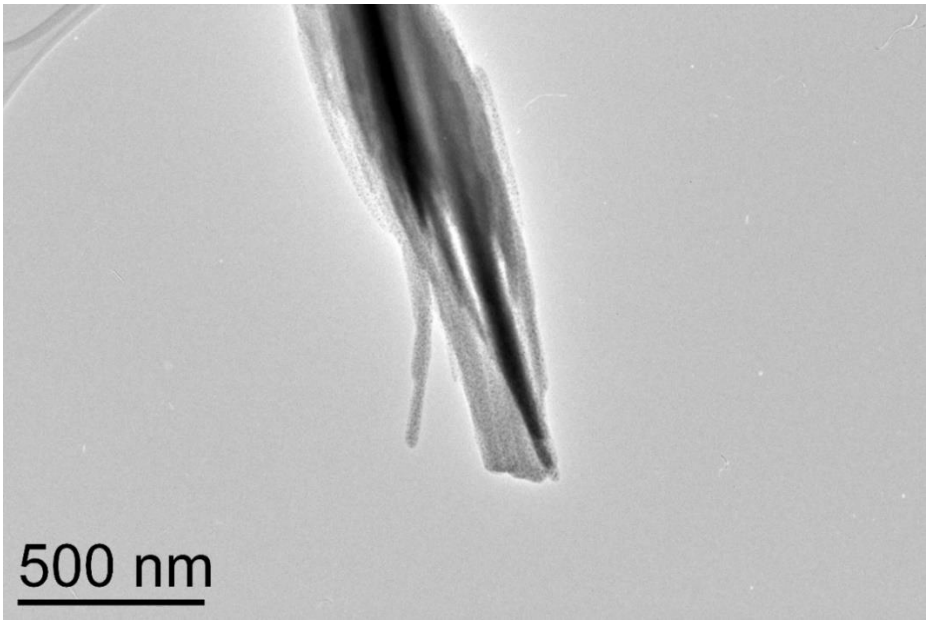

Fig. 50: TEM image of **$[Co(H_3BTCA)_3(DMF)_3]_n$** which shows a rod or tubular like structure.

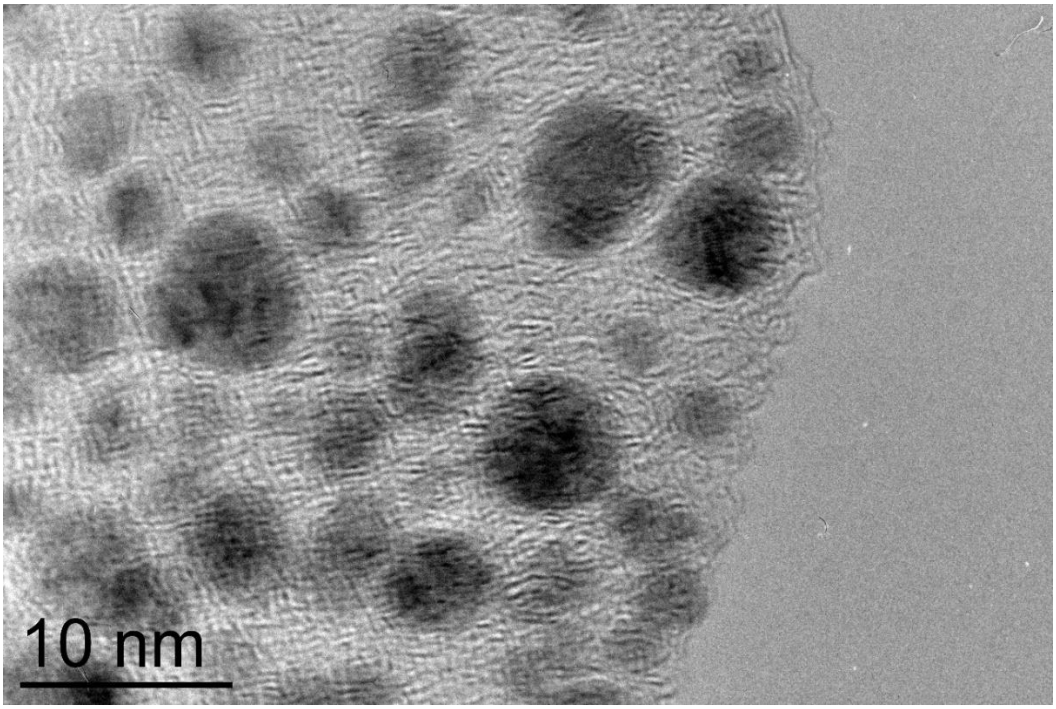

Fig. 51: High-Resolution Transmission Electron Microscopy (HRTEM) image of **[I]**

From TEM nanostructure of the sample (fig. 50 and 51), it can be easily understood about the shape of the particle. Figure 51 represents the HRTEM image of a different portion of the particle. Atomic resolution is clearly observed in the image. Atomic spheres are stacked together (like dark and bright fringes), and orientation of atoms are also identified from the images. The image shows the typical contrast differences from negative to positive contrast. It was found that neighboring atomic spheres show different contrast. This contrast difference may be due to the different chemical composition of the different atomic spheres. [30]

[J] Two-dimensional Metal-organic Framework [Co $(H_3BTCA)_4$ $(DMF)_3]_n$

Under solvothermal synthesis condition, 0.1296g anhydrous $CoCl_2$ (1 millimoles) and 0.63g 1,3,5- benzenetricarboxylic acid (2 millimoles) was mixed with six mL 1:1=DMF:

methanol in the Teflon autoclave. After mixing, the solution was heated at 150 ^{0}C for 24 hours. The products were cooled at 80 ^{0}C for 24 hours, and lastly, held at room temperature for 24 hours. A purple-colored crystal and powder samples were produced, and a suitable characterization analysis was performed.

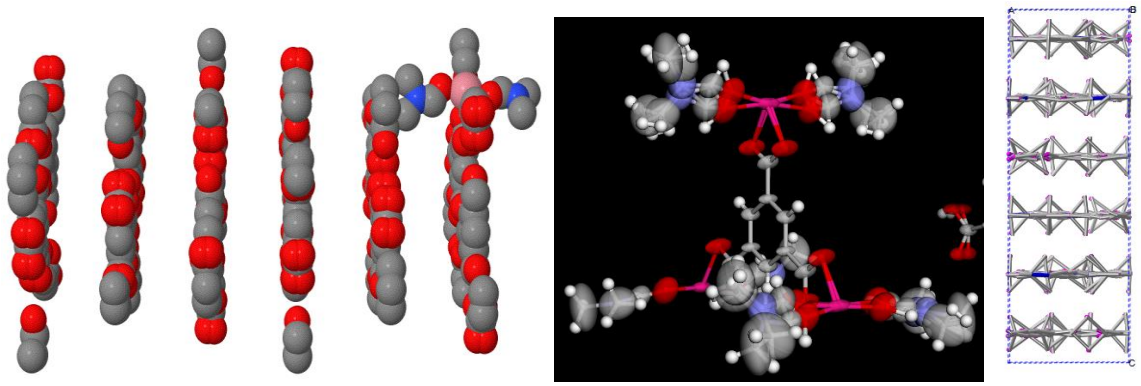

Fig. 52: SXRD data of **[Co (H$_3$BTCA)$_4$ (DMF)$_3$]$_n$ a.** Space filing view b. Hirshfield molecular view c. layered structure front view (Pipe model)

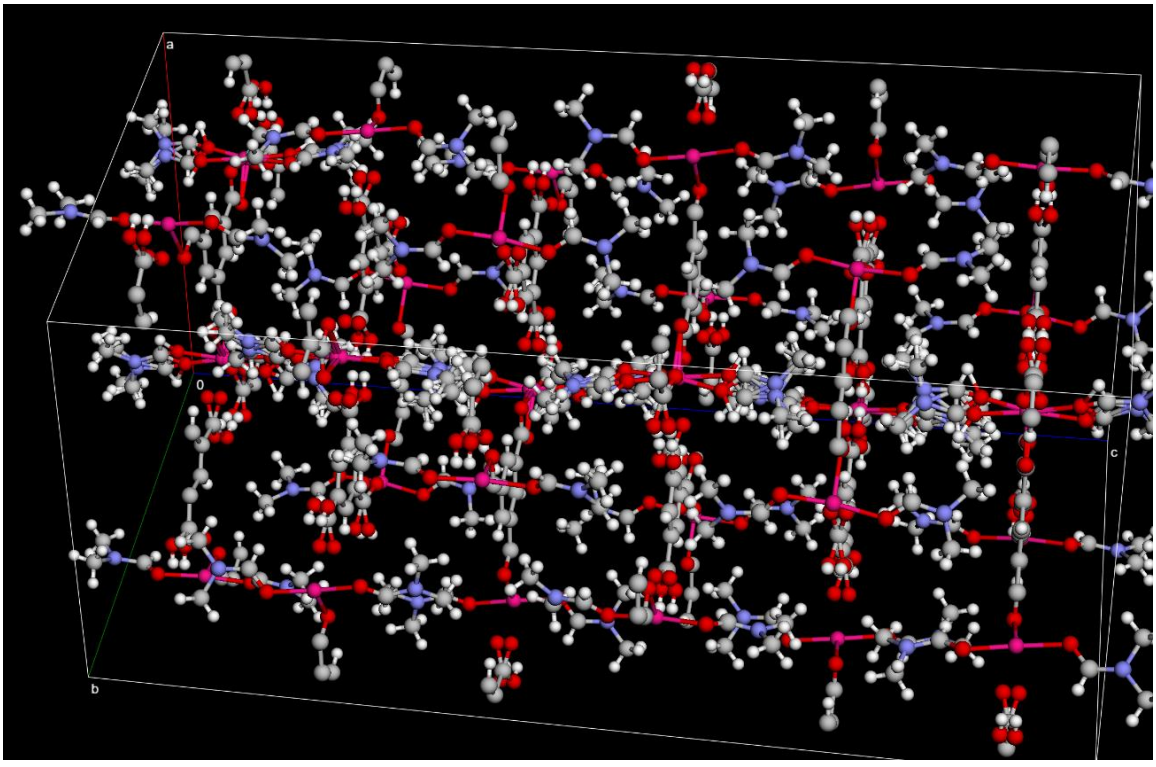

Fig. 53: Unit cell of **[Co (H$_3$BTCA)$_4$ (DMF)$_3$]$_n$**

Table 8: Crystal information of **[Co (H$_3$BTCA)$_4$ (DMF)$_3$]$_n$**

Chemical formula	$C_{45}H_{54}Co_3N_6O_{24}$
M_r	1239.73
Crystal system, space group	Trigonal, *R*3*c*:*H*
Temperature (K)	280
a, *c* (Å)	16.6415 (7), 42.844 (2)
V (Å^3)	10275.5 (10)
Z	6
Radiation type	Mo *K*α
μ (mm^{-1})	0.79
Crystal size (mm)	0.80 × 0.35 × 0.21
No. of measured, independent and observed [$I > 2\sigma(I)$] reflections	42600, 2847, 2555
R_{int}	0.054
$(\sin \theta/\lambda)_{max}$ (Å^{-1})	0.668
$R[F^2 > 2\sigma(F^2)]$, $wR(F^2)$, S	0.054, 0.149, 1.14
No. of reflections	2847
No. of parameters	174
No. of restraints	206

From the SXRD analysis, the crystal is twinned by merohedry through a 180-degree rotation in the (-1 1 0 lattice direction).

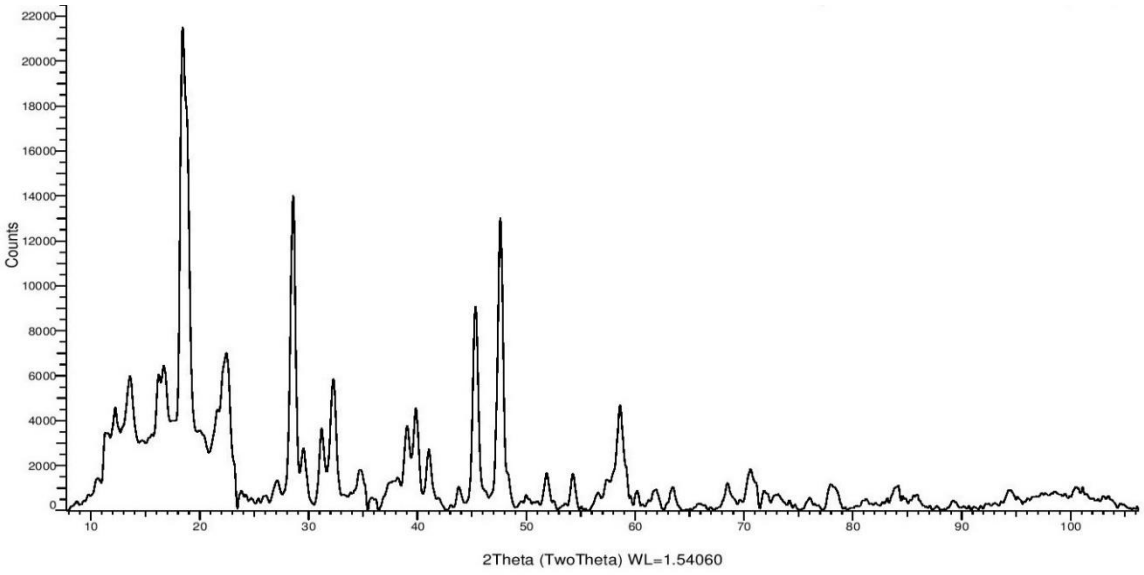

Fig. 54: PXRD data of **[Co (H$_3$BTCA)$_4$ (DMF)$_3$]$_n$**

Figure 54 represents the powder X-ray diffraction pattern of **[J] [Co ($H_3BTCA)_4$ $(DMF)_3]_n$**, which reveals a good amount of crystallinity compared to the previous sample.

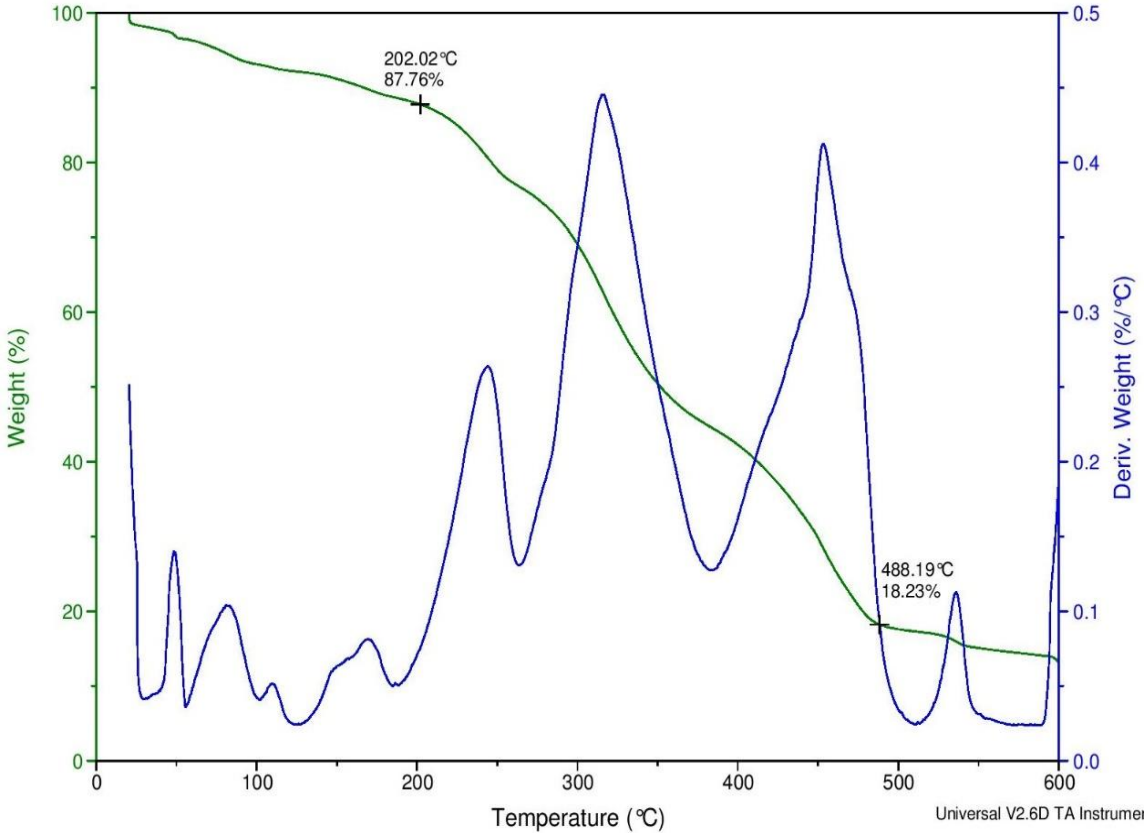

Fig. 55: TGA profile of **[Co ($H_3BTCA)_4$ $(DMF)_3]_n$**

Figure 55 provides the thermal decomposition profile of our sample. Solvent decomposition is reflected in the ~13% decomposition up to around 200 ^{0}C. Because of the gradual decomposition rate from the TGA profile, this sample's thermal stability is very good.

4.3 Other Characterization Techniques

a. Raman Spectroscopy Analysis

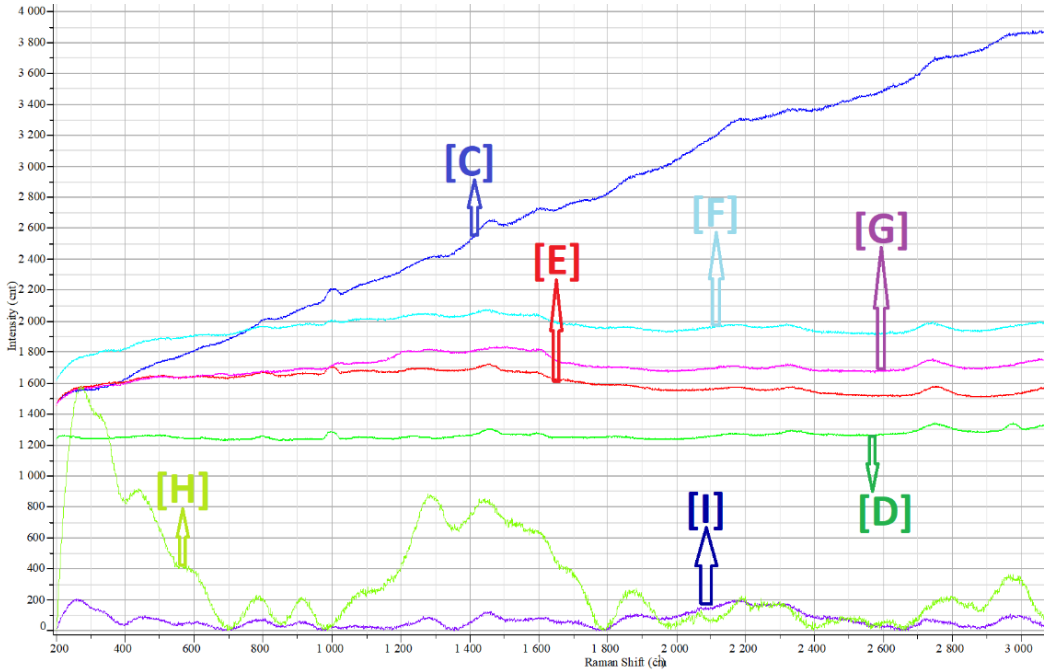

Fig. 56: Comparative Raman spectroscopy analysis of lab samples.

From the Raman spectroscopy analysis, we did not get enough information to study the physical and chemical properties of our produced compound.

b. Solid State Nuclear Magnetic Resonance (NMR) Analysis

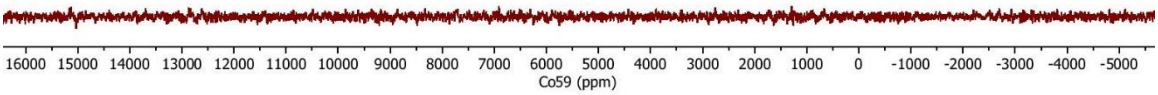

Fig. 57: Co59 solid-state NMR experiment of **[F] [Co (H$_3$BTCA)$_4$ (Imidazole)]$_n$**

(source: Chemistry Department, University of Akron)

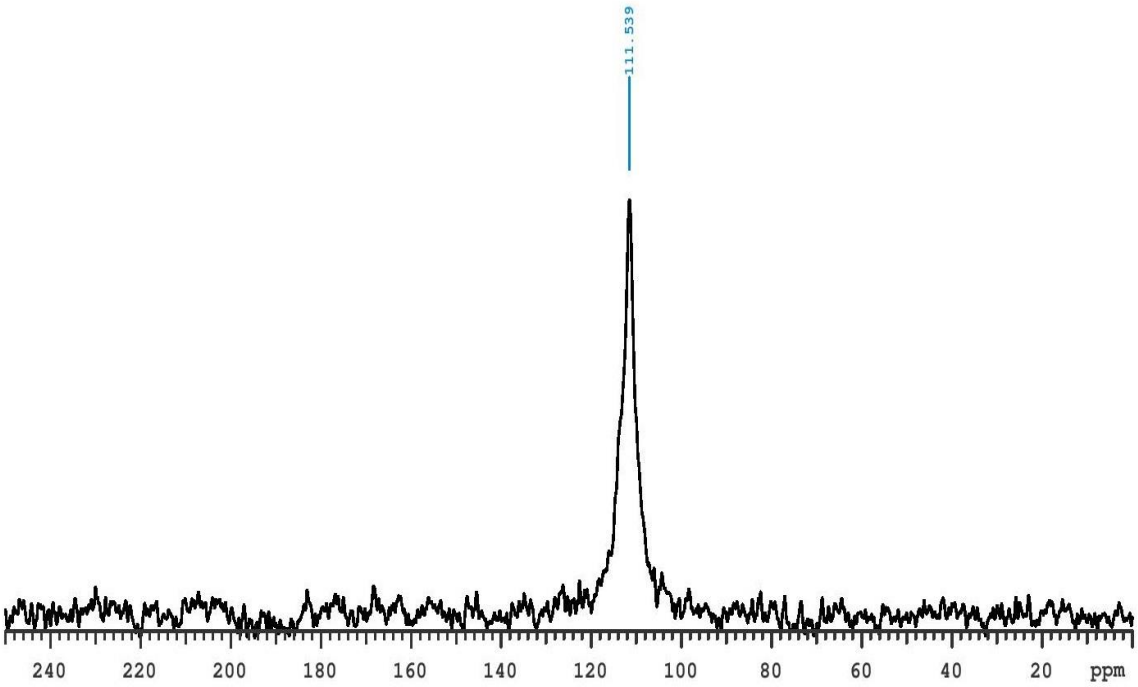

Fig. 58: C13 solid-state NMR experiment of **[F] [Co (H$_3$BTCA)$_4$ (Imidazole)]$_n$**
(source: Chemistry Department, University of Akron)

To establish the presence of anisotropic interactions between the molecules, we sent our samples to University of Akron for solid-state C13 and Co59 NMR spectroscopy. From fig 57, the lack of signal would confirm the presence of Co(II), which is the oxidation state of cobalt that does not appear in NMR may be because it is paramagnetic. From figure 58, The C13 spectra were visibly referenced to the methyl signal of hexamethylbenzene at 17.3 ppm, and the Co59 spectra were externally referenced to sodium cobaltinitrite at 7594 ppm which is inappropriate with our sample specification.

4.4 Comparison and Discussion

a. Powder XRD Analysis

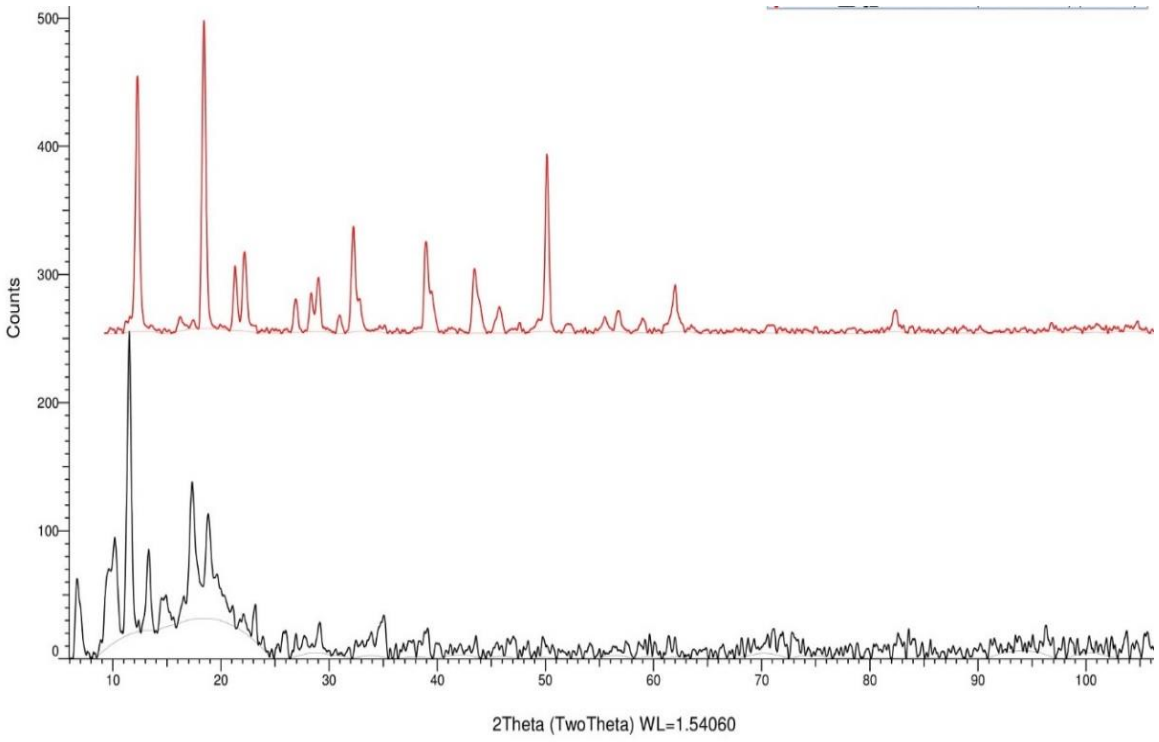

Fig. 59: Effect of Reaction Temperature; black spectra: [F] higher reaction time (150-120-90-60-RT; 24 hours cycle); red spectra: [I] (150-80-RT; 24 hours cycle)

Figure 59 reveals the powder XRD patterns of the produced compounds comparing the thermal condition and time, representing the existence of metallic cobalt in the materials and the degree of crystallinity. In both cases, reaction materials are the same. From the diagram, the development of sharper peaks appears as the reaction temperature increases, indicative of a rise in the cobalt particle's crystallinity and the number of peaks. Co particle size steadily increases with reaction temperature and reaction time. [16] Lower reaction time peaks show the lower phase crystal purity in the compound.

b. TGA Analysis

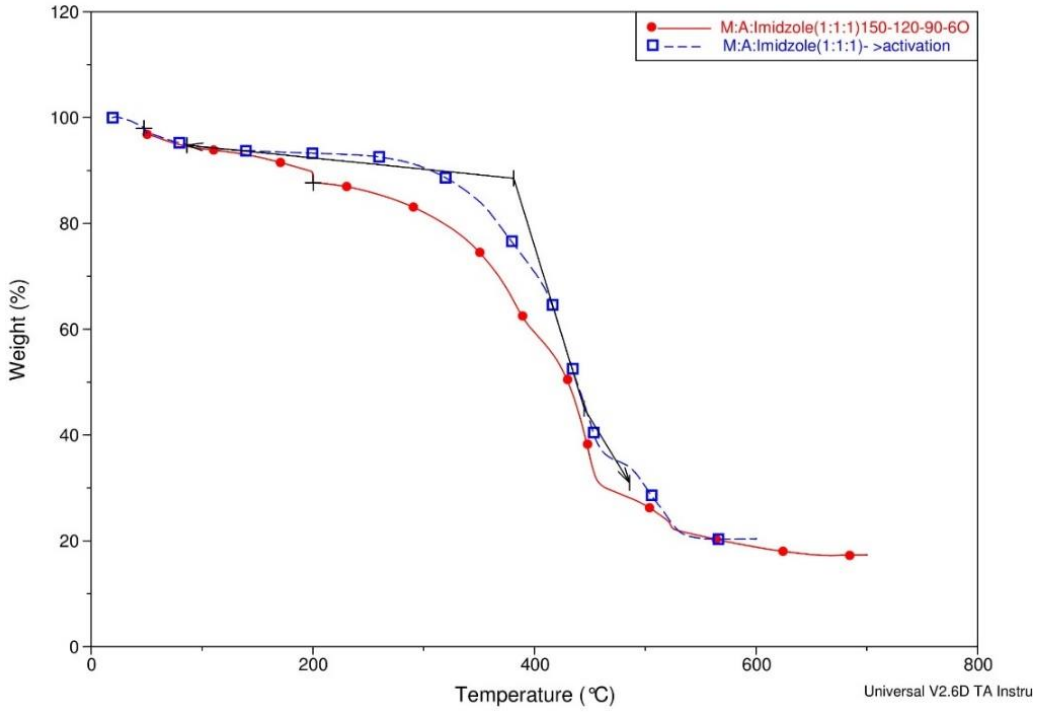

Fig. 60: Effect of Activation on TGA analysis of [F] **[Co (H$_3$BTCA)$_4$ (Imidazole)]$_n$**

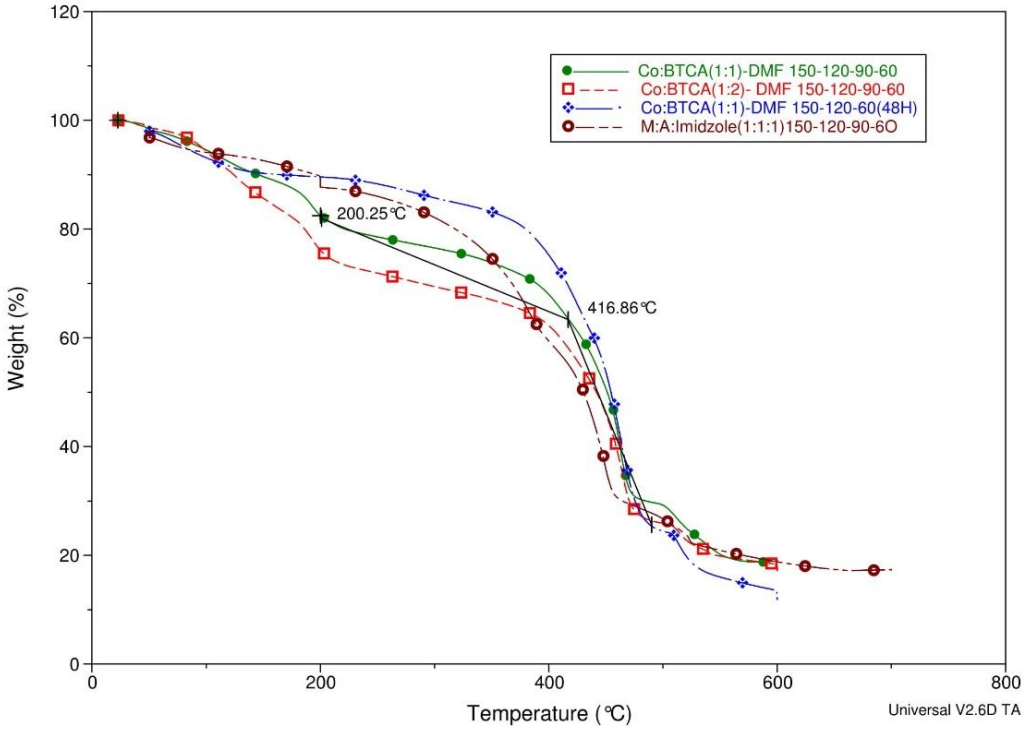

Fig. 61: Effect of reaction time and composition on TGA analysis

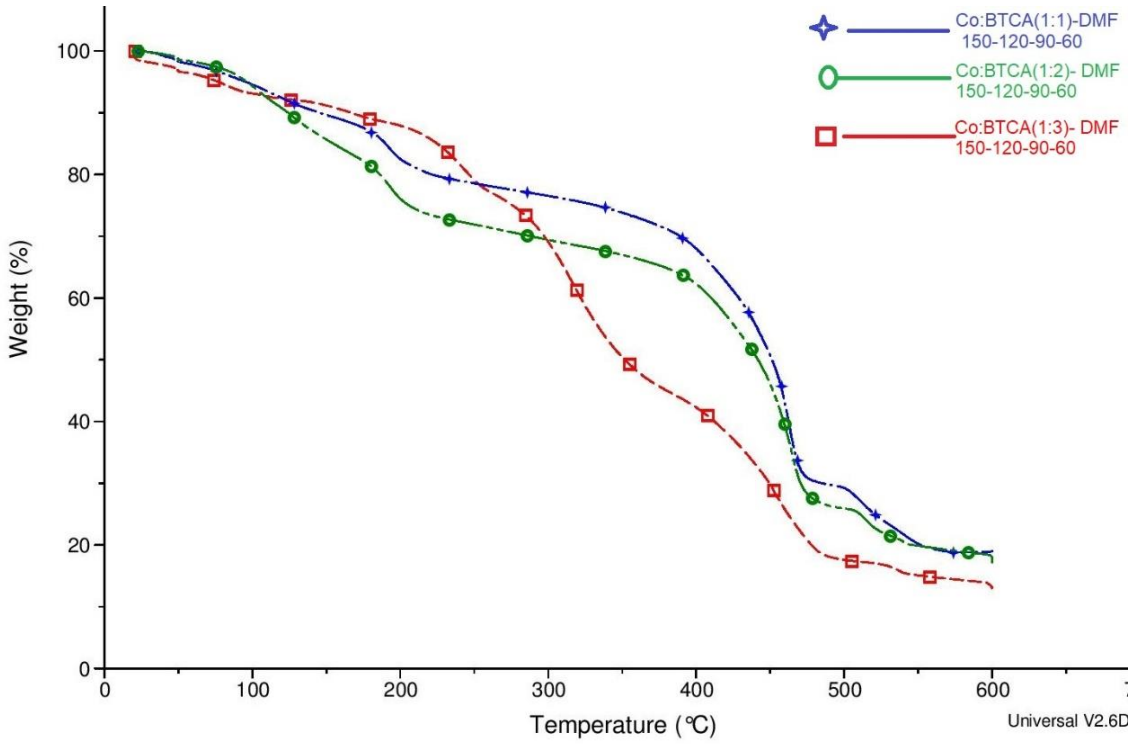

Fig. 62: Effect of composition on TGA analysis

Figure 60 compares the thermal stability of Co-MOF [F] before activation and after activation, and from the graph, after activation, the compound becomes more thermally stable. Figure 61 compares the weight loss TGA curves of cobalt complexes according to the reaction time and concentration. It reveals that there is an instantaneous drop in weight loss when samples are exposed to approximately 200 °C, which is similar to the exclusion of the solvent and moisture content from the compounds. Figure 62 compares the TGA profile according to the various reaction composition. Increasing linker composition by doubling the ratio of metal salt to linker increases thermal stability and more gradual thermal decomposition occurs in the thermal profile, but if we increase the composition of organic linker (1:3), then thermal stability increases with fluctuation and presents a more dramatic weight drop in the thermal profile. [31]

c. TEM Analysis

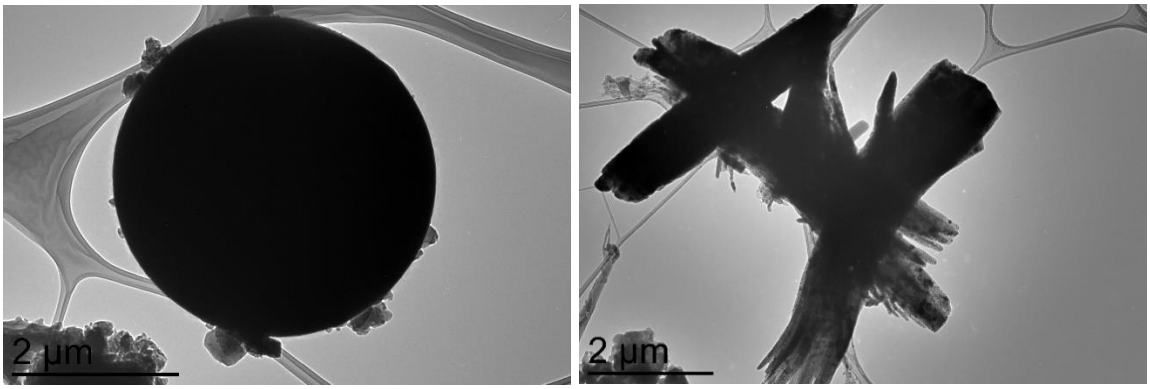

Fig. 63: TEM image of a.) [H] [CoCl2: BTCA: 4,4'- trimethylene-dipyridine (1: 2:2)-DMF 150-120-90-60] b.) [I] CoCl2: BTCA: imidazole (1: 1:1)-DMF: 150-80

Figure 63 shows the difference between two different cobalt complexes via TEM image. Both images at 2 micrometers reveal a particle growth distribution with different morphologies of two different cobalt complexes, thus comparing different reactants and reaction time. Figure 63 a) reveals the growth distribution of micro-crystals of the compound as a sphere and figure 63 b) shows the growth distribution as rod-like.[32] Sphere type of particle growth reveals the structure as zero or one dimensional and rod type of growth revels the structure as two or three-dimensional compound.

Chapter 5: Conclusion

In this research project, different cobalt metal salts, and solvent and linker combinations were investigated with the solvothermal synthesis approach. After the synthesis, we found two three-dimensional and two two-dimensional metal-organic framework compounds as well as two one-dimensional cobalt-coordinated novel complexes. We also found one one-dimensional (similar as reported structure) and two zero-dimensional complexes. Based on the SXRD, SEM and TEM analysis, four MOF compounds were found which are a subclass of coordination complexes. Temperature and reagent concentration effects were investigated with characterization techniques such as SXRD, PXRD, TGA, SEM, and EDS analysis. The concentration of organic linkers and third-party linkers such as nitrogen-based linker addition improved the structural properties of our cobalt complexes. The scope of different applications of cobalt MOFs and cobalt complexes was investigated with suitable characterization. More characterization and analysis can be further investigated to find out the scope of different application and property enhancement.

References:

(1) Furukawa, H.; Cordova, K. E.; O'Keeffe, M.; Yaghi, O. M. The Chemistry and Applications of Metal-Organic Frameworks. *Science* **2013**, *341* (6149), 1230444.

(2) Seo, J. S.; Whang, D.; Lee, H.; Jun, S. I.; Oh, J.; Jeon, Y. J.; Kim, K. A Homochiral Metal–Organic Porous Material for Enantioselective Separation and Catalysis. *Nature* **2000**, *404* (6781), 982–986.

(3) Rowsell, J. L. C.; Yaghi, O. M. Metal–Organic Frameworks: A New Class of Porous Materials. *Microporous Mesoporous Mater.* **2004**, *73* (1–2), 3–14.

(4) Mueller, U.; Schubert, M.; Teich, F.; Puetter, H.; Schierle-Arndt, K.; Pastré, J. Metal–Organic Frameworks—Prospective Industrial Applications. *J Mater Chem* **2006**, *16* (7), 626–636.

(5) Catalytic Applications of Metal-Organic Frameworks | IntechOpen /books/advanced-catalytic-materials-photocatalysis-and-other-current-trends/catalytic-applications-of-metal-organic-frameworks (accessed May 9, 2018).

(6) Li, H.; Eddaoudi, M.; O'Keeffe, M.; Yaghi, O. M. Design and Synthesis of an Exceptionally Stable and Highly Porous Metal-Organic Framework. **1999**, *402*, 4.

(7) Czaja, A. U.; Trukhan, N.; Müller, U. Industrial Applications of Metal–Organic Frameworks. *Chem. Soc. Rev.* **2009**, *38* (5), 1284.

(8) Grant Glover, T.; Peterson, G. W.; Schindler, B. J.; Britt, D.; Yaghi, O. MOF-74 Building Unit Has a Direct Impact on Toxic Gas Adsorption. *Chem. Eng. Sci.* **2011**, *66* (2), 163–170.

(9) Liu, J.; Thallapally, P. K.; McGrail, B. P.; Brown, D. R.; Liu, J. Progress in Adsorption-Based CO_2 Capture by Metal–Organic Frameworks. *Chem Soc Rev* **2012**, *41* (6), 2308–2322.

(10) Rowsell, J. L. C.; Yaghi, O. M. Strategies for Hydrogen Storage in Metal–Organic Frameworks. *Angew. Chem. Int. Ed.* **2005**, *44* (30), 4670–4679.

(11) Herm, Z. R.; Swisher, J. A.; Smit, B.; Krishna, R.; Long, J. R. Metal−Organic Frameworks as Adsorbents for Hydrogen Purification and Precombustion Carbon Dioxide Capture. *J. Am. Chem. Soc.* **2011**, *133* (15), 5664–5667.

(12) Barrett, S. The European Hydrogen and Fuel Cell Strategic Research Agenda and Deployment Strategy. *Fuel Cells Bull.* **2005**, *2005* (5), 12–19.

(13) Masoomi, M. Y.; Bagheri, M.; Morsali, A. Application of Two Cobalt-Based Metal–Organic Frameworks as Oxidative Desulfurization Catalysts. *Inorg. Chem.* **2015**, *54* (23), 11269–11275.

(14) You, B.; Jiang, N.; Sheng, M.; Gul, S.; Yano, J.; Sun, Y. High-Performance Overall Water Splitting Electrocatalysts Derived from Cobalt-Based Metal–Organic Frameworks. *Chem. Mater.* **2015**, *27* (22), 7636–7642.

(15) Liu, X.; Shi, C.; Zhai, C.; Cheng, M.; Liu, Q.; Wang, G. Cobalt-Based Layered Metal–Organic Framework as an Ultrahigh Capacity Supercapacitor Electrode Material. *ACS Appl. Mater. Interfaces* **2016**, *8* (7), 4585–4591.

(16) Chaikittisilp, W.; Torad, N. L.; Li, C.; Imura, M.; Suzuki, N.; Ishihara, S.; Ariga, K.; Yamauchi, Y. Synthesis of Nanoporous Carbon–Cobalt-Oxide Hybrid Electrocatalysts by Thermal Conversion of Metal–Organic Frameworks. *Chem. – Eur. J.* **2014**, *20* (15), 4217–4221.

(17) Li, W.-J.; Gao, S.-Y.; Liu, T.-F.; Han, L.-W.; Lin, Z.-J.; Cao, R. *In Situ* Growth of Metal–Organic Framework Thin Films with Gas Sensing and Molecule Storage Properties. *Langmuir* **2013**, *29* (27), 8657–8664.

(18) Sun, Y.; Zhou, H.-C. Recent Progress in the Synthesis of Metal–Organic Frameworks. *Sci. Technol. Adv. Mater.* **2015**, *16* (5), 054202.

(19) Mondloch, J. E.; Karagiaridi, O.; Farha, O. K.; Hupp, J. T. Activation of Metal–Organic Framework Materials. *CrystEngComm* **2013**, *15* (45), 9258.

(20) Lucas, K. D. Magnesium Sulfonyldibenzoates: Synthesis, Structure, Phase Transformation and Microscopic Studies, Youngstown State University, 2013.

(21) CIF publishing tools http://publcif.iucr.org/services/tools/ (accessed Jun 7, 2018).

(22) Bumbrah, G. S.; Sharma, R. M. Raman Spectroscopy – Basic Principle, Instrumentation and Selected Applications for the Characterization of Drugs of Abuse. *Egypt. J. Forensic Sci.* **2016**, *6* (3), 209–215.

(23) The Theory of Raman Spectroscopy - HORIBA http://www.horiba.com/us/en/scientific/products/raman-spectroscopy/raman-academy/raman-tutorial/the-theory-of-raman-spectroscopy/ (accessed May 21, 2018).

(24) JEOL USA JIB-4500 MultiBeam SEM-FIB https://www.jeolusa.com/PRODUCTS/Scanning-Electron-Microscopes-SEM/SEM-FIB/JIB-4500-MultiBeam (accessed Apr 4, 2018).

(25) Electron Microscopes | YSU http://www.ysu.edu/academics/science-technology-engineering-mathematics/facilities/chemistry-facilities/electron-microscopes (accessed Apr 4, 2018).

(26) JEM-2100 Electron Microscope | Products | JEOL Ltd. https://www.jeol.co.jp/en/products/detail/JEM-2100.html (accessed Apr 25, 2018).

(27) Experiment 2 - NMR Spectroscopy http://www.webassign.net/sample/ncsumeorgchem2/lab_2/manual.html (accessed May 21, 2018).

(28) Dybtsev, D. N.; Yutkin, M. P.; Peresypkina, E. V.; Virovets, A. V.; Hasegawa, Y.; Nishihara, H.; Fedin, V. P. Synthesis, Structure, and Magnetic Properties of the Cobalt(II) 1,3,5-Benzenetricarboxylate Layered Coordination Polymer. *Russ. Chem. Bull.* **2007**, *56* (9), 1782–1786.

(29) Liu, S.-J.; Cao, C.; Yang, F.; Yu, M.-H.; Yao, S.-L.; Zheng, T.-F.; He, W.-W.; Zhao, H.-X.; Hu, T.-L.; Bu, X.-H. High Proton Conduction in Two Co^{II} and Mn^{II} Anionic Metal–Organic Frameworks Derived from 1,3,5-Benzenetricarboxylic Acid. *Cryst. Growth Des.* **2016**, *16* (12), 6776–6780.

(30) Jiang, W. H.; Atzmon, M. The Effect of Compression and Tension on Shear-Band Structure and Nanocrystallization in Amorphous Al90Fe5Gd5: A High-Resolution Transmission Electron Microscopy Study. *Acta Mater.* **2003**, *51* (14), 4095–4105.

(31) Pu, S.; Wang, J.; Li, L.; Zhang, Z.; Bao, Z.; Yang, Q.; Yang, Y.; Xing, H.; Ren, Q. Performance Comparison of Metal–Organic Framework Extrudates and Commercial Zeolite for Ethylene/Ethane Separation. *Ind. Eng. Chem. Res.* **2018**, *57* (5), 1645–1654.

(32) Synthesis, Characterization and Comparative Study of Copper and Zinc Metal Organic Frameworks. *Chem. Sci. Trans.* **2013**, *2* (4).

Appendix A

Single Crystal X-ray Diffraction data analysis (SXRD)

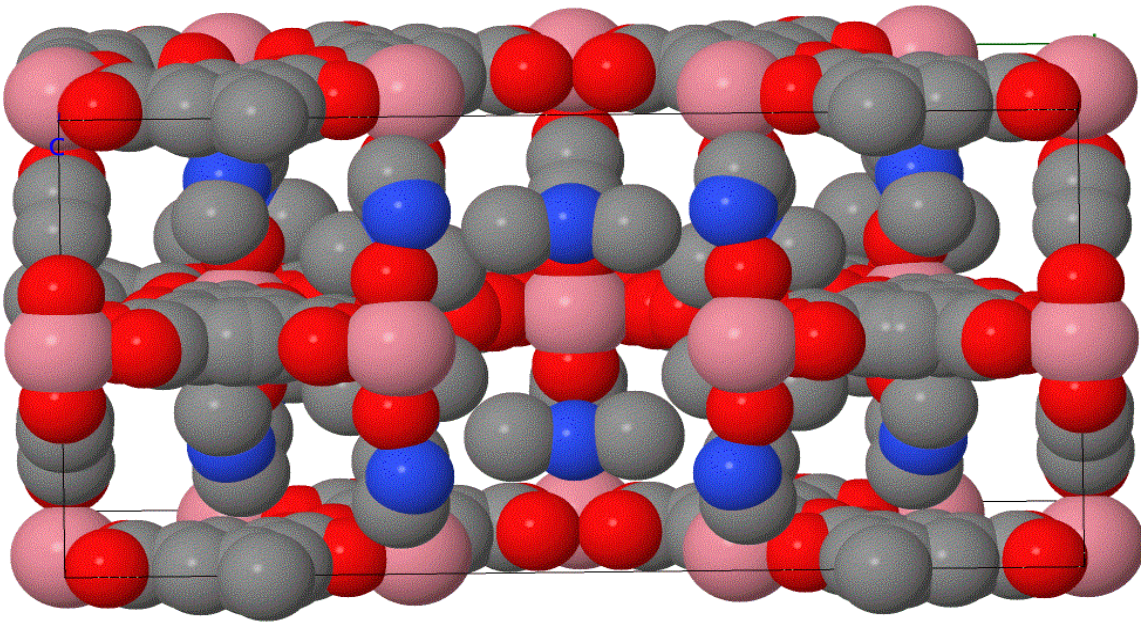

Fig. 64: SXRD (space filling view) data of **[C] [Co_6 ($H_3BTCA)_8$ $(DMF)_{18}(CO_2)_3]_n$. $2H_2O$]**

Table 9: Crystal information of Cobalt Complex [E] **[Co_3 (H_3BTCA) $(DMF)_6(CO_2)_3]_n$**

Chemical formula	$C_{33}H_0Co_3N_6O_{24}$
M_r	1041.18
Crystal system, space group	Hexagonal, $P6_3/m$
Temperature (K)	280
a, c (Å)	16.6513 (11), 14.2969 (11)
V (Å^3)	3433.0 (5)
Z	2
Radiation type	Mo $K\alpha$
μ (mm^{-1})	0.78
No. of measured, independent and observed [$I > 2\sigma(I)$] reflections	9186, 2326, 1820
R_{int}	0.059
$(\sin \theta/\lambda)_{max}$ (Å^{-1})	0.627
$R[F^2 > 2\sigma(F^2)]$, $wR(F^2)$, S	0.188, 0.589, 2.72
No. of reflections	2326
No. of parameters	288
No. of restraints	819
$(\Delta/\sigma)_{max}$	0.726
$\Delta\rho_{max}$, $\Delta\rho_{min}$ (e Å^{-3})	1.83, −1.89

Table 10 : Geometric parameters (Å, º) of **[F] [CoO_3 (H_3BTCA) $(DMF)_3]_n$**

O1—C1	1.249 (4)	C6—C5	1.93 (3)
O1—Co2	2.041 (3)	C6—C5^{iii}	1.93 (3)
C1—C2	1.510 (7)	C6—C5^{iv}	1.93 (3)
Co2—O2	2.059 (10)	C5—C5^{v}	1.17 (5)
Co2—Co2^{i}	2.9152 (15)	C7—C8	1.41 (4)
C2—C3	1.386 (3)	C7—C7^{vi}	2.00 (6)
C2—C3^{ii}	1.385 (3)	C7—C7^{vii}	2.00 (6)
C4—O2	1.19 (3)	C7—C7^{iv}	2.00 (6)
C4—C5	1.69 (3)	C7—C7^{iii}	2.00 (6)
C1—O1—Co2	126.4 (3)	C4—C5—C6	132.8 (17)
O1—C1—O1^{viii}	126.3 (5)	C8—C7—C7^{vi}	45.000 (2)
O1—C1—C2	116.8 (3)	C8—C7—C7^{vii}	45.000 (3)
O1^{viii}—C1—C2	116.8 (3)	C7^{vi}—C7—C7^{vii}	60.000 (5)
O1^{ix}—Co2—O1^{x}	88.36 (19)	C8—C7—C7^{iv}	45.000 (1)
O1^{ix}—Co2—O1^{v}	160.65 (19)	C7^{vi}—C7—C7^{iv}	60.000 (2)
O1^{x}—Co2—O1^{v}	88.41 (19)	C7^{vii}—C7—C7^{iv}	90.000 (1)
O1^{ix}—Co2—O1	88.41 (19)	C8—C7—C7^{iii}	45.000 (2)
O1^{x}—Co2—O1	160.65 (19)	C7^{vi}—C7—C7^{iii}	90.000 (2)
O1^{v}—Co2—O1	88.36 (19)	C7^{vii}—C7—C7^{iii}	60.000 (3)
O1^{ix}—Co2—O2	99.66 (10)	C7^{iv}—C7—C7^{iii}	60.000 (1)
O1^{x}—Co2—O2	99.66 (10)	C7—C8—C7^{vi}	90.0
O1^{v}—Co2—O2	99.68 (10)	C7—C8—C7^{xii}	180.0
O1—Co2—O2	99.68 (10)	C7^{vi}—C8—C7^{xii}	90.000 (3)
O1^{ix}—Co2—Co2^{i}	80.33 (10)	C7—C8—C7^{iv}	90.000 (12)
O1^{x}—Co2—Co2^{i}	80.33 (10)	C7^{vi}—C8—C7^{iv}	90.000 (3)
O1^{v}—Co2—Co2^{i}	80.33 (10)	C7^{xii}—C8—C7^{iv}	90.0
O1—Co2—Co2^{i}	80.32 (10)	C7—C8—C7^{vii}	90.0
O2—Co2—Co2^{i}	179.988 (1)	C7^{vi}—C8—C7^{vii}	90.000 (15)
C3—C2—C3^{ii}	120.2 (5)	C7^{xii}—C8—C7^{vii}	90.000 (12)
C3—C2—C1	119.9 (3)	C7^{iv}—C8—C7^{vii}	180.0
C3^{ii}—C2—C1	119.9 (3)	C7—C8—C7^{iii}	90.000 (7)
C2—C3—C2^{xi}	119.8 (5)	C7^{vi}—C8—C7^{iii}	180.0
O2—C4—C5	94 (2)	C7^{xii}—C8—C7^{iii}	90.0
C5—C6—C5^{iii}	103.0 (9)	C7^{iv}—C8—C7^{iii}	90.000 (12)
C5—C6—C5^{iv}	103.0 (9)	C7^{vii}—C8—C7^{iii}	90.000 (6)
C5^{iii}—C6—C5^{iv}	103.0 (9)	C4^{v}—O2—C4	136 (3)
C5^{v}—C5—C4	107.8 (12)	C4^{v}—O2—Co2	111.8 (15)
C5^{v}—C5—C6	119.4 (8)	C4—O2—Co2	111.8 (15)

Symmetry codes of [F]: (i) −*x*+1/2, −*y*+1, −*z*+1/2; (ii) −*z*+1/2, *x*, −*y*+1/2; (iii) *y*, *z*, *x*; (iv) *z*, *x*, *y*; (v) *x*, −*y*+1, *z*; (vi) −*y*+1, −*z*+1, −*x*+1; (vii) −*z*+1, −*x*+1, −*y*+1; (viii) −*z*+1/2, *y*, −*x*+1/2; (ix) *z*, *y*, *x*; (x) *z*, −*y*+1, *x*; (xi) *y*, −*z*+1/2, −*x*+1/2; (xii) −*x*+1, −*y*+1, −*z*+1

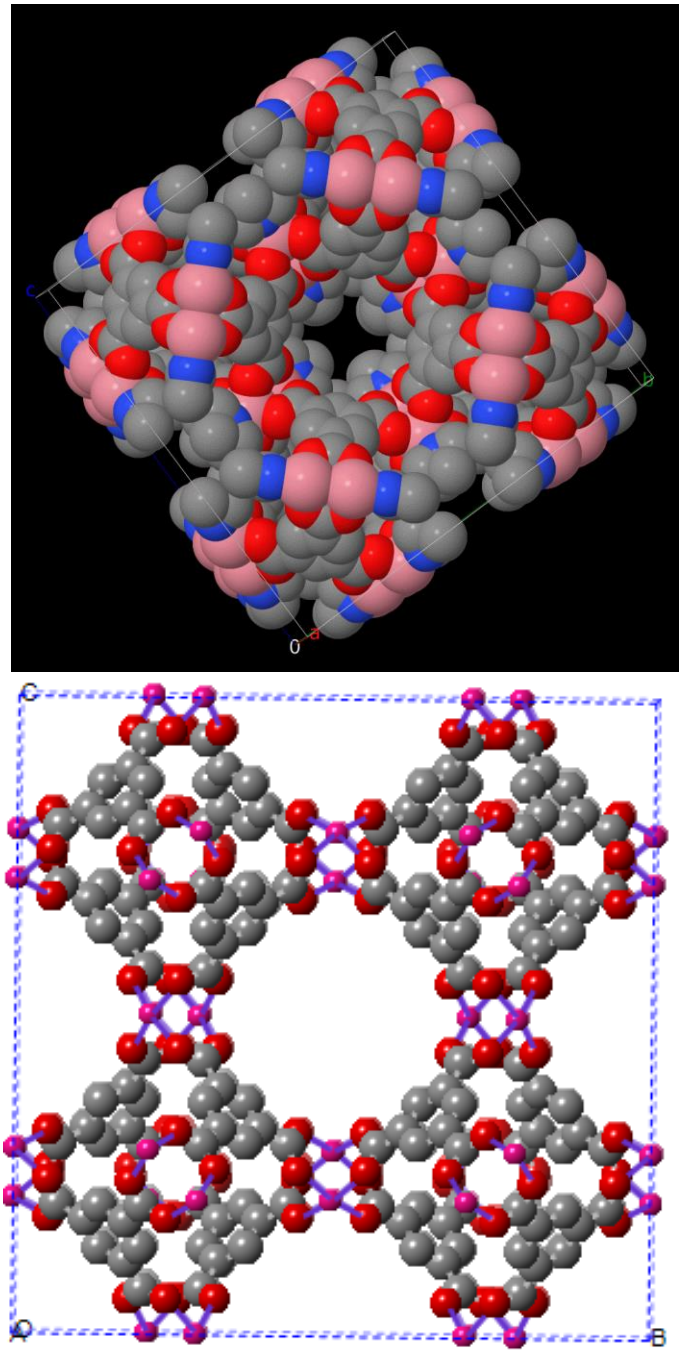

Fig. 65: a. Space-filling view of [G] **[Co (H3BTCA)3 (DMF)]n b.** ball stick model avowing solvent

Appendix B

Powder X-ray Diffraction data analysis (PXRD)

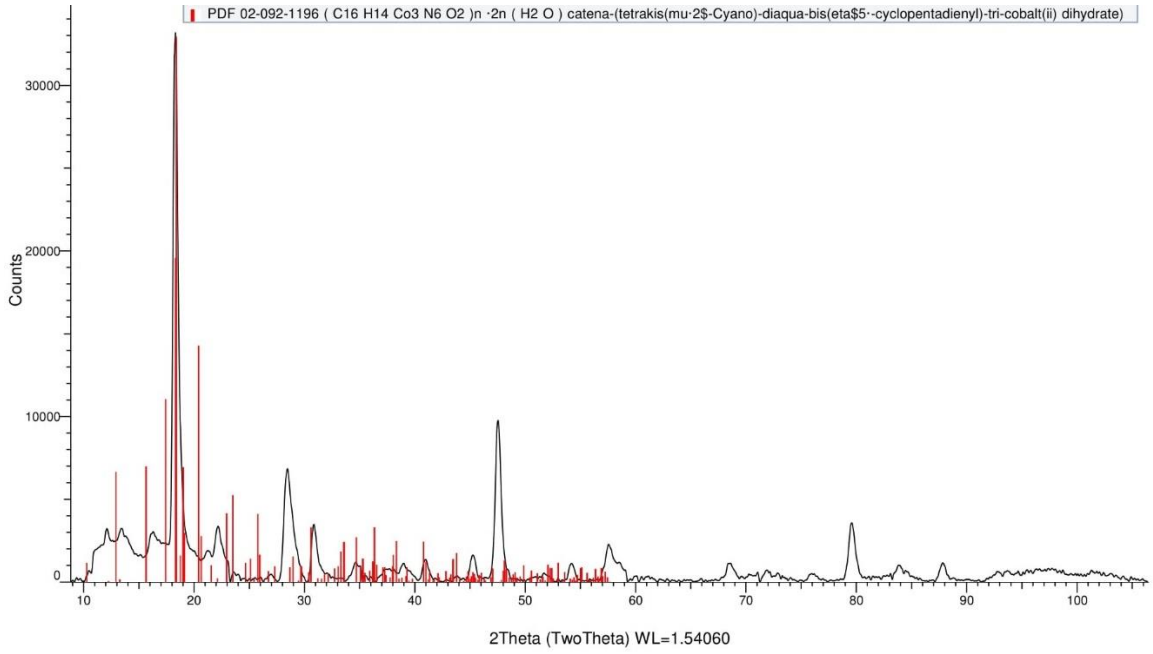

Fig. 66: PXRD data of **$[Co_3 (H_3BTCA) (DMF)_6(CO_2)_3]_n$** and matching data with reference to Cambridge structural database.

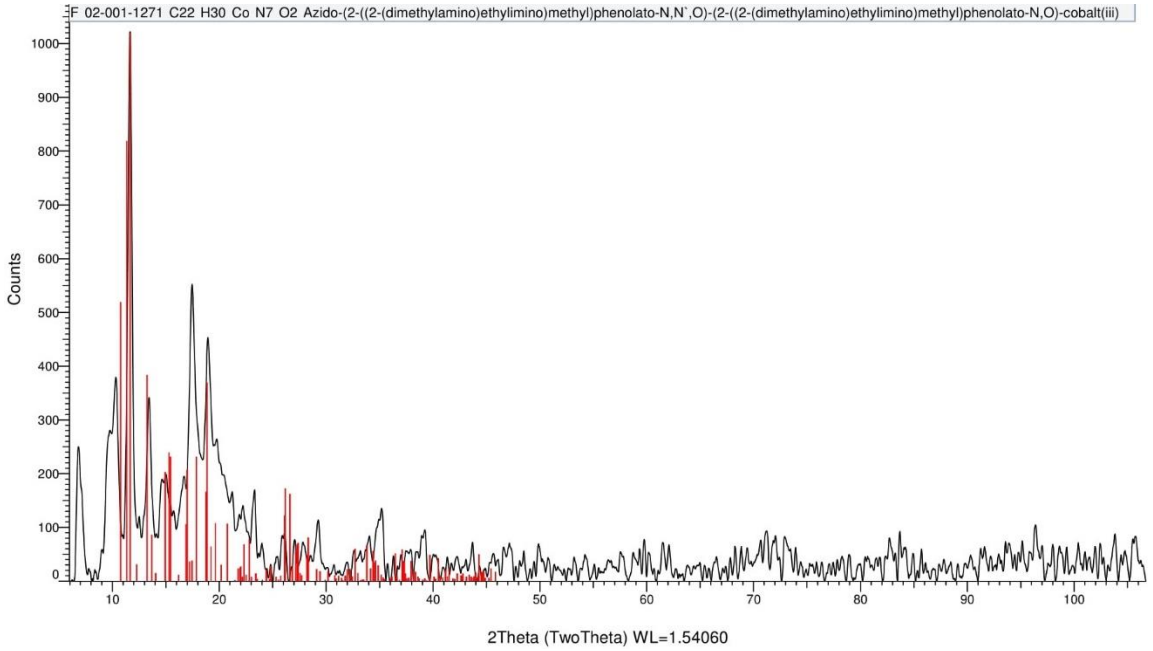

Fig. 67: Experimented (lab sample) PXRD pattern of [F] **$[Co (H_3BTCA)_4 (Imidazole)]_n$** (before activation)

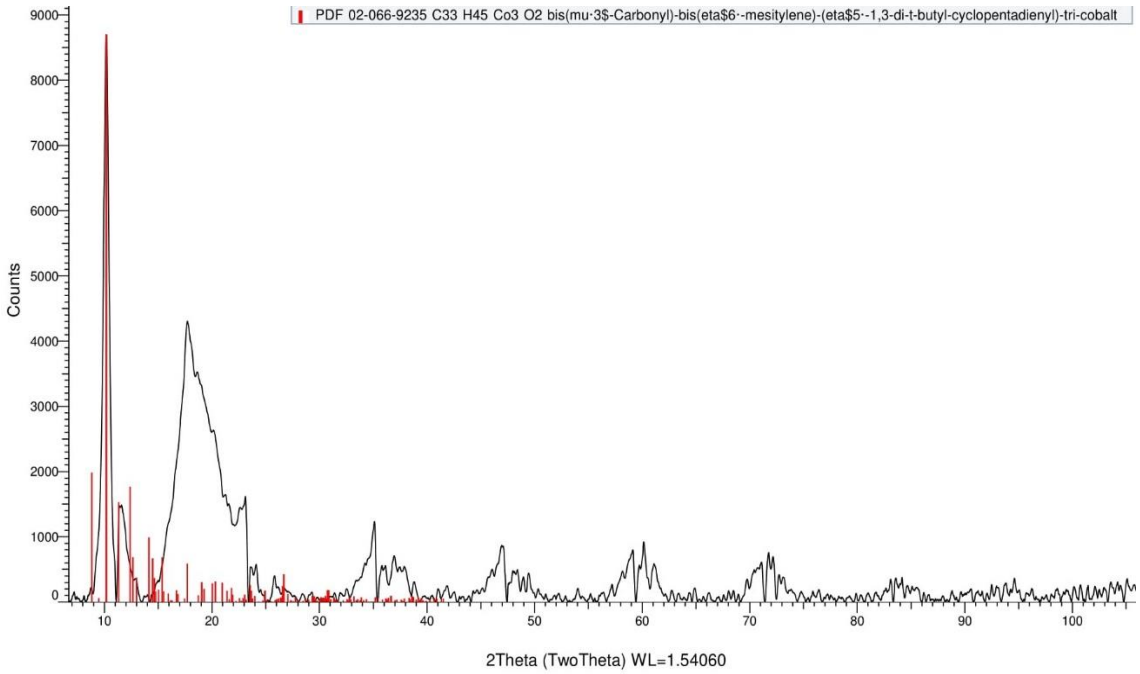

Fig. 68: PXRD pattern of [F] **[Co (H$_3$BTCA)$_4$ (Imidazole)]$_n$** (after activation)

Appendix C
Thermogravimetric analysis (TGA)

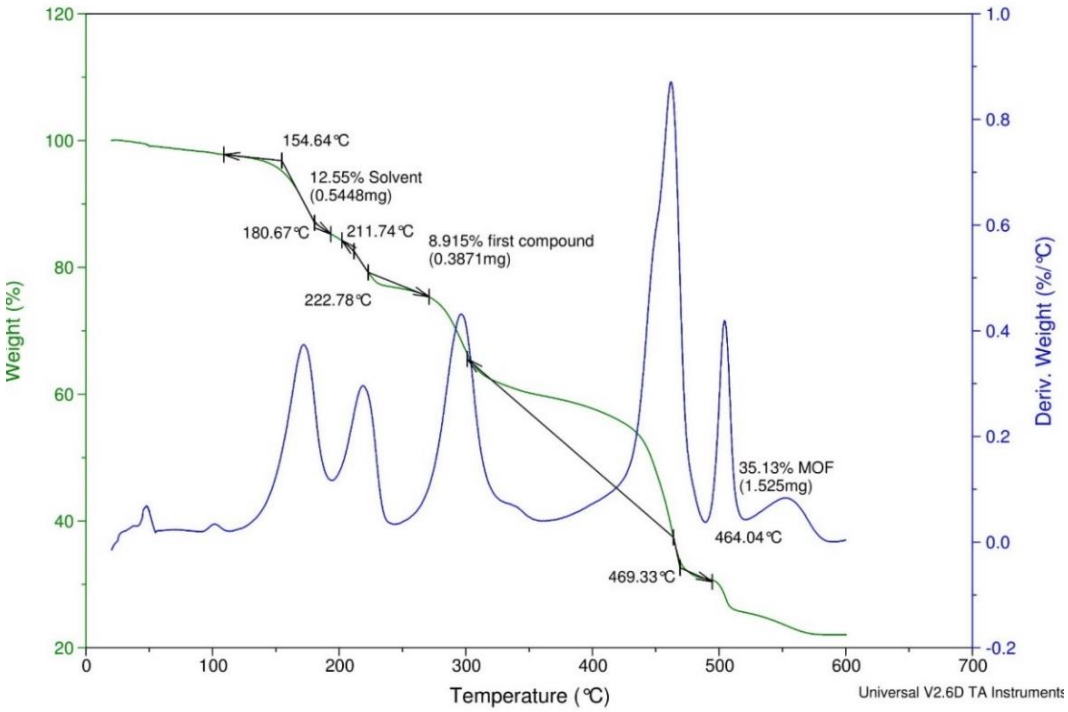

Fig. 69: Thermogravimetric analysis of compound [A]

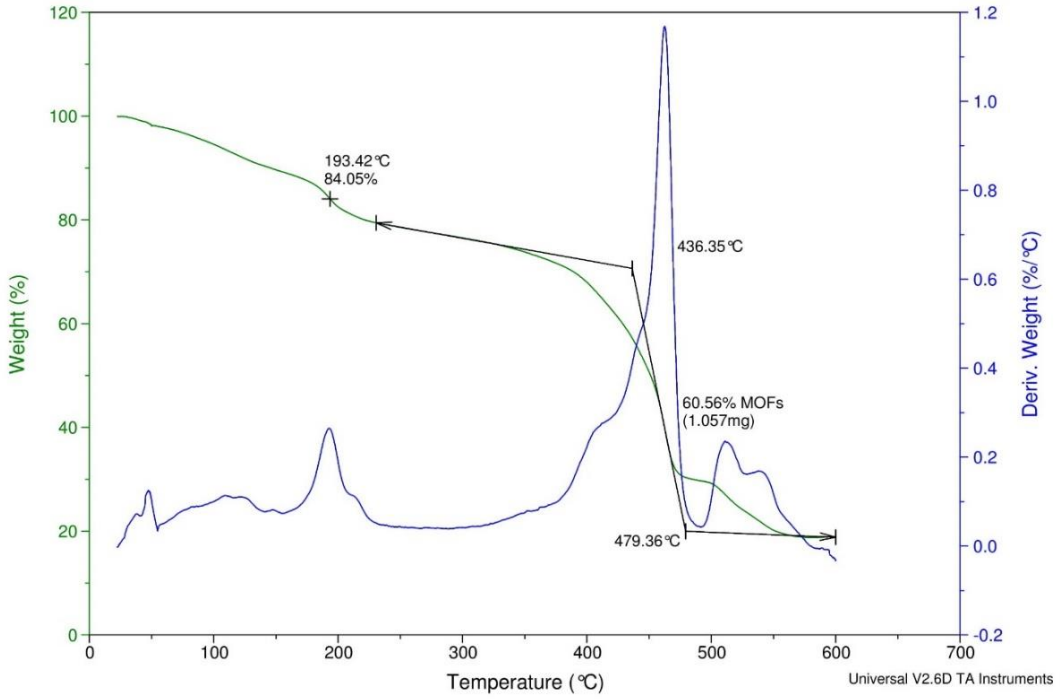

Fig. 70: Thermogravimetric analysis of [C] **$[Co_6(H_3BTCA)_8(DMF)_{18}(CO_2)_3]_n . 2H_2O$]**

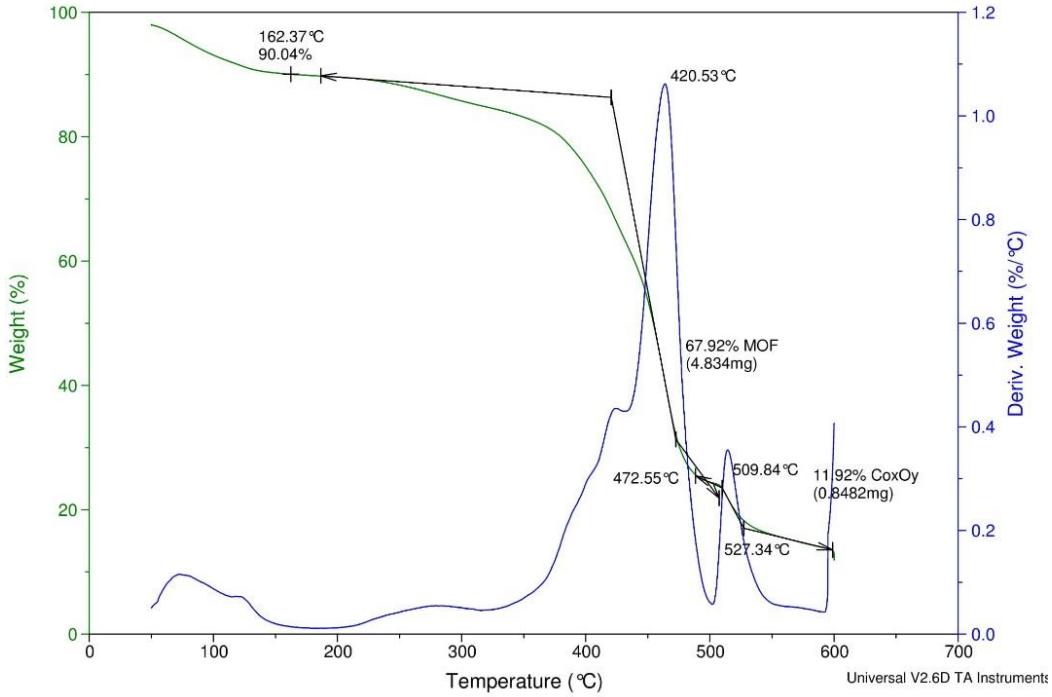

Fig. 71: TGA data of **[E] $[Co_3 (H_3BTCA) (DMF)_6(CO_2)_3]_n$**

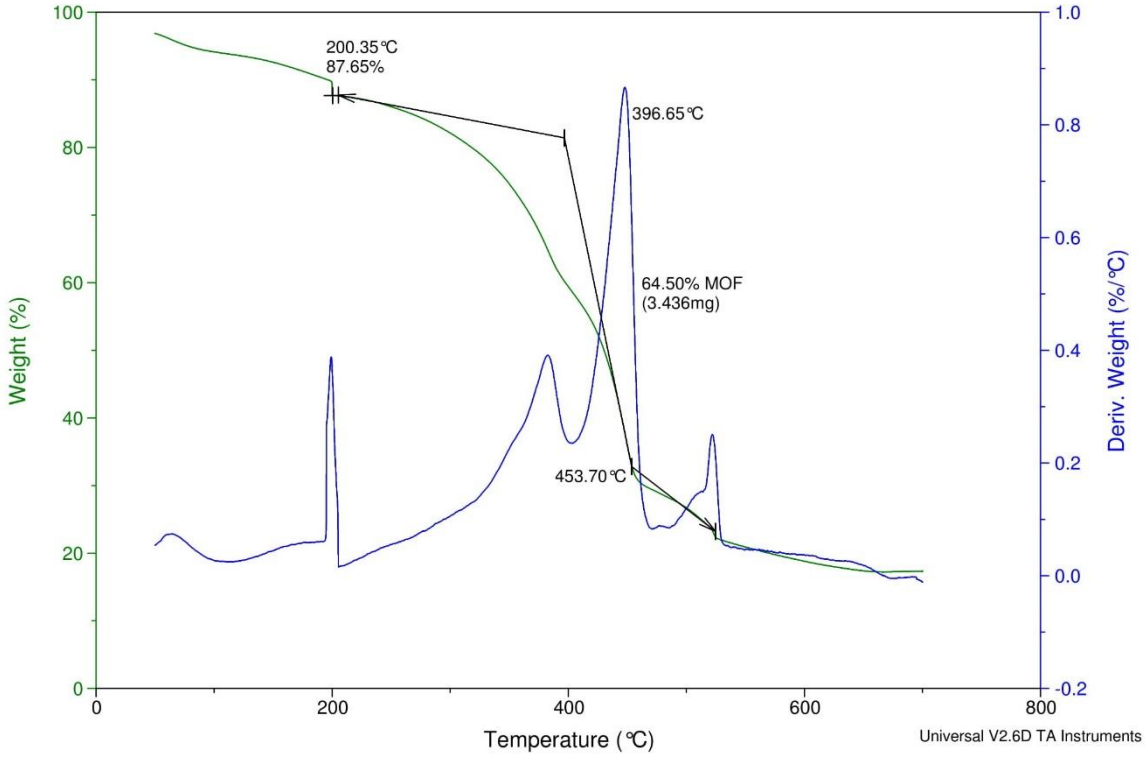

Fig. 72: TGA data of **[F] $[Co (H_3BTCA)_4 (Imidazole)]_n$**

Appendix D

BET surface area, EDS analysis, and TEM analysis

BET Single Point Tabular Report

Experiment 1: Experiment 1 Pre-treatment and First BET

Analysis Type: Physisorption Surface Area
Calibration: (292_0022) BET calibration-September 13, 2011
Measured Flow Rate: 50.12 cm³ STP/min
Signal Offset: 7.07970
Signal Inverted: No

Peak Summary

Experiment Number	Active Concen-tration	Relative Pressure	Cumulative Quantity (µmol/g)	1 / [Q(Po/P-1)] (g/µmol)
1	0.0000	0.0000	-17.07871	0.0000000
1	0.0000	0.0000	-41.35468	0.0000000

BET Analysis Summary

Atmospheric Pressure: 731 mmHg
Saturated Pressure: 775.00 mmHg
Cross-Sectional Area: 0.162 nm²
Monolayer Volume: 29.653 cm³/g
BET Surface Area: 129.0835 m²/g

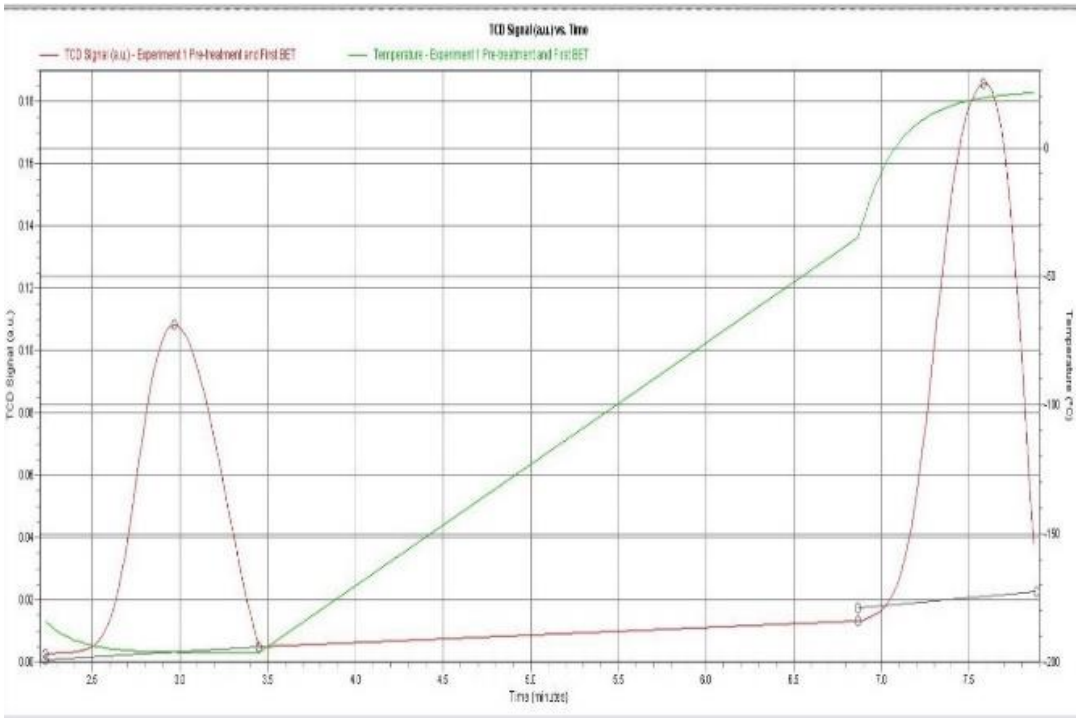

Fig. 73: a. BET Surface area analysis and b. TCD signal with a temperature of **[B]**

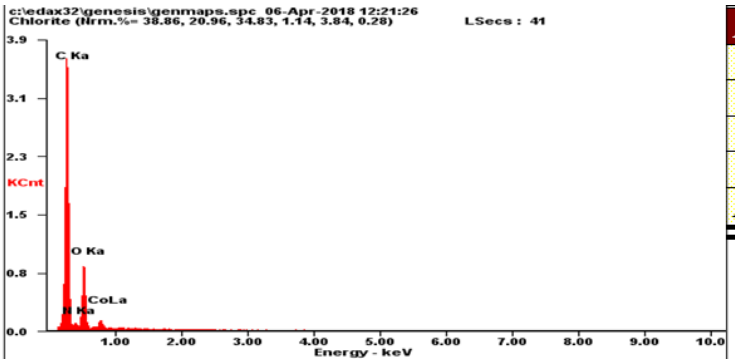

Element	Wt%	At%
CK	66.04	76.03
NK	05.05	04.98
OK	19.38	16.75
CoL	09.53	02.24
Matrix	Correction	ZAF

Fig. 74: EDS compositional analysis of [G]**[Co (H$_3$BTCA)$_3$ (DMF)]$_n$**

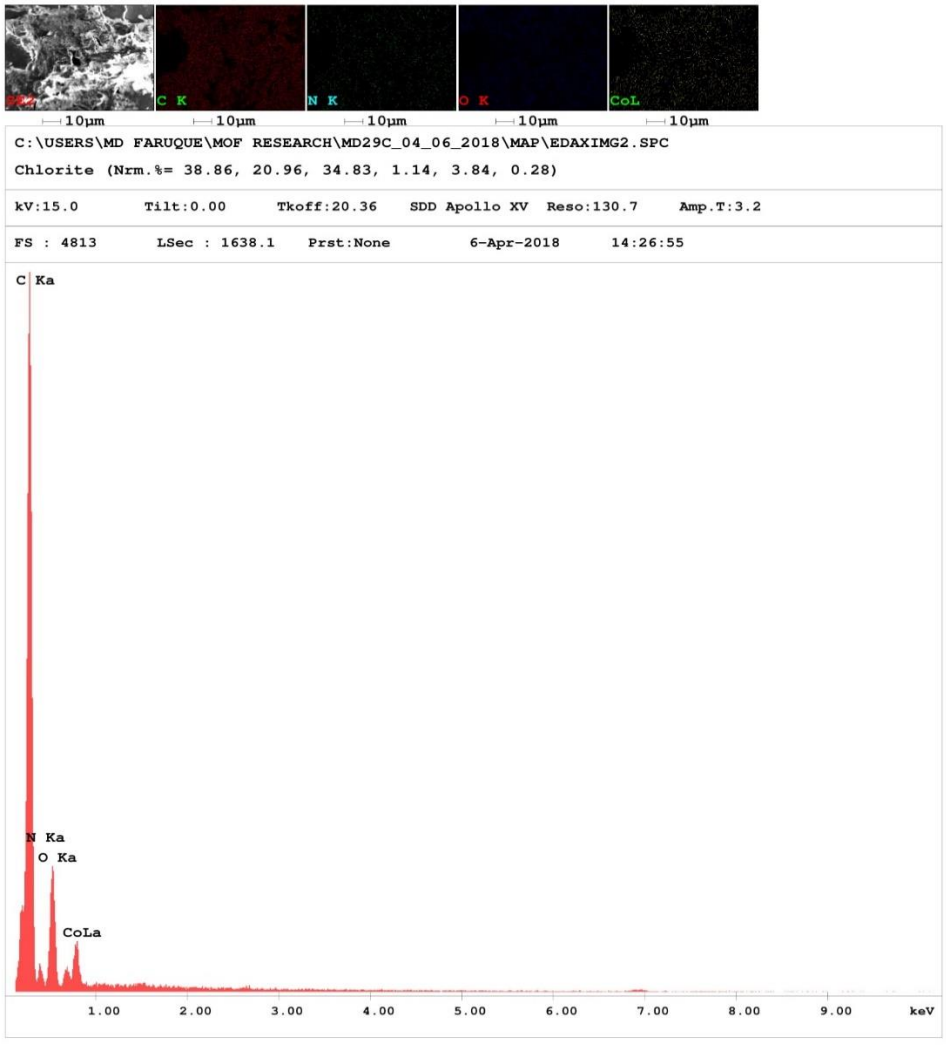

Fig. 75: Elemental mapping with EDS compositional analysis of **[H] [Co (H$_3$BTCA)$_3$ (DMF)$_2$]$_n$**

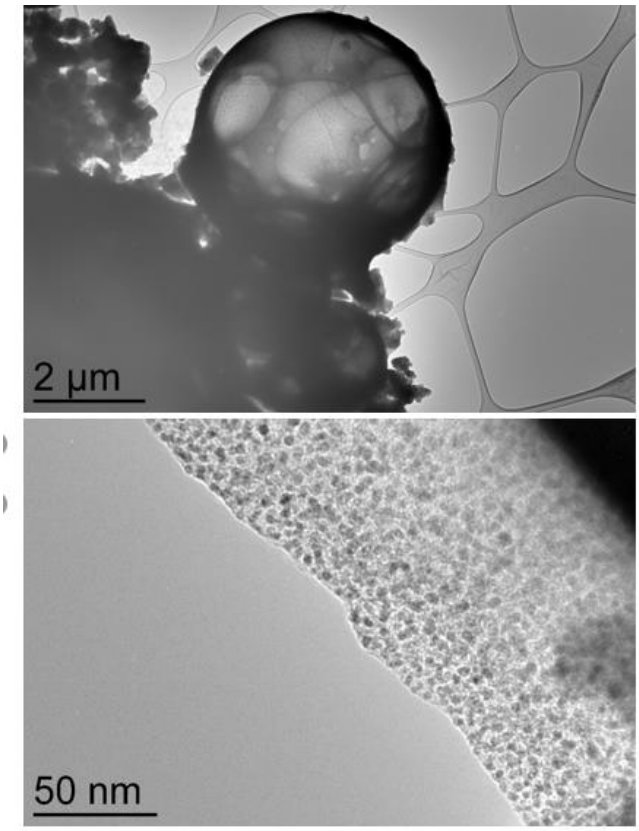

Fig. 76: TEM image of **[H] [Co (H$_3$BTCA)$_3$ (DMF)$_2$]$_n$** a. in microscale b. in nanoscale

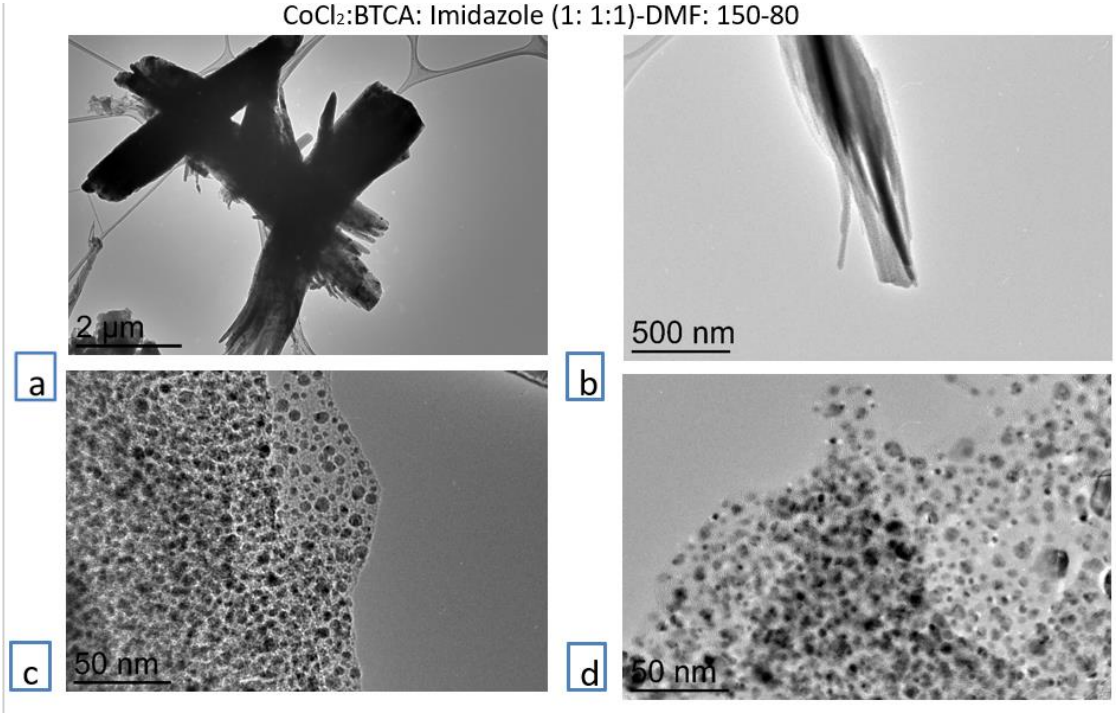

Fig. 77: TEM images of **[I] [Co (H$_3$BTCA)$_3$ (DMF)$_3$]$_n$** at different magnification

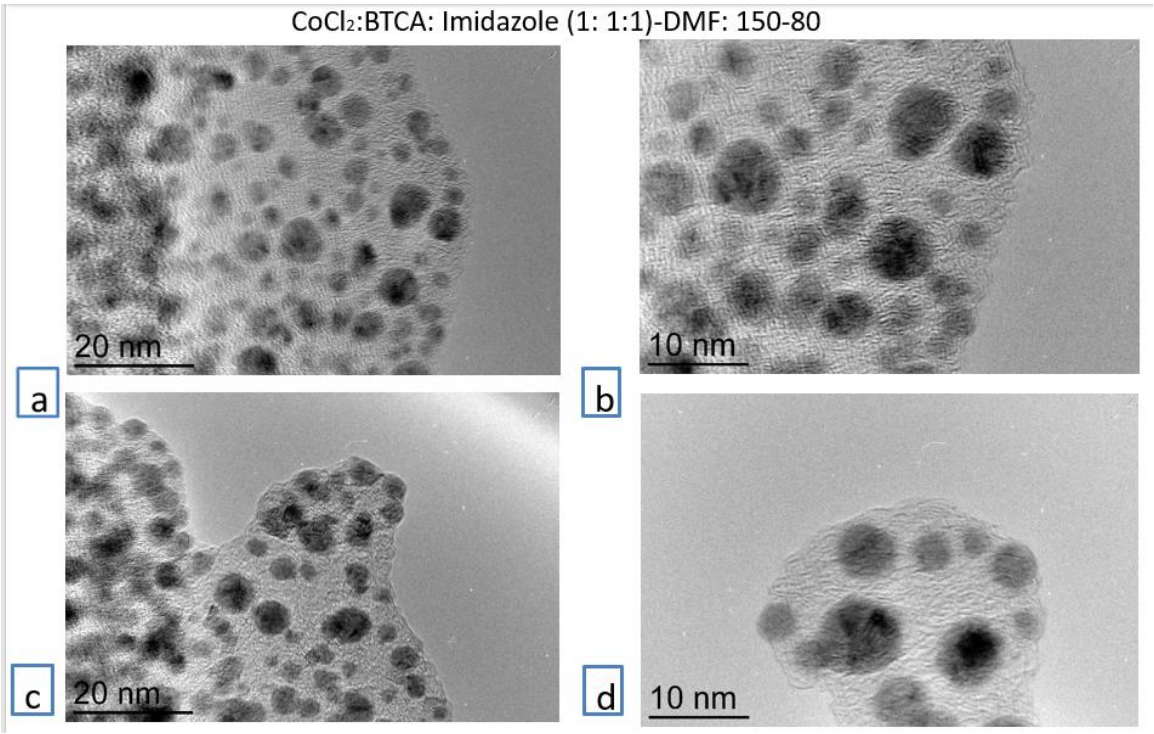

Fig. 78: HRTEM images of **[I] [Co (H$_3$BTCA)$_3$ (DMF)$_3$]$_n$**